2014

A needed response: Fragment molecular orbital analytic gradients

Kurt Ryan Brorsen
Iowa State University

Recommended Citation

Brorsen, Kurt Ryan, "A needed response: Fragment molecular orbital analytic gradients" (2014). *Graduate Theses and Dissertations*. 13920.
https://lib.dr.iastate.edu/etd/13920

A needed response: Fragment molecular orbital analytic gradients

by

Kurt Ryan Brorsen

A Dissertation submitted to the graduate faculty

in partial fulfillment of the requirements for the degree of

DOCTOR OF PHILOSOPHY

Major: Physical Chemistry

Program of Study Committee:
Mark S. Gordon, Major Professor
Theresa L. Windus
Monica H. Lamm
William S. Jenks
Jacob W. Petrich

Iowa State University

Ames, Iowa

2014

TABLE OF CONTENTS

Chapter 1. Introduction

1. Overview

Ab initio quantum chemistry seeks to describe and elucidate chemical species and processes using quantum mechanics. For dynamical chemical processes, molecular dynamics[1] (MD), where the atoms of a chemical system move according to Newton's laws of motion, is frequently used. MD calculations have historically used classical mechanics[2-4] rather than quantum mechanics to describe the evolution of a chemical system. The use of classical mechanics with MD has proven to be a great success, but classical MD has deficiencies, since quantum mechanics must be used to describe important chemical phenomena such as bond breaking or excited states accurately. With the increase of computer power over the past half-century, *ab initio* MD (AIMD) methods[5-7] that describe a chemical system using quantum mechanics have been developed to eliminate the deficiencies of classical MD.

Unfortunately, the application of AIMD is limited to small systems and short time scales since standard quantum chemical methods exhibit non-linear scaling with system size. More recently, new approaches[8,9] have circumvented the non-linear scaling of quantum chemical methods by exploiting the fact that most chemical interactions are local and therefore distant interactions can be approximated or even ignored. Other methods obtain quantum mechanical accuracy at a cost associated with classical mechanics by deriving a classical force field directly from *ab initio* calculations.[10-14] Individually and in combination, methods that eliminate the non-linear scaling of standard *ab initio* methods have the potential to extend the reach of AIMD to larger systems such as surfaces, molecular clusters, bulk liquids, and proteins.

2. Dissertation Overview

Chapter 1 of the thesis introduces the fundamental concepts of *ab initio* quantum chemistry and provides relevant background to the methods used in the subsequent chapters. Chapter 2 derives and discusses the implementation of the analytic gradient for the fragment molecular orbital (FMO) method interfaced with restricted Hartree-Fock theory. Chapter 3 derives and discusses the implementation of the analytic gradient for the FMO method interfaced with density functional theory. Chapter 4 demonstrates the need for the FMO analytic gradient for accurate FMO molecular dynamics (MD) simulations. Chapter 5 determines the surface affinity of the hydronium ion in water clusters using MD and umbrella sampling. Chapter 6 calculates the melting point of Ice-I_h water from MD simulations using the effective fragment potential. Chapter 7 concludes the thesis with a summary of the previous chapters.

3. Theoretical Background

The state at time *t* of a non-relativistic quantum system is determined by the time-dependent Schrodinger equation,[15] (atomic units are used throughout the introduction unless otherwise indicated).

$$i\frac{\partial}{\partial t}\Psi(\mathbf{r},t) = \hat{H}\Psi(\mathbf{r},t). \tag{1}$$

where $\Psi(\mathbf{r},t)$ is the wavefunction and $\mathbf{r}$ is the coordinates of all electrons and nuclei.

The Hamiltonian, $\hat{H}$, is defined as

$$\hat{H} = \sum_{i}^{N} \frac{-\nabla_i^2}{2m_i} + V(\mathbf{r},t), \tag{2}$$

where m_i is the mass of particle *i*, $V(\mathbf{r},t)$ is the potential, and the sum *N* is over all particles. For potentials that do not vary with time, $V(\mathbf{r},t) = V(\mathbf{r})$, the wavefunction can be written as a product, $\Psi(\mathbf{r},t) = \Psi(\mathbf{r})\Psi(t)$, and a time-independent Schrodinger equation can be derived,

$$\hat{H}\Psi(\mathbf{r}) = E\Psi(\mathbf{r}), \tag{3}$$

where *E* is the energy of the system.

For a system consisting of only nuclei and electrons, the Hamiltonian in Eq. (3) is

$$\hat{H} = \sum_{i}^{e} \frac{-\nabla_i^2}{2} + \sum_{A}^{n} \frac{-\nabla_A^2}{2m_A} - \sum_{A}^{n}\sum_{i}^{e} \frac{Z_A}{|R_A - r_i|} + \sum_{i>j}^{e} \frac{1}{|r_i - r_j|} + \sum_{A>B}^{n} \frac{Z_A Z_B}{|R_A - R_B|}, \tag{4}$$

where the sum *e* is over all electrons, the sum *n* is over all nuclei, Z_A is the nuclear charge of nucleus *A*, r_i is the electron coordinate of electron *i*, and R_A is the nuclear coordinate of nucleus *A*.

Eq. (3) is impossible to solve for chemical systems as Eq. (3) treats all nuclei and electrons quantum mechanically, and the electron-nuclei many-body problem cannot be separated. Since electrons are much lighter than the nuclei, the electrons move much faster than the nuclei. Therefore, the electrons are assumed to adjust immediately to any perturbation in the coordinates of the nuclei and the distribution of the electrons can be calculated assuming the nuclei are fixed points in space. The assumption is known as the Born-Oppenheimer approximation[16] and allows an electronic Schrodinger equation

$$\hat{H}_{elec}\Psi(\mathbf{r})_{elec} = E_{elec}\Psi(\mathbf{r})_{elec} \tag{5}$$

to be solved to determine the electronic wavefunction. The electronic Hamiltonian is

$$\hat{H}_{elec} = \sum_{i}^{e} \frac{-\nabla_i^2}{2} - \sum_{A}^{n}\sum_{i}^{e} \frac{Z_A}{|R_A - r_i|} + \sum_{i>j}^{e} \frac{1}{|r_i - r_j|}, \tag{6}$$

which is similar to the full Hamiltonian in Eq. (4) except that the 2nd and 5th terms in Eq. (4) have been eliminated.

For *ab initio* molecular dynamics calculations, the determination of the total energy of the system is necessary. Since the nuclei are taken to be point particles, the nuclei kinetic energy and nuclei-nuclei potential energy can be treated classically and the total energy can be written as

$$E_{total} = E_{elec} + \sum_{A>B}^{n} \frac{Z_A Z_B}{|R_A - R_B|} + \sum_{A}^{n} \frac{m_A \mathbf{v}_A^2}{2} \tag{7}$$

where $\mathbf{v}_A$ is the velocity of nuclei A.

For all but a few special cases, the electronic Schrodinger equation cannot be solved analytically due to the electron-electron interaction term. Therefore, the Hartree-Fock approximation[17] is applied and the third term in Eq. (4), the electron-electron interaction term, is replaced by a potential, $v^{HF}(i)$, that is the averaged position of the other electrons in the system. $v^{HF}(i)$ is defined as

$$v^{HF}(1) = \sum_{i=1}^{e} \left[\hat{J}_i(1) - \hat{K}_i(1) \right]. \tag{8}$$

In Eq. (8), $\hat{J}$, is the Coulomb operator, $\hat{K}$ is the exchange operator.

The Hartree-Fock potential is then used to define a Fock operator,

$$\hat{F} = \sum_{i}^{e} \frac{-\nabla_i^2}{2} - \sum_{A}^{n}\sum_{i}^{e} \frac{Z_A}{|R_A - r_i|} + \sum_{i}^{e} v^{HF}(i), \tag{9}$$

The Fock operator can be rewritten as a sum of one-electron operators

$$\hat{F}=\sum_i^e \hat{F}(i)=\sum_i^e\left[\frac{-\nabla_i^2}{2}+\sum_A^n\frac{Z_A}{|R_A-r_i|}+v^{HF}(i)\right], \tag{10}$$

and the Hartree-Fock equations can be written as a sequence of coupled one-electron eigenvalue problems,

$$\hat{F}(i)\psi(i)=\varepsilon_i\psi(i), \tag{11}$$

where $\psi(i)$, called a molecular orbital, is the eigenfunction of the one-electron Fock operator, $\hat{F}(i)$, and ε_i is the eigenvalue, called the orbital energy. Since each of the Hartree-Fock eigenvalue equations explicitly depend only on a single electron coordinate *i*, the total solution of the Hartree-Fock equations is a product of one-electron orbitals, $\psi(i)$, called a Hartree product

$$\Psi^{HP}=\psi(1)\psi(2)\psi(3)...\psi(N). \tag{12}$$

The Hartree product wavefunction is symmetric to the interchange of any two electrons and therefore violates the Pauli principle that requires the wavefunction to be anti-symmetric to the exchange of any two fermions. The violation of the Pauli principle can be fixed through the use of a Slater determinant,[18]

$$\Psi^{HF}=|\psi(1)\psi(2)\psi(3)...\psi(N)|, \tag{13}$$

which antisymmetrizes the Hartree product wavefunction. The wavefunction, Ψ^{HF}, is then used as the Hartree-Fock wavefunction.

As of yet, no restriction has been place on the form of the $\psi(i)$. To facilitate calculations, the one-electron orbitals are normally expanded in a linear combination of atomic orbitals (LCAO) as

$$\psi(i)=\sum_a C_{ai}\phi_a \tag{14}$$

where $C_{\alpha i}$ is the molecular orbital coefficient and ϕ_a is an atomic orbital. The atomic orbitals are also referred to as basis functions and for most *ab initio* calculations are Gaussian functions or contractions of multiple Gaussian functions.

With the introduction of the basis, the Roothan-Hall equations,[19]

$$\mathbf{FC} = \mathbf{SC}\varepsilon \tag{15}$$

can be derived. The Roothan-Hall equations change the integro-differential equations of Hartree-Fock into an algebraic form that can be solved using standard matrix techniques. In the Roothan-Hall equations, **F** is the Fock matrix

$$F_{\mu\nu} = \int d\mathbf{r}_1 \phi_\mu(1)\hat{F}(1)\phi_\nu(1), \tag{16}$$

C is the matrix of the molecular orbital coefficients $C_{\alpha i}$,

S is the overlap matrix,

$$S_{\mu\nu} = \int d\mathbf{r}_1 \phi_\mu(1)\phi_\nu(1), \tag{17}$$

and ε is a diagonal matrix of the orbital energies ε_i.

From the solution of the Roothan-Hall equations, the Hartree-Fock energy, E_{HF}, can be obtained. The Hartree-Fock method is variational, so E_{HF} is guaranteed to be an upper bound to the exact energy. The difference in energy between the exact energy and the Hartree-Fock energy is called the correlation energy, E_{corr}, and is defined as

$$E_{exact} = E_{HF} + E_{corr}. \tag{18}$$

Since the Hartree-Fock energy is an upper bound on the exact energy, the correlation energy is negative. The correlation energy arises from the replacement of the electron-electron interaction term in Eq. (6) with the Hartree-Fock potential in Eq. (9). While the correlation energy is small relative to the total energy, the correlation energy is still necessary to include to obtain accurate energies of chemical systems.

A common of way of including the correlation energy is through Møller-Plesset perturbation theory,[20] which uses Raleigh-Schrodinger perturbation theory with the Hartree-Fock wavefunction as a zeroth order wavefunction. The full Hamiltonian, $\hat{H}$, can be written as a sum of the Hartree-Fock Hamiltonian, $\hat{H}_0$, and a small perturbation, $\hat{V}$,

$$\hat{H} = \hat{H}_0 + \lambda\hat{V}. \tag{19}$$

The energy and the wavefunction can then be expanded in a series as

$$\Psi_{MPn} = \Psi_0 + \sum_{i=1}^{n} \lambda^i \Psi_i$$

$$E_{MPn} = E_0 + \sum_{i=1}^{n} \lambda_i E_i \tag{20}$$

After some algebra the Hartree-Fock wavefunction can be proven to be correct through first order and the second order energy term,

$$E_2 = \sum_{D} \frac{\left|\left\langle \Psi_D \middle| V \middle| \Psi_{HF} \right\rangle\right|^2}{E_D^{(0)} - E_{HF}^{(0)}}, \tag{21}$$

is the next energy term that contributes. In Eq. (21), the summation runs over all double excitations, D. Ψ_D are doubly excited determinants using the Hartree-Fock wavefunction as the ground state, and $E_D^{(0)}$ and $E_{HF}^{(0)}$ are the zeroth order energies of a doubly excited determinant and the Hartree-Fock wavefunction respectively. The second order energy term can be added to the Hartree-Fock energy

$$E_{MP2} = E_{HF} + E_2 \tag{22}$$

to obtain the second order Møller-Plesset (MP2) energy.

The second order energy term that is included in MP2 accounts for 80-90% of the total correlation energy. Higher order energy terms (MP3, MP4, etc…) can be added, but due to convergence issues with the higher order energy terms they are not routinely included.

As an alternative to the *ab initio* methods that use a wavefunction to calculate energies and properties, density functional theory[21] (DFT) uses the electronic density. DFT is in principal exact, and since the electronic density is a much simpler function than the electronic wavefunction, DFT is able to include electron correlation at less of a computational cost than wavefunction methods.

To practically perform DFT calculations, a set of equations similar to the Hartree-Fock equations, the Kohn-Sham equations, are solved. Instead of the Fock operator in Hartree-Fock theory, DFT uses the one-electron Kohn-Sham operator $\widehat{h}_{KS}$,

$$\widehat{h}_{KS} = \frac{-\nabla^2}{2} + \sum_{A}^{n} \frac{Z_A}{|R_A - r|} + \int dr' \frac{\rho(r')}{r - r'} + V^{XC}(r) \tag{23}$$

The Kohn-Sham operator is similar to the Fock operator in that the electrons can be treated as independent particles. The difference between DFT and HF lies in the replacement of the HF exchange term with the exchange correlation term, $V^{XC}(r)$. The replacement of the HF exchange term with $V^{XC}(r)$ allows DFT to include electron correlation in the calculation and if the exact $V^{XC}(r)$ was known, DFT would be exact. Unfortunately, the exact $V^{XC}(r)$ has never been found for any chemical system, and approximation of $V^{XC}(r)$ is necessary. Though DFT is not systematically improvable, unlike perturbative methods, such as Moller-Plesset perturbation theory or other *ab initio* methods like coupled cluster theory are in principal, the cheap cost of solving the Kohn-Sham equations combined with the inclusion of some electron correlation has resulted in DFT being widely used in electronic structure calculations.

Standard implementations of quantum mechanical methods scale poorly with respect to system size. Hartree-Fock scales ~N^4, MP2 scales ~N^5, and the coupled cluster singles and doubles with perturbative triples method scales ~N^7, where N is the number of basis functions. In order to circumvent the non-linear scaling, fragmentation can be employed. In fragmentation methods, instead of one large quantum mechanical calculation on the system of interest, the system is divided into smaller pieces, termed fragments, and then a quantum mechanical calculation is performed on each of the fragments. Many fragmentation methods exist,[9] but the present thesis will focus on the fragment molecular orbital (FMO) method.[23] The FMO methods begins by dividing a chemical system into non-overlapping fragments termed monomers. A quantum mechanical calculation is then performed on each of the monomers in the electrostatic potential of all the other monomers. The field is then updated with the new density of each monomer and the process is iterated to self-consistency. Next, a quantum mechanical calculation may be performed on pairs of monomers or dimers, as in the FMO2 method. The dimer calculation also takes place in the electrostatic potential of all other monomers, but is not iterated, because the dimer calculation is considered to be a small perturbation to the monomer energies. If 3-(4-,5-,…)body properties are important for the system, calculations can also be performed on trios (quartets, quintets, …) of monomers in the electrostatic potential of all other monomers. Similar to the dimer calculation, the additional n-body calculations are not iterated to self-consistency.

The FMO energy is then calculated as a sum of an n-body expansion of the energy of the n-mers. The expansion can be written as sum of n-order energies

$$\begin{aligned} E_{FMO(N)} &= E^1 + E^2 + E^3 + \ldots + E^N \\ E^1 &= \sum_{I}^{N} E_I \\ E^2 &= \sum_{I>J}^{N} \left(E_{IJ} - E_I - E_J \right) \qquad . \\ E^3 &= \sum_{I>J>K}^{N} \left(E_{IJK} - E_I - E_{J-} E_K - \Delta E_{IJ} - \Delta E_{JK} - \Delta E_{IK} \right) \end{aligned} \tag{24}$$

where

$$\Delta E_{IJ} = E_{IJ} - E_I - E_J , \tag{25}$$

The sum N is over all fragments and E_X , E_{XY} , and E_{XYZ} are the energies of monomer X, dimer XY, and trimer XYZ respectively.

The termination of the n-body expansion at second order is called FMO2 and is the most commonly used FMO expansion. Termination of the expansion at third order is called FMO3 and will also be used in the following chapters.

Modeling solvation effects, especially the solvation by water, is important for a wide variety of systems. Modeling solvation through the addition of quantum mechanical solvent molecules rapidly becomes infeasible due to the previously described poor scaling with system size of quantum mechanical methods. While fragmentation methods such as FMO can help reduce the scaling, the inclusion of solvent effects using FMO still proves computationally difficult. Partly due to the difficulty of describing solvent effects using *ab initio* methods, quantum mechanical/molecular mechanical (QM/MM) methods[24-26] have been developed that allow a solute molecule to be described using quantum mechanics while the surrounding solvent molecules are treated with classical mechanics. One such method is the effective fragment potential (EFP).[10-13] EFP is a one-electron model potential with parameters derived from an *ab initio* calculation. EFP has two models, EFP1, which is restricted to water, and EFP2, which can be used to model any solvent. As EFP particles are internally frozen, they can only model intermolecular interactions. EFP differs from most classical solvation potentials in that EFP contains no empirically fitted parameters.

To simulate the dynamics of a chemical system, molecular dynamics[1] (MD), in which atoms move according to Newton's second law of motion,

$$F = ma, \tag{26}$$

is commonly used. To find the acceleration on an atom and subsequently the velocity and position of the atom, the calculation of the force is necessary. In a quantum mechanical calculation, the force on an atom can be obtained by calculating the gradient of the potential, which is found from the derivative of the total energy with respect to nuclear coordinate. Therefore, the calculation of accurate gradients is of great importance for *ab initio* MD simulations.

References

1. Frenkel, D.; Smit, B. *Understanding molecular simulation: from algorithms to applications*. Academic Press, Inc. Orlando, FL,1996

2. Ponder, J. W.; Wu, C.; Ren, P.; Pande, V. S.; Chodera, J. D.; Schnieders, M. J.; Haque, I. *The Journal of Physical Chemistry B* 114, no. 8 (2010): 2549-2564.

3. Vanommeslaeghe, K.; Hatcher, E.; Acharya, C.; Kundu, S.; Zhong, S.; Shim, J.; Darian, E; *Journal of computational chemistry* 31, no. 4 (2010): 671-690.

4. Cornell, W. D.; Cieplak, P.; Bayly, C. I.; Gould, I. R.; Merz, K. M.; Ferguson, D. M.; Spellmeyer, D. C.; Fox, T.; Caldwell, J. W.; Kollman. P. A. *Journal of the American Chemical Society* 117, no. 19 (1995): 5179-5197.

5. Car, R.; Parrinello, M. *Physical review letters* 55, no. 22 (1985): 2471.

6. Kresse, G.; Hafner, J. *Physical Review B* 49, no. 20 (1994): 14251.

7. Kresse, G.; Hafner, J. *Physical Review B* 47, no. 1 (1993): 558.

8. Zalesny, R.; Papadopoulos, M. G.; Mezey, P. G.; Leszczynski, J. *Linear-Scaling Techniques in Computational Chemistry and Physics*, Springer, Berlin, 2011.

9. Gordon M. S.; Fedorov, D. G.; Pruitt, S. R.; Slipchenko, L. V. Chem. Rev. 112 (2012) 632.

10. Jensen, J. H.; Day, P. N.; Gordon, M. S.; Basch, H.; Cohen, D.; Garmer, D. R.; Kraus, M.; Stevens, W. J. *Modeling the Hydrogen Bond*, 1994, 569, 139–151.

11. Day, P. N.; Jensen, J. H.; Gordon, M. S.; Webb, S. P.; Stevens, W. J.; Krauss, M.; Garmer, D.; Basch, H.; Cohen, D. *J. Chem. Phys.* 1996, 105, 1968-1986.

12. Gordon, M. S.; Freitag, M. A.; Bandyopadhyay, P.; Jensen, J. H.; Kairys, V.; Stevens, W. J. *J. Phys. Chem*. A 2001, 105, 293-307.

13. Gordon, M. S.; Slipchenko, L. V.; Li, H.; Jensen, J.H.. *Annual Reports in Computational Chemistry*, 2007, 3, 177-193.

14. Gordon, M. S.; Mullin, J. M.; Pruitt, S. R.; Roskop, L. B.; Slipchenko, L. V.; Boatz, J. A. *J. Phys. Chem. B 2009*, 113, 9646-9663.

15. (a) Schrödinger, E. Ann. Phys. 1926, 79, 361. (b) Schrödinger, E. Ann. Phys., 1926, 79, 489. (c) Schrödinger, E. Ann. Phys., 1926, 79, 734. (d) Schrödinger, E. Ann. Phys., 1926, 80, 437. (e) Schrödinger, E. Ann. Phys., 1926, 81, 109. (f) Schrödinger, E. Die Naturwissenschaften, 1926, 14, 664.

16. Born, M; Oppenheimer, R. Ann. Phys., 1927, 84, 457.

17. (a) Hartree, D. R. Proc. Cambridge Philos. Soc., 1928, 24, 89. (b) Hartree, D. R. Proc. Cambridge Philos. Soc., 1928, 24, 111. (c) Hartree, D. R. Proc. Cambridge Philos. Soc., 1928, 24, 426. (d) Fock, V. Z. Phys.,

1930, 61, 126. (e) Fock, V. Z. Phys., 1930, 62, 795.

18. Slater, J. C. Phys. Rev., 1929, 34, 1293.

19. Roothaan, C. C. J. *Reviews of modern physics* 23, no. 2 (1951): 69.

20. Møller, C.; Plesset, M. S. Phys. Rev. 1934, 46, 618.

21. Kohn W.; Sham L. J. Phys. Rev. 1965, 140, A1133.

22. Shavitt, Isaiah; Bartlett, Rodney J. *Many-Body Methods in Chemistry and Physics: MBPT and Coupled-Cluster Theory*. Cambridge University Press 2009

23. Kitaura, K.; Ikeo, E.; Asada, T.; Nakano, T.; Uebayasi, M. Chem. Phys. Lett. 1999, 313, 701.

24. Warshel, A.; Levitt, M.; *Journal of molecular biology* 103, no. 2 (1976): 227-249.

25. Lin, H.; Truhlar, D. G. *Theoretical Chemistry Accounts* 117, no. 2 (2007): 185-199.

26. Senn, H. M.; Thiel, W. *Angewandte Chemie International Edition* 48, no. 7 (2009): 1198-1229.

Chapter 2. Fully analytic energy gradient in the fragment molecular orbital method

A paper published in *The Journal of Chemical Physics*

Takeshi Nagata, Kurt Brorsen, Dmitri G. Fedorov, Kazuo Kitaura, Mark S. Gordon

Abstract

The Z-vector equations are derived and implemented for solving the response term due to the external electrostatic potentials, and the corresponding contribution is added to the energy gradients in the framework of the fragment molecular orbital (FMO) method. To practically solve the equations for large molecules like proteins, the equations are decoupled by taking advantage of the local nature of fragments in the FMO method and establishing the self-consistent Z-vector method. The resulting gradients are compared with numerical gradients for the test molecular systems: $(H_2O)_{64}$, alanine decamer, hydrated chignolin with the protein data bank (PDB) ID of 1UAO and a Trp-cage miniprotein construct (PDB ID: 1L2Y). The computation time for calculating the response contribution is comparable to or less than that of the FMO self-consistent charge calculation. It is also shown that the energy gradients for the electrostatic dimer approximation are fully analytic, which significantly reduces the computational costs. The fully analytic FMO gradient is parallelized with an efficiency of about 98 % on 32 nodes.

1. Introduction

Dynamics simulations of large molecules have become very important in the field of computational chemistry.[1-7] For example, thermodynamic data such as the free energy and entropy can be extracted from such simulations. Since chemical processes occur at non-zero temperatures, an increasing number of molecular dynamics (MD) simulations have been performed using model potentials based on molecular mechanics (MM). Another common use of computational simulations is the sampling of potential energy surfaces for local and global minima using for example, Monte Carlo (MC) simulations. For instance, the structural data of proteins measured by X-ray or nuclear magnetic resonance (NMR) can be refined with the help of a computational simulation and the resulting structure stored in the protein data bank (PDB). Classical MM schemes can, in principle, be replaced by more accurate methods that consider the electronic structure explicitly.[8-13] The benefit of this replacement is that by using first principles methods, more reliable and sophisticated thermodynamic properties, dynamics, and structures can be provided.

The cost of conventional quantum mechanical (QM) electronic structure approaches formally scales at least as N^m, where N measures the size of the molecular system and m ranges from 3 for simple methods (e.g., the local density approximation of density functional theory) to much higher values for correlated methods. Considerable efforts are invested in developing linear scaling or $O(N)$ methods.[14, 15] The fragmentation methods have a fairly long history[16-22] and now it is an active area of research.[13,23-32]

One such method is the fragment molecular orbital (FMO) method.[33-36] The FMO method enables the calculation of electronic states for large molecules by performing MO calculations in parallel on fragments of a large molecular system using external electrostatic potentials (ESP). These ESPs describe the electrostatic field due to charge distributions of all of the other fragments. MOs of individual fragments are local in nature, because they are expanded in terms of basis functions on the atoms in the fragments, reducing the computation time significantly. Additionally, in order to realize linear-scaling, approximations have been proposed for the time-consuming ESP calculation in FMO[34, 37] and other methods.[10] The fragment self-consistent procedure employed in FMO has been used in somewhat different forms in other methods,[18, 19,38,,9,39] while the many-body expansion of the energy is conceptually related to the theory of intermolecular interactions[16] or the density expansion method.[20]

Over the past decade, the FMO method has become one of the most extensively developed fragmentation methods for the calculation of accurate chemical properties, such as the total energy, the dipole moment and the interaction energy between fragments in large systems. The FMO method has been interfaced with many QM methods: Second order Møller-Plesset (MP2) perturbation theory,[40, 41] coupled-cluster (CC) theory,[42] density functional theory (DFT),[43, 44] the multiconfiguration self-consistent field (MCSCF) method,[45] configuration interaction (CI),[46, 47] time-dependent DFT (TDDFT),[48, 49, 50] open-shells[51] and nuclear-electronic orbitals.[52] For these methods, the total energies are in good agreement with the corresponding conventional QM total energies. The FMO method has been applied to a number of large systems.[53-66] FMO-MD has been used[67-78] to study the dynamics of various processes such as chemical reactions. However, the FMO-MD method suffers from an accumulation of errors[67] with the time evolution due to an incomplete analytic FMO energy gradient.

The analytic FMO energy gradient reported by Kitaura et al. in 2001,[79] was incomplete since the response term due to the ESPs was neglected assuming that it is a small contribution for small basis sets. It was subsequently illustrated that when using larger basis sets, such as 6-31G(d),[80] the response contribution to the gradient is substantial. Evaluating the response contribution requires the solution of the coupled-perturbed Hartree-Fock (CPHF) equations. These equations are time-consuming to solve for large molecules, since they depend not on the fragment size, but on the size of the entire system.

Since the original report of a partially analytic FMO gradient,[79] several improvements regarding previously missing terms in the FMO gradient have been implemented in the GAMESS program package:[81, 82] (a) The ESP derivative terms including the Mulliken point charge (PTC) approximation (ESP-PTC);[80] (b) the derivative of the dimer energy of two distant fragments approximated as the electrostatic interaction energy (the electrostatic dimer approximation, ES-DIM)[83] and (c) the hybrid orbital projection derivatives.[84]

The last and most complicated missing response term is the subject of the present paper in which the exact response term for the FMO ESP gradient contribution is introduced, and the fully analytic FMO energy gradient is implemented, with an additional computation time requirement that is comparable to the first step of an FMO calculation (the self-consistent charge, SCC, iterations. The gradient implementation is also extended to the ES-DIM approximation, but not yet to the ESP-PTC approximation. Consequently, the usefulness of the FMO method is improved by establishing a complete expression of the analytic energy gradient.

Similarly to FMO, the response term arises in other methods where the external charges are not fully self-consistent. For example, in the electronically embedded method[85, 86] the layers are introduced in the system, this is different from fragments because layers are mutually inclusive, i.e., lower layers include higher layers, and thus the lowest layer calculation deals with the whole system, whereas the fragment based approach we take uses the locality of fragments. On the other hand in some other fragment methods such as X-Pol[87] the CPHF-related terms do not arise.

2. Fully analytic FMO energy gradient

2.1 Overview of the FMO energy gradient

In the following equations, the FMO energy expression[33-36] and the corresponding gradient equations are briefly summarized. The 2-body FMO (FMO2) total energy is represented as

$$E = \sum_{I}^{N} E_I^{'} + \sum_{I>J}^{N} (E_{IJ}^{'} - E_I^{'} - E_J^{'}) + \sum_{I>J}^{N} \mathrm{Tr}(\Delta \mathbf{D}^{IJ} \mathbf{V}^{IJ}), \tag{1}$$

where $E_X^{'}$ is the internal fragment energy for fragment X (X=I or IJ, for monomers and dimers, respectively). $\mathbf{V}^{IJ}$ is the matrix form of the electrostatic potential (ESP) for dimer IJ due to the electron densities and nuclei of the remaining fragments, i.e.,

$$V_{\mu\nu}^{IJ} = \sum_{K \neq IJ} \left(u_{\mu\nu}^{K} + v_{\mu\nu}^{K} \right). \tag{2}$$

The one-electron and two-electron integrals in $V_{\mu\nu}^{IJ}$ are, respectively,

$$u_{\mu\nu}^{K} = \sum_{A \in K} \langle \mu | \frac{-Z_A}{|\mathbf{r} - \mathbf{R}_A|} | \nu \rangle, \tag{3}$$

$$v_{\mu\nu}^{K} = \sum_{\lambda\sigma \in K} D_{\lambda\sigma}^{K} (\mu\nu | \lambda\sigma), \tag{4}$$

where $D_{\lambda\sigma}^{K}$ is the density matrix element of fragment K and $(\mu\nu\,|\,\lambda\sigma)$ is a two-electron integral in the AO basis. The dimer density matrix difference $\Delta\mathbf{D}^{IJ}$ in Eq. (1) is defined by

$$\Delta\mathbf{D}^{IJ} = \mathbf{D}^{IJ} - (\mathbf{D}^{I} \oplus \mathbf{D}^{J}). \tag{5}$$

We note that the SCC process ensures the self-consistency of monomer densities with respect to each other but not monomer and dimer densities. The direct sum in Eq. (5) means blockwise addition of two monomer matrices into the dimer supermatrix.

The internal fragment energies in Eq. (1) may be written in the form:

$$E_X^{'} = \sum_{\mu\nu\in X} D_{\mu\nu}^{X} h_{\mu\nu}^{X} + \frac{1}{2}\sum_{\mu\nu\lambda\sigma\in X}\left[D_{\mu\nu}^{X} D_{\lambda\sigma}^{X} - \frac{1}{2} D_{\mu\lambda}^{X} D_{\nu\sigma}^{X}\right](\mu\nu\,|\,\lambda\sigma) + \sum_{\mu\nu\in X} D_{\mu\nu}^{X} P_{\mu\nu}^{X} + E_X^{\mathrm{NR}}, \tag{6}$$

where $h_{\mu\nu}^{X}$ is the X-mer one-electron Hamiltonian and the nuclear repulsion energy is

$$E_X^{\mathrm{NR}} = \sum_{B\in X}\sum_{A(\in X)>B} \frac{Z_A Z_B}{R_{AB}}. \tag{7}$$

Note that monomer and dimer densities are determined by the MO calculations in the presence of ESPs due to the remaining monomers. For fragmentation across a covalent bond, the hybrid orbital projection (HOP) contribution

$$\sum_{i\in X}^{\mathrm{occ}} 2\langle i|\hat{P}^{X}|i\rangle = \sum_{\mu\nu\in X} D_{\mu\nu}^{X} P_{\mu\nu}^{X}, \tag{8}$$

must be considered in Eq. (6). The HOP operator is defined by

$$\hat{P}^{X} = \sum_{k\in X} B_k |\theta_k\rangle\langle\theta_k|, \tag{9}$$

where $|\theta_k\rangle$ is a hybrid orbital and the universal constant B_k is usually set to 10^{6}.

The differentiation of $E_X^{'}$ with respect to nuclear coordinate a leads to

$$\frac{\partial E'_X}{\partial a} = \sum_{\mu\nu\in X} D^X_{\mu\nu}\frac{\partial h^X_{\mu\nu}}{\partial a} + \frac{1}{2}\sum_{\mu\nu\lambda\sigma\in X}\left[D^X_{\mu\nu}D^X_{\lambda\sigma} - \frac{1}{2}D^X_{\mu\lambda}D^X_{\nu\sigma}\right]\frac{\partial(\mu\nu|\lambda\sigma)}{\partial a} + \sum_{\mu\nu\in X} D^X_{\mu\nu}\frac{\partial P^X_{\mu\nu}}{\partial a} \tag{10}$$

$$-2\sum_{i,j\in X}^{\text{occ}} S^{a,X}_{ji}F'^X_{ji} - 4\sum_{i\in X}^{\text{occ}}\sum_{r\in X}^{\text{vir}} U^{a,X}_{ri}V^X_{ri} + \frac{\partial E^{\text{NR}}_X}{\partial a},$$

where the overlap derivative matrix element is defined by

$$S^{a,X}_{ij} = \sum_{\mu\nu\in X} C^{X*}_{\mu i}\frac{\partial S^X_{\mu\nu}}{\partial a}C^X_{\nu j}. \tag{11}$$

The internal fragment Fock matrix element F'^X_{ij} is given in terms of MOs:

$$F'^X_{ij} = h^X_{ij} + \sum_{k\in X}^{\text{occ}}\left[2(ij|kk) - (ik|jk)\right] + P^X_{ij}, \tag{12}$$

where the MO-based projection operator matrix P^X_{ij} is introduced for convenience:

$$P^X_{ij} = \sum_{\mu\nu\in X} C^{X*}_{\mu i}P^X_{\mu\nu}C^X_{\nu j}. \tag{13}$$

Throughout this study, the Roman ($ijkl\cdots$) and Greek ($\mu\nu\rho\sigma\cdots$) indices denote the molecular orbitals and atomic orbitals (AO) respectively. For the response term in Eq. (10), the following equation defined in the previous study[80] is introduced:

$$\overline{U}^{a,X,Y} = 4\sum_{i\in X}^{\text{occ}}\sum_{r\in X}^{\text{vir}} U^{a,X}_{ri}V^Y_{ri}. \tag{14}$$

The response terms $U^{a,X}_{ri}$ associated with ESP V^Y_{ri} in the MO basis arise from the expansion of the MO coefficient derivative in terms of the MO coefficients,[88] and Eq. (14) sums the $U^{a,X}_{ri}$ terms multiplied by the V^Y_{ri} terms in order to simplify the gradient derivations. There are two types of $\overline{U}^{a,X,Y}$ terms: (a) $\overline{U}^{a,I,I}$ (i.e., X=Y) arising from the derivative of the monomer terms, and (b) $\overline{U}^{a,X,IJ}$ where *X* can be *I*, *J* or *IJ* (related to the three **D** terms in Eq. (5)). The derivatives of the MO coefficients can be written as

$$\frac{\partial C^{X}_{\mu i}}{\partial a} = \sum_{m\in X}^{\text{occ+vir}} U^{a,X}_{mi} C^{X}_{\mu m}. \tag{15}$$

To obtain the occupied-virtual orbital response $U^{a,X}_{ri}$, one must solve the CPHF equations. This will be discussed in subsequent subsections.

The differentiation of the ESP energy contribution in Eq. (1) with respect to nuclear coordinate *a* leads to

$$\begin{aligned}\frac{\partial}{\partial a}\mathrm{Tr}(\Delta\mathbf{D}^{IJ}\mathbf{V}^{IJ}) = {} & \sum_{\mu\nu\in IJ}\Delta D^{IJ}_{\mu\nu}\sum_{K\neq IJ}\left[\frac{\partial u^{K}_{\mu\nu}}{\partial a} + \sum_{\lambda\sigma\in K} D^{K}_{\lambda\sigma}\frac{\partial(\mu\nu\,|\,\lambda\sigma)}{\partial a}\right] \\ & -2\sum_{\mu\nu\in IJ} W^{IJ}_{\mu\nu}\frac{\partial S^{IJ}_{\mu\nu}}{\partial a} + 2\sum_{\mu\nu\in I} W^{I}_{\mu\nu}\frac{\partial S^{I}_{\mu\nu}}{\partial a} + 2\sum_{\mu\nu\in J} W^{J}_{\mu\nu}\frac{\partial S^{J}_{\mu\nu}}{\partial a} + \overline{U}^{a,IJ,IJ} - \overline{U}^{a,I,IJ} - \overline{U}^{a,J,IJ} \\ & -2\sum_{K\neq IJ}\sum_{\mu\nu\in K}\Delta X^{K(IJ)}_{\mu\nu} S^{a,K}_{\mu\nu} + 4\sum_{K\neq IJ}\sum_{\mu\nu\in IJ}\sum_{r\in K}^{\text{vir}}\sum_{i\in K}^{\text{occ}}\Delta D^{IJ}_{\mu\nu} U^{a,K}_{ri}(\mu\nu\,|\,ri),\end{aligned} \tag{16}$$

where

$$W^{X}_{\mu\nu} = \frac{1}{4}\sum_{\lambda\sigma\in X} D^{X}_{\mu\lambda} V^{IJ}_{\lambda\sigma} D^{X}_{\sigma\nu}, \tag{17}$$

and

$$\Delta X^{K(IJ)}_{\mu\nu} = \frac{1}{4}\sum_{\lambda\sigma\in K} D^{K}_{\mu\lambda}\left[\sum_{\zeta\eta\in IJ}\Delta D^{IJ}_{\zeta\eta}(\zeta\eta\,|\,\lambda\sigma)\right] D^{K}_{\sigma\nu}. \tag{18}$$

The collection of all the $\overline{U}^{a,X,Y}$ terms in Eq. (10) and Eq. (16) subject to the differentiation of Eq. (1) forms the following equation:

$$\overline{U}^{a} = -\sum_{I}^{N}\overline{U}^{a,I,I} - \sum_{I>J}^{N}\left(\overline{U}^{a,IJ,IJ} - \overline{U}^{a,I,I} - \overline{U}^{a,J,J}\right) + \sum_{I>J}^{N}\left(\overline{U}^{a,IJ,IJ} - \overline{U}^{a,I,IJ} - \overline{U}^{a,J,IJ}\right). \tag{19}$$

$\overline{U}^{a}$ is zero when no ESP approximations are applied or when all the ESPs are approximated uniformly (e.g., with the ESP-PTC approximation).[80] Otherwise, $\overline{U}^{a}$ is only approximately equal to zero. $\overline{U}^{a}$ is regarded as a compensation term arising by defining the internal fragment energies and the ESP contribution separately in Eq. (1). If $\overline{U}^{a}=0$, then in Eq. (16) the dimer-related terms $\overline{U}^{a,IJ,IJ}-\overline{U}^{a,I,IJ}-\overline{U}^{a,J,IJ}$ need not be evaluated, and the only terms that require the solution of CPHF equations come from the monomers, $U_{ri}^{a,I}$.

2.2 Coupled-perturbed Hartree-Fock equations in FMO

Calculating the fully analytic FMO energy gradients (with the aforementioned conditions on the ESP approximations that lead to $\overline{U}^{a}=0$) requires only the response terms due to the monomers, i.e., $U_{ri}^{a,I}$. These terms can be obtained using the diagonal nature of the monomer Fock matrices. The purpose of this subsection is to derive the CPHF equations for $U_{ri}^{a,I}$ in the framework of the FMO method.

For monomer *I*, the corresponding Fock matrix rewritten in terms of MOs is

$$F_{ij}^{I}=F_{ij}^{'I}+V_{ij}^{I} \tag{20}$$

$$=\tilde{h}_{ij}^{I}+\sum_{k\in I}^{\text{occ}}\left[2(ij\,|\,kk)-(ik\,|\,jk)\right]+P_{ij}^{I},$$

where the one-electron Hamiltonian in FMO is

$$\tilde{h}_{ij}^{I}=h_{ij}^{I}+V_{ij}^{I}. \tag{21}$$

$F_{ij}^{'I}$ is the internal Fock matrix (i.e., the full matrix F_{ij}^{I} with ESP subtracted) and P_{ij}^{I} is the projection operator matrix.

The differentiation of Eq. (20) with respect to nuclear coordinate a is

$$\frac{\partial F_{ij}^{I}}{\partial a}=\frac{\partial}{\partial a}\left(\tilde{h}_{ij}^{I}+\sum_{k\in I}^{\text{occ}}\left[2(ij\,|\,kk)-(ik\,|\,jk)\right]+P_{ij}^{I}\right). \tag{22}$$

After some algebra, Eq. (22) leads to

$$\frac{\partial F_{ij}^{I}}{\partial a}=F_{ij}^{a,I}+\sum_{k\in I}^{\text{occ+vir}}\left(U_{ki}^{a,I}F_{kj}^{I}+U_{kj}^{a,I}F_{ik}^{I}\right)+\sum_{k\in I}^{\text{occ+vir}}\sum_{l\in I}^{\text{occ}}U_{kl}^{a,I}A_{ij,kl}^{'} \tag{23}$$

$$+\sum_{K\neq I}\sum_{k\in K}^{\text{occ+vir}}\sum_{l\in K}^{\text{occ}}U_{kl}^{a,K}\,4(ij\,|\,kl),$$

In Eq. (23) a superscript *a* indicates a derivative with respect to coordinate *a*. The (molecular) orbital Hessian contribution is given by

$$A_{ij,kl}^{'}=4(ij\,|\,kl)-(ik\,|\,jl)-(il\,|\,jk), \tag{24}$$

and the Fock derivative is

$$F_{ij}^{a,I}=h_{ij}^{a,I}+V_{ij}^{a,I}+\sum_{k\in I}^{\text{occ}}\left[2(ij\,|\,kk)^{a}-(ik\,|\,jk)^{a}\right]+P_{ij}^{a,I}, \tag{25}$$

Eq. (25) is derived from Eq. (10.7) of Ref. [88]. The derivative of the one-electron Hamiltonian, $h_{ij}^{a,I}$ and the derivative two-electron integral, $(ij\,|\,kl)^{a}$ are defined as

$$h_{ij}^{a,I}=\sum_{\mu\nu\in I}C_{\mu i}^{I*}C_{\nu j}^{I}\frac{\partial h_{\mu\nu}^{I}}{\partial a}, \tag{26}$$

$$(ij\,|\,kl)^{a}=\sum_{\mu\nu\rho\sigma\in I}C_{\mu i}^{I*}C_{\nu j}^{I}C_{\rho k}^{I*}C_{\sigma l}^{I}\frac{\partial(\mu\nu\,|\,\rho\sigma)}{\partial a}, \tag{27}$$

(see Section 4.5 of Ref. 88 for details). The ESP derivative $V_{ij}^{a,I}$ is defined as follows:

$$V_{ij}^{a,I}=\sum_{K\neq I}\left(u_{ij}^{a,K}+\sum_{k\in K}^{\text{occ}}2\left(ij\,|\,kk\right)^{a}\right). \tag{28}$$

F_{ij}^{I} is zero by virtue of SCF equations, if $i \neq j$. The HOP derivative $P_{ij}^{a,I}$ and the one-electron contribution in the ESP derivative $u_{ij}^{a,K}$ are defined analogously to $h_{ij}^{a,I}$, as MO-transformed derivative integrals (see Eq. (26)).

After further algebra, Eq. (23) leads to:

$$\frac{\partial F_{ij}^{I}}{\partial a} = F_{ij}^{a,I} - \left(\varepsilon_j^I - \varepsilon_i^I\right) U_{ij}^{a,I} - S_{ij}^{a,I}\varepsilon_j^I - \sum_{k,l \in I}^{\text{occ}} S_{kl}^{a,I}\left[2(ij\,|\,kl) - (ik\,|\,jl)\right] + \sum_{k\in I}^{\text{vir}}\sum_{l\in I}^{\text{occ}} U_{kl}^{a,I} A'_{ij,kl} \tag{29}$$

$$-\sum_{K\neq I}\sum_{k,l\in K}^{\text{occ}} 2S_{kl}^{a,K}(ij\,|\,kl) + \sum_{K\neq I}\sum_{k\in K}^{\text{vir}}\sum_{l\in K}^{\text{occ}} U_{kl}^{a,K}\, 4(ij\,|\,kl),$$

where ε_i^I is the orbital energy of MO *i* on fragment *I* and the following relation[88] is used

$$S_{ij}^{a,X} + U_{ji}^{a,X} + U_{ij}^{a,X} = 0. \tag{30}$$

Eq. (29) contains two types of unknown values $U_{kl}^{a,X}$ to be solved: $U_{kl}^{a,I}$ for the target fragment and $U_{kl}^{a,K}$ from the remaining fragments. Therefore it is necessary to collect $\partial F_{ij}^{X}/\partial a$ of all the monomer fragments to construct and solve the complete CPHF equations. Consequently, a set of CPHF equations have the dimension of the whole system given in the matrix form as

$$\mathbf{A}\mathbf{U}^{a} = \mathbf{B}_0^{a}, \tag{31}$$

where the fragment diagonal and off-diagonal blocks of matrix $\mathbf{A}$ are given in Eqs. (32) and (33), respectively,

$$A_{ij,kl}^{I,I} = \delta_{ik}\delta_{jl}\left(\varepsilon_j^I - \varepsilon_i^I\right) - \left[4(ij\,|\,kl) - (ik\,|\,jl) - (il\,|\,jk)\right], \tag{32}$$

and

$$A_{ij,kl}^{I,K} = -4(ij\,|\,kl), \tag{33}$$

where Eq. (32) comes from the MOs of only the target fragment *I* and Eq. (33) comes from the ESP acting upon I . The $ij\in I$ element of vector $\mathbf{B}_0^a$ is

$$B_{0,ij}^{a,I} = F_{ij}^{a,I} - S_{ij}^{a,I}\varepsilon_j^I - \sum_{kl\in I}^{\text{occ}} S_{kl}^{a,I}\left[2(ij\,|\,kl)-(ik\,|\,jl)\right] - \sum_{K\neq I}\sum_{kl\in K}^{\text{occ}} 2S_{kl}^{a,K}(ij\,|\,kl). \tag{34}$$

2.3 Z-vector method in FMO

It is impractical to solve the CPHF equations of Eq. (31) for all nuclear coordinates of a large system. To avoid this difficulty, the Z-vector method is applied to the FMO CPHF equations.[88]

In Eq. (16), the terms involving the unknowns $U_{ri}^{a,K}$ are collected for all of the dimer fragments *IJ*. The resulting contribution to the FMO energy gradient leads to

$$\Re^a = 4\sum_{I>J}^{N}\sum_{K\neq IJ}\sum_{\mu\nu\in IJ}\sum_{r\in K}^{\text{vir}}\sum_{i\in K}^{\text{occ}}\Delta D_{\mu\nu}^{IJ} U_{ri}^{a,K}\left(\mu\nu\,|\,ri\right) \tag{35}$$

$$= \sum_{K}\sum_{r\in K}^{\text{vir}}\sum_{i\in K}^{\text{occ}} U_{ri}^{a,K} X_{ri}^{K},$$

where X_{ri}^K is defined as

$$X_{ri}^K = 4\sum_{(I>J)\neq K}^{N}\sum_{\mu\nu\in IJ}\Delta D_{\mu\nu}^{IJ}\left(\mu\nu\,|\,ri\right). \tag{36}$$

It is convenient to express Eq. (35) in vector form:

$$\Re^a = \sum_{K}\sum_{r\in K}^{\text{vir}}\sum_{i\in K}^{\text{occ}} U_{ri}^{a,K} X_{ri}^{K} = \mathbf{X}^T\mathbf{U}^a \tag{37}$$

$$= \mathbf{X}^T\mathbf{A}^{-1}\mathbf{B}_0^a$$

$$= \mathbf{Z}^T\mathbf{B}_0^a.$$

This reduces the CPHF problem for solving Eq. (31) to a set of simultaneous equations:

$$\mathbf{A}^T\mathbf{Z} = \mathbf{X}. \tag{38}$$

It is still time-consuming to solve Eq. (38) directly, because it has the dimension of the entire system. However, taking advantage of the decoupled nature of the FMO method, a more clever approach can be considered by separating the diagonal (I,I) and off-diagonal (K,I) blocks of $\mathbf{A}$ in Eq. (38):

$$\sum_{k\in I}^{\text{vir}}\sum_{l\in I}^{\text{occ}} A_{kl,ri}^{I,I} Z_{kl}^{I} = X_{ri}^{I} - \sum_{K\neq I}^{all}\sum_{k\in K}^{\text{vir}}\sum_{l\in K}^{\text{occ}} A_{kl,ri}^{K,I} Z_{kl}^{K}, \tag{39}$$

or in matrix form:

$$\left(\mathbf{A}^{I,I}\right)^{T}\mathbf{Z}^{I} = \mathbf{X}^{\prime I}, \tag{40}$$

where

$$\mathbf{X}^{\prime I} = \mathbf{X}^{I} - \sum_{K\neq I}\left(\mathbf{A}^{K,I}\right)^{T}\mathbf{Z}^{K}. \tag{41}$$

Eq. (37), using definitions in Eqs. (34,38,40,41), gives the final formulation of the terms that are required to complete the FMO analytic gradient. The solution of these equations is accomplished as follows, illustrated in Fig. 1. By taking the I diagonal blocks of matrix **A** and solving $\left(\mathbf{A}^{I,I}\right)^{T}\mathbf{Z}^{I} = \mathbf{X}^{I}$, one finds the initial $\mathbf{Z}^{I}$. $\mathbf{X}^{\prime I}$ is computed to solve Eq. (40). The external unknowns $\mathbf{Z}_{kl}^{K}$ in the last term of Eq. (39) are frozen and this equation is decoupled for each fragment *I*. **Z** is obtained by solving Eq. (40) for all fragments independently, and then $\mathbf{X}^{\prime I}$ is updated with these new values of $\mathbf{Z}^{K}$ for the next step; the calculations are then repeated until all elements in the Z-vector are self-consistent. This is similar in both procedure and computational cost to the self-consistent charge (SCC) procedure in the monomer energy calculation (and it also bears a similarity to SCF), so it will be called the self-consistent Z-vector (SCZV) method. The preconditioned conjugate-gradient (CG) method is applied to solve Eq. (40). The convergence test is made for all Z-vector elements. If the root mean square deviation (RMSD) of $\mathbf{Z}^{I,\mathrm{new}} - \mathbf{Z}^{I,\mathrm{old}}$ is larger than a threshold, the procedure returns to step 2 in Fig. 1.

The SCZV method is parallelized using the generalized distributed data interface (GDDI).[89] Because of its iterative decoupled nature, the computation time of SCZV is comparable to that of SCC.

2.4 Application to the electrostatic dimer approximation

The previous subsection presented a derivation in which the analytic FMO gradient was derived with no approximations. In this subsection, the electrostatic dimer (ES-DIM) approximation for the fully analytic energy gradients is introduced, and it is shown that the response term arising from the ES-DIM approximation need not to be considered, because they cancel out with the response term from Eq. (19).

For separated fragments *I* and *J*, if the distance R_{IJ} (defined as the distance between the closest atoms in *I* and *J* divided by the sum of their van-der-Waals atomic radii) is larger than the threshold value $L_{\mathrm{ES-DIM}}$ in the ES-DIM approximation, the internal pair interaction energy, i.e., the corresponding summand in the second sum on the right hand side of Eq. (1) can be replaced by

$$E'_{IJ} - E'_{I} - E'_{J} \approx \mathrm{Tr}(\mathbf{D}^{I}\mathbf{u}^{J}) + \mathrm{Tr}(\mathbf{D}^{J}\mathbf{u}^{I}) + \sum_{\mu\nu\in I}\sum_{\lambda\sigma\in J} D^{I}_{\mu\nu} D^{J}_{\lambda\sigma}(\mu\nu|\lambda\sigma) + \Delta E^{\mathrm{NR}}_{IJ}, \qquad (42)$$

where the nuclear repulsion (NR) term $\Delta E^{\mathrm{NR}}_{IJ} = E^{\mathrm{NR}}_{IJ} - E^{\mathrm{NR}}_{I} - E^{\mathrm{NR}}_{J}$. In addition, the corresponding *IJ* term in the third sum of Eq. (1) cancels out because $\Delta\mathbf{D}^{IJ} = 0$. The differentiation of Eq. (42) with respect to nuclear coordinate *a* without considering the response term is given elsewhere.[83] Therefore, it is sufficient here to discuss how the unknown orbital response terms in the FMO gradient are formulated. The collection of the response terms in the FMO gradient yields

$$\overline{U}^{a} + \Re^{a} = -\sum_{I}^{N} \overline{U}^{a,I,I} - \sum_{I>J}^{N} \left(\overline{U}^{a,IJ,IJ} - \overline{U}^{a,I,I} - \overline{U}^{a,J,J} \right) + \sum_{I>J}^{N} \left(\overline{U}^{a,IJ,IJ} - \overline{U}^{a,I,IJ} - \overline{U}^{a,J,IJ} \right) \tag{43}$$

$$+4 \sum_{I>J}^{N} \sum_{K \neq IJ} \sum_{\mu\nu \in IJ} \sum_{r \in K}^{\text{vir}} \sum_{i \in K}^{\text{occ}} \Delta D_{\mu\nu}^{IJ} U_{ri}^{a,K} \left(\mu\nu \,|\, ri \right).$$

As mentioned before, $\overline{U}^{a} = 0$ only if there are no approximations to the ESPs. In the case of the ES-DIM approximation, Eq. (43) should be reformulated.

When the ES-DIM approximation is applied to avoid SCF calculations for dimers separated by more than $L_{\text{ES-DIM}}$, $\overline{U}^{a}$ in Eq. (19) can be rewritten as

$$\overline{U}^{a} = -\sum_{I}^{N} \overline{U}^{a,I,I} - \sum_{I>J(R_{IJ} \le L_{\text{ES-DIM}})}^{N} \left(\overline{U}^{a,IJ,IJ} - \overline{U}^{a,I,I} - \overline{U}^{a,J,J} \right) + \sum_{I>J(R_{IJ} \le L_{\text{ES-DIM}})}^{N} \left(\overline{U}^{a,IJ,IJ} - \overline{U}^{a,I,IJ} - \overline{U}^{a,J,IJ} \right) \tag{44}$$

$$= -\sum_{I}^{N} \overline{U}^{a,I,I} + \sum_{I>J(R_{IJ} \le L_{\text{ES-DIM}})}^{N} \left(\overline{U}^{a,I,I(J)} + \overline{U}^{a,J,J(I)} \right) \neq 0,$$

where the partial terms

$$\overline{U}^{a,X,X(Y)} = 4 \sum_{i \in X}^{\text{occ}} \sum_{r \in X}^{\text{vir}} U_{ri}^{a,X} \left(u_{ri}^{Y} + v_{ri}^{Y} \right), \tag{45}$$

describe the contribution of a single fragment denoted *Y* to the full sum over all *Y* in $\overline{U}^{a,X,X}$.

Also, the following relation can be used,

$$\overline{U}^{a,I,I} - \overline{U}^{a,I,IJ} = \overline{U}^{a,I,I(J)}, \tag{46}$$

because (see Eq. (14)) the ESP for IJ (V^{IJ}) runs over all fragments excluding *I* and *J*, whereas the ESP for *I* excludes the contribution from *I*. Therefore, in the difference expression only *J* terms remain.

$$V_{ri}^{I} - V_{ri}^{IJ} = V_{ri}^{I,I(J)} \equiv u_{ri}^{J} + v_{ri}^{J}. \tag{47}$$

$\overline{U}^{a}$ in Eq. (44) is in general non-zero and can be further simplified to

$$\overline{U}^{a} = -\sum_{I}^{N} \overline{U}^{a,I,I} + \sum_{I>J(R_{IJ} \le L_{\text{ES-DIM}})}^{N} \left(\overline{U}^{a,I,I(J)} + \overline{U}^{a,J,J(I)} \right) \tag{48}$$

$$= -\sum_{I>J(R_{IJ} > L_{\text{ES-DIM}})}^{N} \left(\overline{U}^{a,I,I(J)} + \overline{U}^{a,J,J(I)} \right),$$

where the completeness relation is used:

$$\sum_{I}^{N} \overline{U}^{a,I,I} = \sum_{I}^{N} \sum_{J \ne I}^{N} \overline{U}^{a,I,I(J)} = \sum_{I>J}^{N} \left(\overline{U}^{a,I,I(J)} + \overline{U}^{a,J,J(I)} \right). \tag{49}$$

For the derivatives of Eq. (42) the collection of response terms for all *IJ* is

$$\sum_{I>J(R_{IJ} > L_{\text{ES-DIM}})}^{N} \left[\mathrm{Tr}\left(\frac{\partial \mathbf{D}^{I}}{\partial a} \mathbf{u}^{J}\right) + \mathrm{Tr}\left(\frac{\partial \mathbf{D}^{J}}{\partial a} \mathbf{u}^{I}\right) \right. \tag{50}$$

$$\left. + \sum_{\mu\nu \in I} \sum_{\lambda\sigma \in J} \frac{\partial D_{\mu\nu}^{I}}{\partial a} D_{\lambda\sigma}^{J} (\mu\nu | \lambda\sigma) + \sum_{\mu\nu \in I} \sum_{\lambda\sigma \in J} D_{\mu\nu}^{I} \frac{\partial D_{\lambda\sigma}^{J}}{\partial a} (\mu\nu | \lambda\sigma) \right]$$

$$= \sum_{I>J(R_{IJ} > L_{\text{ES-DIM}})}^{N} \left(\overline{U}^{a,I,I(J)} + \overline{U}^{a,J,J(I)} \right) - 2 \sum_{I \ne J(R_{IJ} > L_{\text{ES-DIM}})}^{N} \sum_{ij \in I}^{\text{occ}} S_{ji}^{a,I} \left(u_{ji}^{J} + v_{ji}^{J} \right).$$

The first term on the right hand side of Eq. (50) cancels out with $\overline{U}^{a}$ in Eq. (48). Since the derivative terms of Eq. (42) are already implemented,[83] one can obtain the fully analytic energy gradients for the ES-DIM approximation by calculating the following response contribution to the gradient:

$$\overline{U}^{a} + \Re^{a} = 4 \sum_{I>J(R_{IJ} \le L_{\text{ES-DIM}})}^{N} \sum_{K \ne IJ} \sum_{\mu\nu \in IJ} \sum_{r \in K}^{\text{vir}} \sum_{i \in K}^{\text{occ}} \Delta D_{\mu\nu}^{IJ} U_{ri}^{a,K} (\mu\nu | ri). \tag{51}$$

2.5 Implementation

To further facilitate solution of the SCZV equations, it is useful to reformulate them in the AO basis, thereby avoiding the expensive integral transformation.[90] Examining Eqs. (39,32,33), the main computational effort is spent on two-electron integral terms like $\sum_{kl}(kl\,|\,ri)Z_{kl}^{K}$ in Eq. (39). By utilizing the MO i expansion over AOs μ,

$$\left|i\right\rangle = \sum_{\mu} C_{\mu i}\left|\mu\right\rangle. \tag{52}$$

The two-electron integral terms in Eq. (39) can be transformed according to

$$\sum_{k\in K}^{\text{vir}}\sum_{l\in K}^{\text{occ}}(kl\,|\,ri)Z_{kl}^{K} = \sum_{k\in K}^{\text{vir}}\sum_{l\in K}^{\text{occ}}C_{\mu k}^{K*}C_{\nu l}^{K}(\mu\nu\,|\,ri)Z_{kl}^{K} = \sum_{\mu\nu}(\mu\nu\,|\,ri)\tilde{Z}_{\mu\nu}^{K}, \tag{53}$$

where

$$\tilde{Z}_{\mu\nu}^{K} = \sum_{k\in K}^{\text{vir}}\sum_{l\in K}^{\text{occ}}C_{\mu k}^{K*}Z_{kl}^{K}C_{\nu l}^{K}. \tag{54}$$

Using Eq. (53) avoids the full transformation of the two-electron integrals to the MO basis, which leads to a significant reduction of the computation time and memory. However, $\tilde{Z}_{\mu\nu}^{I}$ is not symmetric; this is inconvenient and can be further improved by symmetrizing it:

$$\bar{Z}_{\mu\nu}^{I} = \frac{1}{2}\left(\tilde{Z}_{\mu\nu}^{I} + \tilde{Z}_{\nu\mu}^{I}\right). \tag{55}$$

It is possible to rewrite the SCZV equations (Eq. (40)) using the symmetrized local Z-vector element $\bar{Z}_{\mu\nu}^{K}$. $\bar{Z}_{\mu\nu}^{K}$ corresponds to the density matrix element $D_{\mu\nu}$ in typical integral programs, and therefore the SCZV method can be implemented using standard CPHF codes.

The Cauchy-Schwarz inequality, which estimates the value of $(\mu\nu|\rho\sigma)$ based on the values of a smaller set of integrals with repeated indices, can be used in the SCZV to obtain a further reduction of computation time. The Cauchy-Schwarz inequality screening is usually applied to the maximum element of the factor by which the integrals of interest are multiplied. The SCZV procedure is more efficient because the Z-vector elements normally have smaller values than the density matrix elements, and therefore, the Cauchy-Schwarz integral screening can skip more terms. In the implementation of the response contribution, Eq. (37), the direct (AO basis) algorithm and the Cauchy-Schwarz inequality for the calculation of the two-electron integrals are included. As a result, the calculations do not need a large amount of disk space or memory.

3. Computational details

To verify that the response contribution that has been derived and implemented in this study makes the FMO energy gradients fully analytic, analytic gradients are compared with numerical gradients for molecular systems taken from previous studies:[80, 91, 92] $(H_2O)_{64}$, the α-helix conformation of the alanine decamer $(ALA)_{10}$ capped with -OCH_3 and -$NHCH_3$ groups, chignolin (PDB ID: 1UAO) solvated by 157 water molecules, and the Trp-cage miniprotein construct (PDB ID: 1L2Y). The structures of $(ALA)_{10}$ and 1L2Y were taken from earlier works.[83, 92] Numerical gradients were computed with double differencing and a coordinate step of 0.005 Å (except for $(H_2O)_{64}$ with 6-311G(d), where a 0.0005 Å step was used).

For the fragmentation of a system that does not require fragmenting covalent bonds, such as a water cluster, the HOP operator is not needed. For the first test calculation, a water molecule in $(H_2O)_{64}$ is assigned to a fragment. The geometrical structure of $(H_2O)_{64}$ was modeled by HyperChem, optimized by Amber[94,93] and then reoptimized at the FMO-RHF/6-31G level.[80] The optimized structure of $(H_2O)_{64}$ is depicted in Fig. 2a.

For molecular systems in which fragmentation occurs across covalent bonds, the hybrid orbital operator contributes to the gradients both directly and via the response term from the Fock derivative, Eq. (25). The α-helix conformation of $(ALA)_{10}$ with some intramolecular hydrogen bonds (shown in Fig. 2b) is chosen because in the case of incomplete analytic gradients it is expected to have large errors in the gradients compared to the β-strand or extended structures. Because this system is relatively small, the validity of the analytic gradients without approximations can also be accessed.

The FMO method has been interfaced with the effective fragment potential (EFP) method, which explicitly treats solvent molecules by adding a one-electron potential to the Hamiltonian.[91, 94] Chignolin is immersed in 157 water molecules described by EFPs, and its structure is optimized using the combined FMO/EFP method at the RHF/cc-pVDZ level.[91] The optimized structure in Fig. 2c reproduces the PDB NMR structure well.[80]

Fig. 2d depicts the structure of 1L2Y. Because 1L2Y is the largest system treated with the FMO method in this study, it is an appropriate test case for the application of the electrostatic dimer approximation which is necessary for efficient computations of large systems. In this calculation, the threshold for the ES-DIM approximation $L_{\mathrm{ES-DIM}}$ was set to the default value, 2.0 and all other approximations were turned off.[34]

For systems fragmented across covalent bonds, i.e., $(ALA)_{10}$, chignolin and 1L2Y, a one residue/one fragment partition was adopted. The gradient calculations for

$(H_2O)_{64}$, $(ALA)_{10}$, hydrated chignolin, and 1L2Y were performed at the RHF/6-31G(d) level and diffuse functions were added to the carboxyl groups of 1L2Y. Additionally, RHF/6-311G(d) was also used to calculate the gradients for $(H_2O)_{64}$.

The computation time of the SCZV procedure is expected to be comparable to that of the SCC calculation. Thus, the timings of the calculations of fully analytic gradients in which both the SCC and SCZV steps were included were measured and compared. The timing calculations used the 32 node Soroban cluster with Intel Pentium 4 CPU 3.2 GHz nodes connected by Gigabit Ethernet. Table I lists separately for monomers and dimers the number of GDDI groups in the gradient calculation for each system (in GDDI, in order to improve parallel efficiency, all computer nodes are divided into groups and individual monomer and dimer calculations are distributed dynamically among these groups). Note that the number of GDDI groups in the SCZV step is the same as in the SCC step. The parallel efficiency is calculated for the gradient and SCZV calculations for $(H_2O)_{64}$ using 1, 2, 4, 8, 16 and 32 nodes of the Soroban cluster. For this calculation, the number of GDDI groups is equal to the number of nodes.

4. Results and discussion

4.1 Fully analytic energy gradients without approximations

In this subsection, the fully analytic gradients without approximations is discussed. It is important to numerically verify that the gradients are fully analytic using $\overline{U}^a = 0$ (Eq. 19).

As mentioned previously, for $(H_2O)_{64}$, the energy gradients do not involve the HOP term and only the response term contributes to the analytic gradients. In Table II, the root mean square (RMS) value in the numerical gradients became identical with the new analytic gradients (0.005997 a.u.). However, the RMS value in the old analytic gradients, in which only the response contribution is neglected, deviates by 0.0001 a.u. from the numerical and the analytic ones. For the maximum absolute gradient values (MAX grad.), the new analytic gradient value is in good agreement with the corresponding numerical value, while the conventional value differs by 0.00025 a.u. The latter is not a negligible error when aiming for fully analytic gradients. The root mean square (RMS) of the errors for the new analytic gradient relative to the numerical gradient (the RMS error in the analytic gradients) is negligibly small (0.000011 a.u.), which is an improvement by a factor of 20 over the RMS error in the old analytic gradients (0.000231 a.u.). This improvement is visualized in Fig. 3a, which plots the errors of the new analytic gradient and the old analytic gradient relative to the numeric gradient against the total 576 gradient elements. The new analytic gradient values converge to zero, while the old analytic gradient values have large deviations.

For systems fragmented across covalent bonds, the HOP contribution to the response term must be considered. $(ALA)_{10}$ is such a system and due to its size is a good test for calculating numerical gradients without approximations at a relatively moderate computational cost. Note that the old analytic gradient method that is illustrated here did include the direct contribution of HOP derivatives to the gradients, since this contribution was introduced in a previous study.[84] Table II shows that the three types of gradients are in good agreement. Even though the RMS value in the old analytic gradients is very close to that of numerical gradients, the RMS errors and maximum absolute gradient error for the old analytic gradient deviates by significant amounts (0.000160 a.u. and 0.000580 a.u., respectively). On the other hand, the very small errors in the new analytic gradient values indicate that they are fully analytic and that the HOP contribution to the response term is properly included. In Fig. 3b, as in Fig. 3a, one can see that the new analytic gradients are fully analytic for every gradient element. Comparing Fig. 3b ($(\text{ALA})_{10}$) with Fig. 3a (the water cluster), the former has smaller gradient errors for the old analytic gradients. Since the response term is related to the ESPs, the environmental potential affects the water clusters more significantly than the peptide.

Most biological processes occur in aqueous solution. To model one of these processes, one may consider a protein in a water droplet. For molecular dynamics and geometry optimization processes, an accurate solvent model must be combined with the application of FMO to the solute. As the first test calculation toward this goal, hydrated chignolin is chosen for the FMO/EFP framework. In order to obtain the fully analytic energy gradients in this framework, it is necessary to add the EFP derivatives to the Fock derivative term, Eq. (25) and probably to modify the **A** matrix in Eq. (38). In this study, however, the EFP-related many-body polarization contribution to the FMO ESP response term was neglected. Therefore, the FMO/EFP energy gradients are not fully analytic. So, the accuracy of the FMO/EFP new energy gradients is shown only for the solute (FMO) molecule (chignolin). As seen in Table II, the accuracy of the FMO/EFP new energy gradients is similar to that for the full treatment of FMO, but the maximum absolute gradient error is larger (0.000092 a.u.) than those for the other test systems, and there are slight deviations in the FMO/EFP new analytic gradients in Fig. 3c. Nevertheless, the maximum absolute new analytic gradient error is improved by a factor of 16 compared to the old analytic gradient value. This encouraging result provides motivation to develop the fully analytic energy gradients for FMO/EFP as well as FMO combined with the polarizable continuum model (PCM).[92, 95]

For the chosen systems, the wall-clock times required for the SCC, the SCZV, and the total FMO calculation were measured. Table III shows that for the gradient calculation without approximations for $(H_2O)_{64}$, the SCC calculation took 24.3 sec., which is comparable to 29.5 sec. in the corresponding SCZV calculation. These times are small relative to the total computational time of over 400 sec. For $(ALA)_{10}$, the SCZV calculation takes only 64% of the computation time of the corresponding SCC calculation. For hydrated chignolin, the SCZV calculation requires a similar percentage of the computation time. These results illustrate why the Z-vectors converge more rapidly; the calculation of two-electron integrals is faster because the Cauchy-Schwarz inequality is more efficient when applied to the Z-vectors rather than to the monomer densities (used in ESPs or two-electron integrals for monomers).

4.2 Fully analytic energy gradients in the ES dimer approximation

The FMO energy gradients have been shown to be fully analytic by introducing the response contribution. The computation time in the calculation of the response term is comparable to or less than that required for the SCC calculation. This implies that although it is practical to calculate the response term itself, it is still expensive to calculate the fully analytic energy gradients for a larger molecule because of the difficulty in performing a large number of dimer SCF calculations without approximations.

As discussed above, the fully analytic energy gradients with the ES-DIM approximation have been derived. The purpose of this subsection is to check numerically that the FMO energy gradients are fully analytic within the ES-DIM approximation and to discuss the timings.

The ES-DIM approximation was first applied to $(H_2O)_{64}$ using both the 6-31G(d) and 6-311(d) basis sets. Table II shows that with $L_{\mathrm{ES-DIM}}=2.0$, the RMS value, the MAX gradient value and the RMS error for the new analytic gradients are identical to those without approximations. Additionally, the maximum gradient error is negligibly small. These results imply that the ES-DIM approximation is a suitable choice for this system.

The errors for the old analytic gradient increase with the basis set, as can be seen in Table II. For example, the maximum gradient error increases from 0.000975 to 0.002280 when going from 6-31G(d) to 6-311(d). The error in the new analytic vs numeric gradient is about 15 times smaller and is probably due to the error in the numerical gradient itself. There is also no basis set effect on the error when the new analytic gradient is employed. The pictorial representations of the errors in Fig. 3a and 3e demonstrate the quality of the gradients.

For another system requiring fragmentation across covalent bonds, consider 1L2Y, which consists of 20 amino acid residues. Since the calculation of numerical gradients for such a relatively large molecule is time-consuming, a subsystem is chosen, i.e., the 38 atoms defining 19 detached bonds between 20 fragments (for which atoms the error in the old analytic gradient is the largest as found in the earlier study[84]). With $L_{\mathrm{ES-DIM}}=2.0$, there are 92 SCF and 98 approximated (ES-DIM) dimers. In Table II (see also Fig. 3d), the corresponding RMS value and the maximum absolute gradient value show that the new analytic gradients are fully analytic in comparison to the numerical values. The corresponding RMS and MAX gradient errors are similar in accuracy to the fully analytic gradient values of the other systems. The errors are much improved compared to those from the old analytic gradient calculation; especially for the MAX gradient which is more accurate by a factor of 27, indicating a significant contribution from the response term in this system.

As shown in Table III, for $(H_2O)_{64}$, the total wall-clock time for the fully analytic gradient calculation with the approximation (261.0 sec.) is less than the timing without approximations (467.2 sec.). In comparing the SCZV and the SCC calculation for this water cluster, it is reasonable that the former took less computation time. When using the approximation, the ratio of the computation time in SCZV to SCC is normally less than 1. This implies that the SCZV calculation is faster; this trend is independent of the ES-DIM approximation. For 1L2Y, the SCZV calculations took approximately 70% of the time required for the SCC calculations, and it is expected that this ratio will decrease for larger systems.

For $(H_2O)_{64}$, the parallel efficiency $S(n)$, shown in Fig. 4, was calculated using the following expression:

$$S(n) = \frac{T_1/T_n}{n} \times 100, \tag{56}$$

where T_1 and T_n represent the computation time using 1 node and n nodes, respectively. 100 % efficiency means that the calculation is n times faster on n nodes. The results show that for $(H_2O)_{64}$ the parallel efficiency is over 97.8 % for all numbers of nodes (n=1, 2, 4, 8, 16 and 32) both in the total gradient calculation (solid line) and SCZV calculation (dashed line). For n=16, the parallel efficiency in the SCZV calculation drops slightly from that for n=8. For $(H_2O)_{64}$, 64 SCZV calculations should be distributed into 16 nodes (divided into 16 GDDI groups). However, each SCZV calculation takes a different amount of time, because the number of iterations and the integral screening depends upon the fragment; the GDDI calculations are dynamically divided over groups, and there is some granularity (i.e., some groups finish ahead of others). This is why the parallel efficiency drops at n=16. The superlinear scaling over 100 % for a small number of nodes is also observed in FMO-RHF calculations[89] and is thought to originate from external factors like CPU cache efficiency.

5 Conclusions

The CPHF equations and the Z-vector equations in the FMO framework have been derived to compute the fully analytic energy gradients. One outcome of this study is the derivation and implementation of the SCZV equations, by which the time-consuming Z-vector equations of the whole system reduce to those of the monomer fragments. Additionally, the SCZV procedure is parallelized by the use of GDDI.[89] It was shown that the FMO energy gradients are fully analytic in the electrostatic dimer approximation. This leads to a significant reduction of the total computation time. Nearly fully analytic energy gradients have been successfully implemented for the combined FMO/EFP method as well.

The use of the SCZV procedure is not limited to the gradient calculation. The calculation of the second derivative (Hessian) matrix is necessary to calculate important properties such as the IR spectrum, Raman spectrum and NMR chemical shifts. To calculate the fully analytic Hessian, one must solve the CPHF equations, and the SCZV procedure would play an essential role. The SCZV procedure could also be found useful in other fragmentation methods that require the response term (some methods[87, 96] do not need it with respect to the field, although the Mulliken charge derivatives do require it[97, 80]).

The analytic gradient equations have been derived at the Hartree-Fock level of theory. For proteins, dispersion is crucial for determining the folded structure[58] and for protein-ligand binding. Therefore, the fully analytic energy gradient should be extended to electron correlation methods such as MP2. For practical calculations, such as FMO-MD to study protein folding, it will be necessary to develop the fully analytic gradient with the point charge (ESP-PTC) approximation.

As mentioned earlier, MD simulations are an important application of FMO, however, FMO-MD has been limited mainly to molecular clusters.[70, 71, 72, 75, 76, 77, 78] As found in this study, with the introduction of fully analytic energy gradients, reliable MD simulation with perfect energy conservation will now be possible.

6. Acknowledgment

This work has been supported by the Next Generation Super Computing Project, Nanoscience Program (MEXT, Japan), and by a US National Science Foundation Petascale Applications grant. KB is supported by a US Department of Energy Computational Science Graduate Fellowship.

References

1. D. A. Pearlman, D. A. Case, J. W. Caldwell, W. S. Ross, T. E. Cheatham, S. Debolt, D. Ferguson, G. Seibel, and P. Kollman, Comput. Phys. Commun. **91**, 1 (1995).

2. P. Kollman, I. Massova, C. Reyes, B. Kuhn, S. H. Huo, L. Chong, M. Lee, T. Lee, Y. Duan, W. Wang, O. Donini, P. Cieplak, J. Srinivasan, D. A. Case, and T. E. Cheatham, Acc. Chem. Res. **33**, 889 (2000).

3. D. Bashford and D. A. Case, Annu. Rev. Phys. Chem. **51**, 129 (2000).

4. J. Gao and D. Truhlar, Annu. Rev. Phys. Chem. **53**, 467 (2002).

5. A. D. Mackerell, J. Comput. Chem. **25**, 1584 (2004).

6. W. Wang, O. Donini, C. M. Reyes, and P. A. Kollman, Annu. Rev. Biophys. Biomol. Struct. **30**, 211 (2001).

7. A. Warshel, Annu. Rev. Biophys. Biomol. Struct. **32**, 425 (2003).

8. R. Car and M. Parrinello, Phys. Rev. Lett. **55**, 2471 (1985).

9. J. L. Gao, J. Phys. Chem. B **101**, 657 (1997).

10. J. L. Gao, J. Chem. Phys. **109**, 2346 (1998).

11. H. B. Schlegel, J. M. Millam, S. S. Iyengar, G. A. Voth, A. D. Daniels, G. E. Scuseria, and M. J. Frisch, J. Chem. Phys. **114**, 9758 (2001).

12. W. Xie and J. Gao, J. Chem. Theory Comput. **3**, 1890 (2007).

13. W. Xie, M. Orozco, D. G. Truhlar, and J. Gao, J. Chem. Theory Comput. **5**, 459 (2009).

14. S. Y. Wu and C. S. Jayanthi, Phys. Rep. **358**, 1 (2002).

15. S. Goedecker and G. E. Scuseria, Comp. Sci. Eng. **5**, 14 (2003).

16. D. Hankins, J. W. Moskowitz, and F. H. Stillinger, J. Chem. Phys. **53**, 4544 (1970).

17. K. Morokuma, J. Chem. Phys. **55**, 1236 (1971).

18. K. Ohno and H. Inokuchi, Theor. Chim. Acta (Berl.) **26**, 331 (1972).

19. P. Otto and J. Ladik, Chem. Phys. **8**, 192 (1975).

20. H. Stoll and H. Preuß, Theor. Chim. Acta **46**, 11 (1977).

21. Z. Barandiaran and L. Seijo, J. Chem. Phys. **89**, 5739 (1988).

22. H. Kubota, Y. Aoki, and A. Imamura, Bull. Chem. Jpn. **67**, 13 (1994).

23. H. R. Leverentz and D. G. Truhlar, J. Chem. Theory Comput. **5**, 1573 (2009).

24. M. S. Gordon, J. M. Mullin, S. R. Pruitt, L. B. Roskop, L. V. Slipchenko, and J. A. Boatz, J. Phys. Chem. B **113**, 9646 (2009).

25. R. A. Mata, H. Stoll, and B. J. C. Cabral, J. Chem. Theory Comput. **5**, 1829 (2009).

26. L. Huang, L. Massa, I. Karle, and J. Karle, Proc. Nat. Acad. Sc. U.S.A. **106**, 3664 (2009).

27. Y. Tong, Y. Mei, J. Z. H. Zhang, L. L. Duan, and Q. G. Zhang, J. Theor. Comp. Chem. **8**, 1265 (2009).

28. P. Söderhjelm and U. Ryde, J. Phys. Chem. A **113**, 617 (2009).

29. S. D. Yeole and S. Gadre, J. Chem. Phys. **132**, 094102 (2010).

30. A. Pomogaeva, F. L. Gu, A. Imamura, and Y. Aoki, Theor. Chem. Acc. **125**, 453 (2010).

31. T. Touma, M. Kobayashi, and H. Nakai, Chem. Phys. Lett. **485**, 247 (2010).

32. X. He and K. M. Merz, J. Chem. Theory Comput. **6**, 405 (2010).

33. K. Kitaura, E. Ikeo, T. Asada, T. Nakano, and M. Uebayasi, Chem. Phys. Lett. **313**, 701 (1999).

34. T. Nakano, T. Kaminuma, T. Sato, K. Fukuzawa, Y. Akiyama, M. Uebayasi, and K. Kitaura, Chem. Phys. Lett. **351**, 475 (2002).

35. D. G. Fedorov and K. Kitaura, J. Phys. Chem. A **111**, 6904 (2007).

36. D. G. Fedorov and K. Kitaura, editors, *The Fragment Molecular Orbital Method: Practical Applications to Large Molecular Systems*, CRC Press, Boca Raton, FL, 2009.

37. D. G. Fedorov and K. Kitaura, Chem. Phys. Lett. **433**, 182 (2006).

38. J. L. Pascual and L. Seijo, J. Chem. Phys. **102**, 5368 (1995).

39. Q. Cui, M. Elstner, E. Kaxiras, T. Frauenheim, and M. Karplus, J. Phys. Chem. B **105**, 569 (2001).

40. D. G. Fedorov and K. Kitaura, J. Chem. Phys. **121**, 2483 (2004).

41. Y. Mochizuki, K. Yamashita, K. Fukuzawa, K. Takematsu, H. Watanabe, N. Taguchi, Y. Okiyama, M. Tsuboi, T. Nakano, and S. Tanaka, Chem. Phys. Lett. **493**, 346 (2010).

42. D. G. Fedorov and K. Kitaura, J. Chem. Phys. **123**, 134103/1 (2005).

43. S.-I. Sugiki, N. Kurita, Y. Sengoku, and H. Sekino, Chem. Phys. Lett. **382**, 611 (2003).

44. D. G. Fedorov and K. Kitaura, Chem. Phys. Lett. **389**, 129 (2004).

45. D. G. Fedorov and K. Kitaura, J. Chem. Phys. **122**, 054108/1 (2005).

46. Y. Mochizuki, S. Koikegami, S. Amari, K. Segawa, K. Kitaura, and T. Nakano, Chem. Phys. Lett. **406**, 283 (2005).

47. Y. Mochizuki, K. Tanaka, K. Yamashita, T. Ishikawa, T. Nakano, S. Amari, K. Segawa, T. Murase, H. Tokiwa, and M. Sakurai, Theor. Chem. Acc. **117**, 541 (2007).

48. M. Chiba, D. G. Fedorov, and K. Kitaura, Chem. Phys. Lett. **444**, 346 (2007).

49. M. Chiba, D. G. Fedorov, and K. Kitaura, J. Chem. Phys. **127**, 104108 (2007).

50. M. Chiba, D. G. Fedorov, and K. Kitaura, J. Comput. Chem. **29**, 2667 (2008).

51. S. R. Pruitt, D. G. Fedorov, K. Kitaura, and M. S. Gordon, J. Chem. Theory Comp. **6**, 1 (2010).

52. B. Auer, M. V. Pak, and S. Hammes-Schiffer, J. Phys. Chem. C **114**, 5582 (2010).

53. I. Nakanishi, D. G. Fedorov, and K. Kitaura, Proteins: Struct., Funct., Bioinf. **68**, 145 (2007).

54. T. Sawada, T. Hashimoto, H. Tokiwa, T. Suzuki, H. Nakano, H. Ishida, M. Kiso, and Y. Suzuki, Glycoconj. J. **25**, 805 (2008).

55. T. Watanabe, Y. Inadomi, K. Fukuzawa, T. Nakano, S. Tanaka, L. Nilsson, and U. Nagashima, J. Phys. Chem. B **111**, 9621 (2007).

56. T. Sawada, D. G. Fedorov, and K. Kitaura, Int. J. Quant. Chem. **109**, 2033 (2009).

57. T. Ishida, D. G. Fedorov, and K. Kitaura, J. Phys. Chem. B **110**, 1457 (2006).

58. X. He, L. Fusti-Molnar, G. Cui, and K. M. J. Merz, J. Phys. Chem. B **113**, 5290 (2009).

59. D. G. Fedorov, P. V. Avramov, J. H. Jensen, and K. Kitaura, Chem. Phys. Lett. **477**, 169 (2009).

60. N. Taguchi, Y. Mochizuki, T. Nakano, S. Amari, K. Fukuzawa, T. Ishikawa, M. Sakurai, and S. Tanaka, J. Phys. Chem. B **113**, 1153 (2009).

61. T. Ikegami, T. Ishida, D. G. Fedorov, K. Kitaura, Y. Inadomi, H. Umeda, M. Yokokawa, and S. Sekiguchi, J. Comput. Chem. **31**, 447 (2010).

62. K. A. Kistler and S. J. Matsika, J. Phys. Chem. A **113**, 12396 (2009).

63. S. Amari, M. Aizawa, J. Zang, K. Fukuzawa, Y. Mochizuki, Y. Iwasawa, H. Nakata, K. Chuman, and T. Nakano, J. Chem. Inf. Comput. Sci. **46**, 221 (2006).

64. T. Yoshida, T. Fujita, and H. Chuman, Curr. Comp.-Aided Drug Des. **5**, 38 (2009).

65. T. Yoshida, Y. Munei, S. Hitaoka, and H. Chuman, J. Chem. Inf. Model. **50**, 850 (2010).

66. Q. Gao, S. Yokojima, D. G. Fedorov, K. Kitaura, M. Sakurai, and S. Nakamura, J. Chem. Theory Comp. **6**, 1428 (2010).

67. Y. Komeiji, T. Nakano, K. Fukuzawa, Y. Ueno, Y. Inadomi, T. Nemoto, M. Uebayasi, D. G. Fedorov, and K. Kitaura, Chem. Phys. Lett. **372**, 342 (2003).

68. T. Ishimoto, H. Tokiwa, H. Teramae, and U. Nagashima, Chem. Phys. Lett. **387**, 460 (2004).

69. T. Ishimoto, H. Tokiwa, H. Teramae, and U. Nagashima, J. Chem. Phys. **122**, 094905 (2005).

70. Y. Mochizuki, Y. Komeiji, T. Ishikawa, T. Nakano, and H. Yamataka, Chem. Phys. Lett. **437**, 66 (2007).

71. M. Sato, H. Yamataka, Y. Komeiji, Y. Mochizuki, T. Ishikawa, and T. Nakano, J. Am. Chem. Soc. **130**, 2396 (2008).

72. Y. Komeiji, T. Ishikawa, Y. Mochizuki, H. Yamataka, and T. Nakano, J. Comput. Chem. **30**, 40 (2009).

73. Y. Komeiji, Y. Mochizuki, T. Nakano, and D. G. Fedorov, J. Mol. Str. (THEOCHEM) **898**, 2 (2009).

74. T. Fujita, H. Watanabe, and S. Tanaka, J. Phys. Soc. Jpn. **78**, 104723 (2009).

75. T. Fujiwara, Y. Mochizuki, Y. Komeiji, Y. Okiyama, H. Mori, T. Nakano, and E. Miyoshi, Chem. Phys. Lett. **490**, 41 (2010).

76. T. Fujiwara, H. Mori, Y. Mochizuki, H. Tatewaki, and E. Miyoshi, J. Mol. Str. (THEOCHEM) **949**, 28 (2010).

77. M. Sato, H. Yamataka, Y. Komeiji, Y. Mochizuki, and T. Nakano, Chem. Eur. J. **16**, 6430 (2010).

78. Y. Komeiji, Y. Mochizuki, and T. Nakano, Chem. Phys. Lett. **484**, 380 (2010).

79. K. Kitaura, S. I. Sugiki, T. Nakano, Y. Komeiji, and M. Uebayasi, Chem. Phys. Lett. **336**, 163 (2001).

80. T. Nagata, D. G. Fedorov, and K. Kitaura, Chem. Phys. Lett. **475**, 124 (2009).

81. M. W. Schmidt, K. K. Baldridge, J. A. Boatz, S. T. Elbert, M. S. Gordon, J. J. Jensen, S. Koseki, N. Matsunaga, K. A. Nguyen, S. Su, T. L. Windus, M. Dupuis, and J. A. Montgomery, J. Comput. Chem. **14**, 1347 (1993).

82. M. S. Gordon and M. W. Schmidt, *Theory and Applications of Computational Chemistry, the first forty years*, Elsevier, Amsterdam, 2005.

83. D. G. Fedorov, T. Ishida, M. Uebayasi, and K. Kitaura, J. Phys. Chem. A **111**, 2722 (2007).

84. T. Nagata, D. G. Fedorov, and K. Kitaura, Chem. Phys. Lett. **492**, 302 (2010).

85. H. P. Hratchian, P. V. Parandekar, K. Raghavachari, M. J. Frisch, and T. Vreven, J. Chem. Phys. **128**, 034107 (2008).

86. N. J. Mayhall, K. Raghavachari, and H. P. Hratchian, J. Chem. Phys. **132**, 114107 (2010).

87. W. Xie, L. Song, D. G. Truhlar, and J. Gao, J. Chem. Phys. **128**, 234108 (2008).

88. Y. Yamaguchi, H. F. Schaefer III, Y. Osamura, and J. Goddard, *A New Dimension to Quantum Chemistry: Analytical Derivative Methods in Ab Initio Molecular Electronic Structure Theory*, Oxford University Press, New York, 1994.

89. D. G. Fedorov, R. M. Olson, K. Kitaura, M. S. Gordon, and S. Koseki, J. Comput. Chem. **25**, 872 (2004).

90. Y. Alexeev, M. W. Schmidt, T. L. Windus, and M. S. Gordon, J. Comput. Chem. **28**, 1685 (2007).

91. T. Nagata, D. G. Fedorov, K. Kitaura, and M. S. Gordon, J. Chem. Phys. **131**, 024101 (2009).

92. D. G. Fedorov, K. Kitaura, H. Li, J. H. Jensen, and M. S. Gordon, J. Comput. Chem. **27**, 976 (2006).

93. W. D. Cornell, P. Cieplak, C. I. Bayly, I. R. Gould, K. M. Merz, D. M. Ferguson, D. C. Spellmeyer, T. Fox, J. W. Caldwell, and P. A. Kollman, J. Amer. Chem. Soc. **117**, 5179 (1995).

94. T. Nagata, D. G. Fedorov, T. Sawada, K. Kitaura, and M. S. Gordon, J. Chem. Phys. **134**, 034110 (2011).

95. H. Li, D. G. Fedorov, T. Nagata, K. Kitaura, J. H. Jensen, and M. S. Gordon, J. Comput. Chem. **31**, 778 (2010).

96. C. Steinmann, D. G. Fedorov, and J. H. Jensen, J. Phys. Chem. A **114**, 8705 (2010).

97. K. Sakata, J. Phys. Chem. A **104**, 10001 (2000).

Figure 1. Schematic diagram of the self-consistent Z-vector (SCZV) procedure.

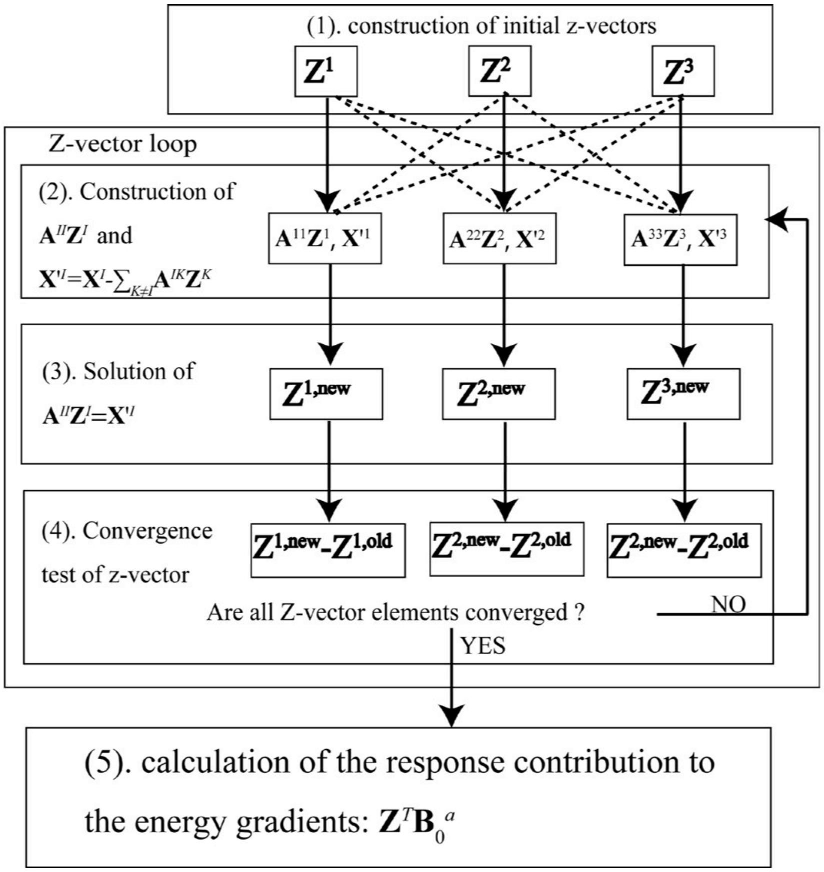

Figure 1

Figure 2a. Geometric structures of $(H_2O)_{64}$, (colored by chemical elements as light grey (H), dark grey (C), blue (N), and red (O)).

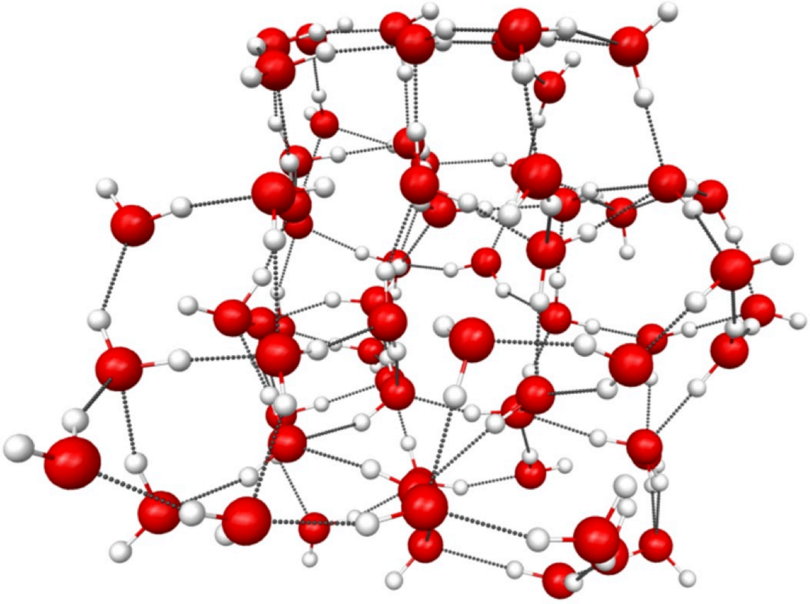

Figure 2a

Figure 2b. Geometric structures of $(ALA)_{10}$ capped with CH_3CO- and -$NHCH_3$ groups, (colored by chemical elements as light grey (H), dark grey (C), blue (N), and red (O)).

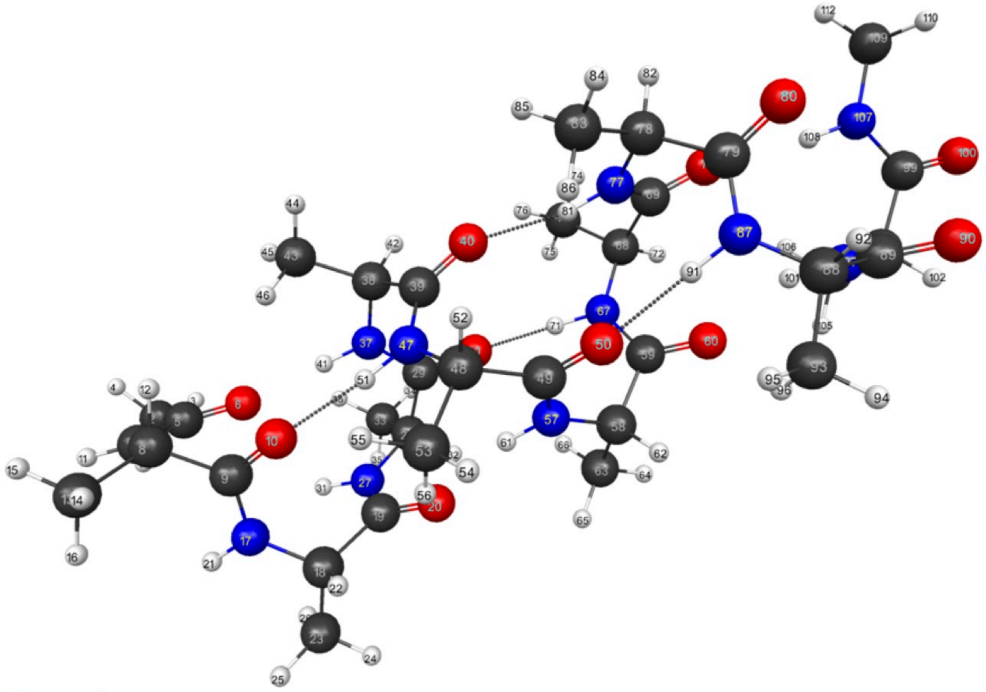

Figure 2b

Figure 2c. Geometric structures of chignolin solvated by 157 water molecules (colored by chemical elements as light grey (H), dark grey (C), blue (N), and red (O)).

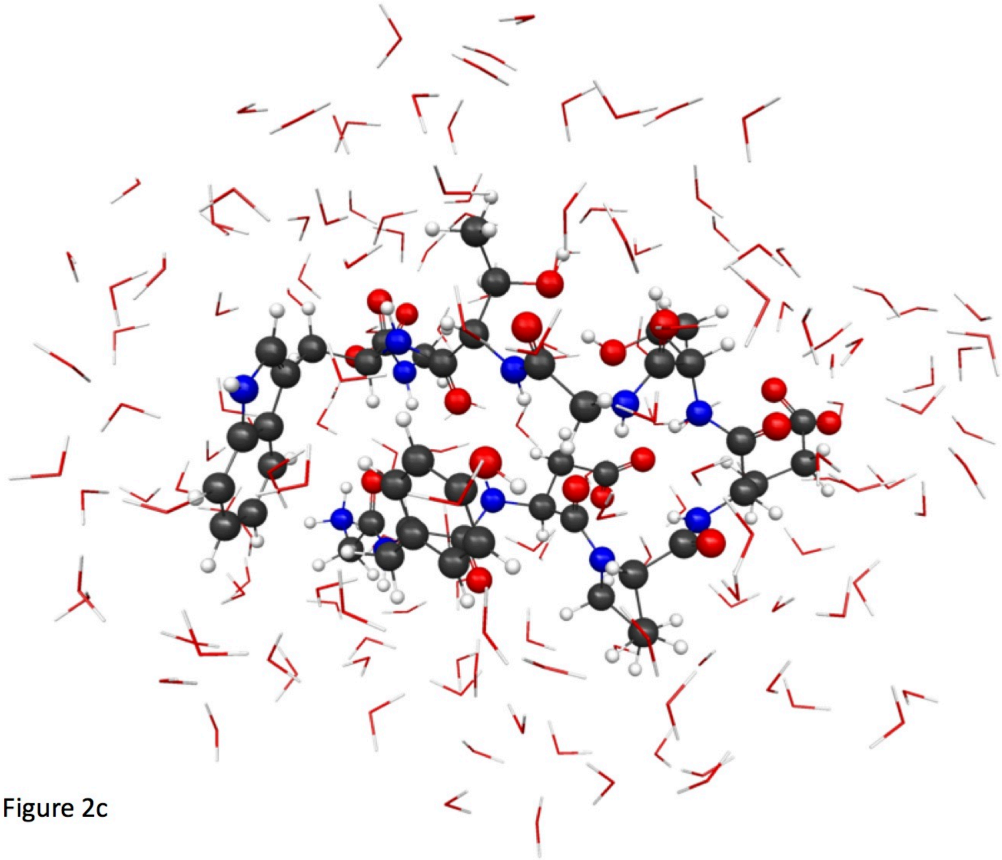

Figure 2c

Figure 2d. Geometric structures of 1L2Y (colored by chemical elements as light grey (H), dark grey (C), blue (N), and red (O)).

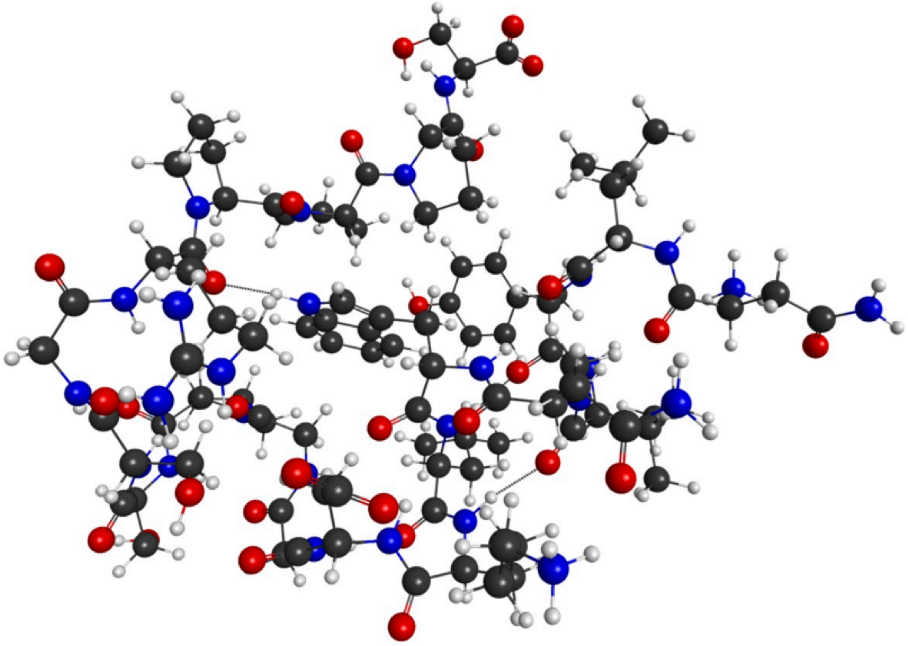

Figure 2d

Figure 3a. Errors of the analytic gradient elements relative to the numeric gradient elements for $(H_2O)_{64}$. Black diamond: fully analytic energy gradients calculated at the RHF/6-31G(d) level. Yellow square: the conventional gradients.

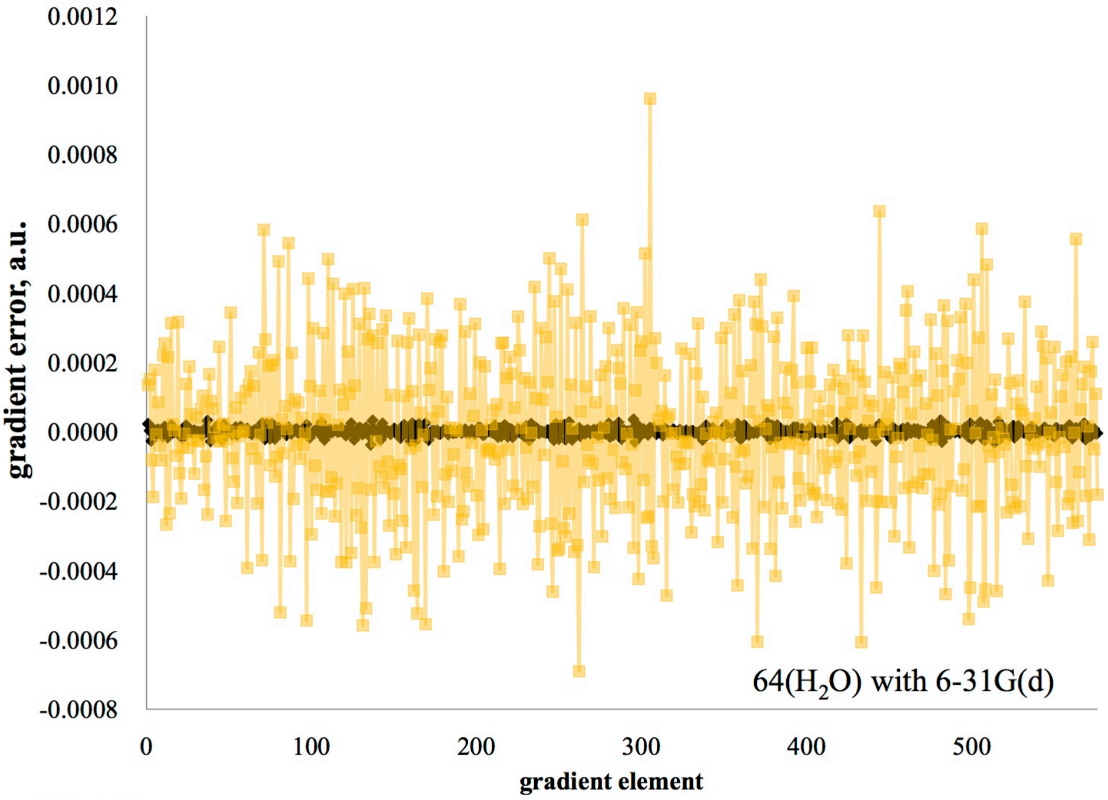

Figure 3a

Figure 3b. Errors of the analytic gradient elements relative to the numeric gradient elements for $(ALA)_{10}$ capped with CH_3O- and -$NHCH_3$ groups calculated at the RHF/6-31G(d) level. Black diamond: fully analytic energy gradients. Yellow square: the conventional gradients.

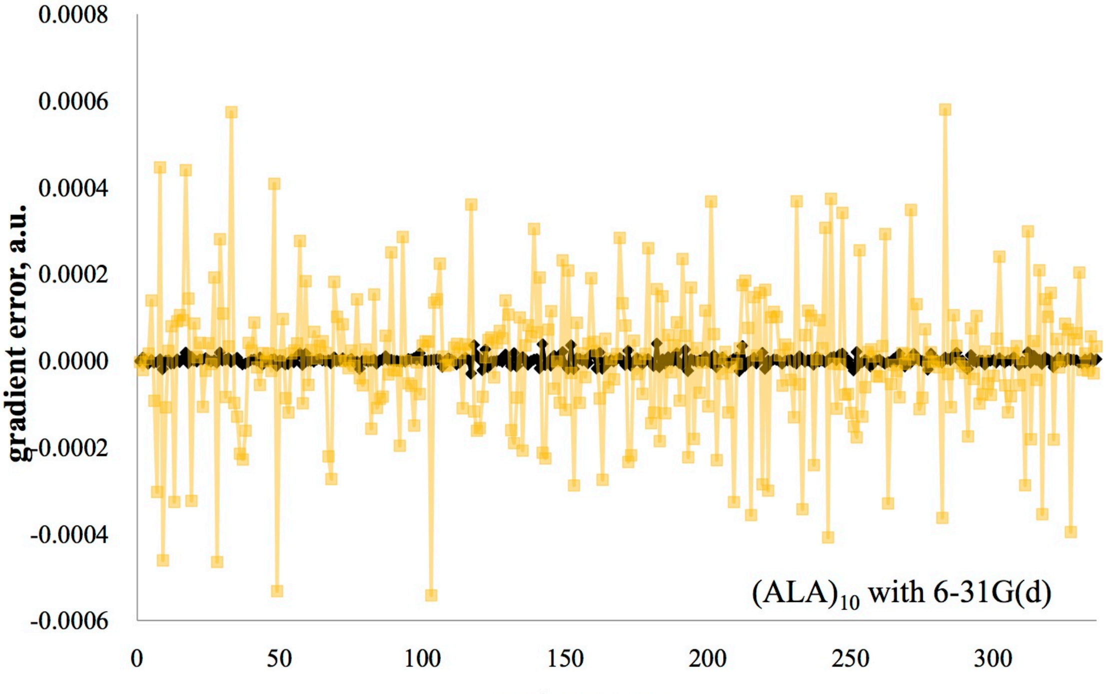

Figure 3b

Figure 3c. Errors of the analytic gradient elements relative to the numeric gradient elements for chignolin solvated by 157 water molecules calculated at the RHF/6-31G(d) level. Black diamond: fully analytic energy gradients. Yellow square: the conventional gradients.

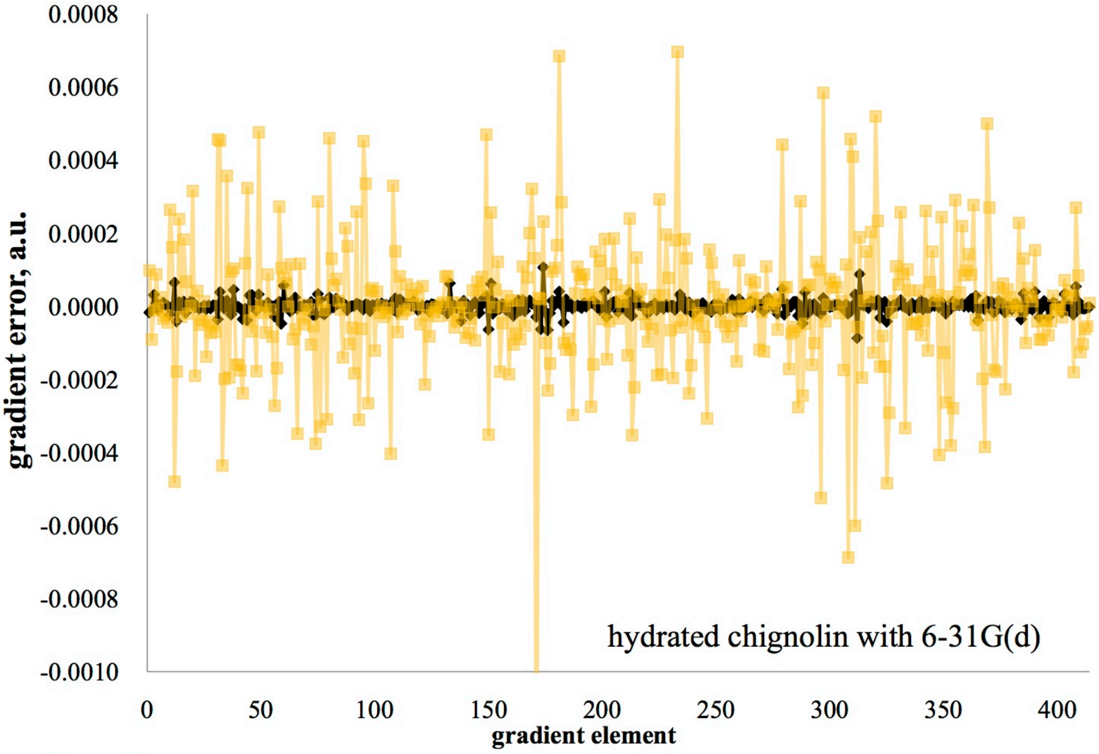

Figure 3c

Figure 3d. Errors of the analytic gradient elements relative to the numeric gradient elements for 1L2Y calculated at the RHF/6-31G(d) level. Black diamond: fully analytic energy gradients. Yellow square: the conventional gradients.

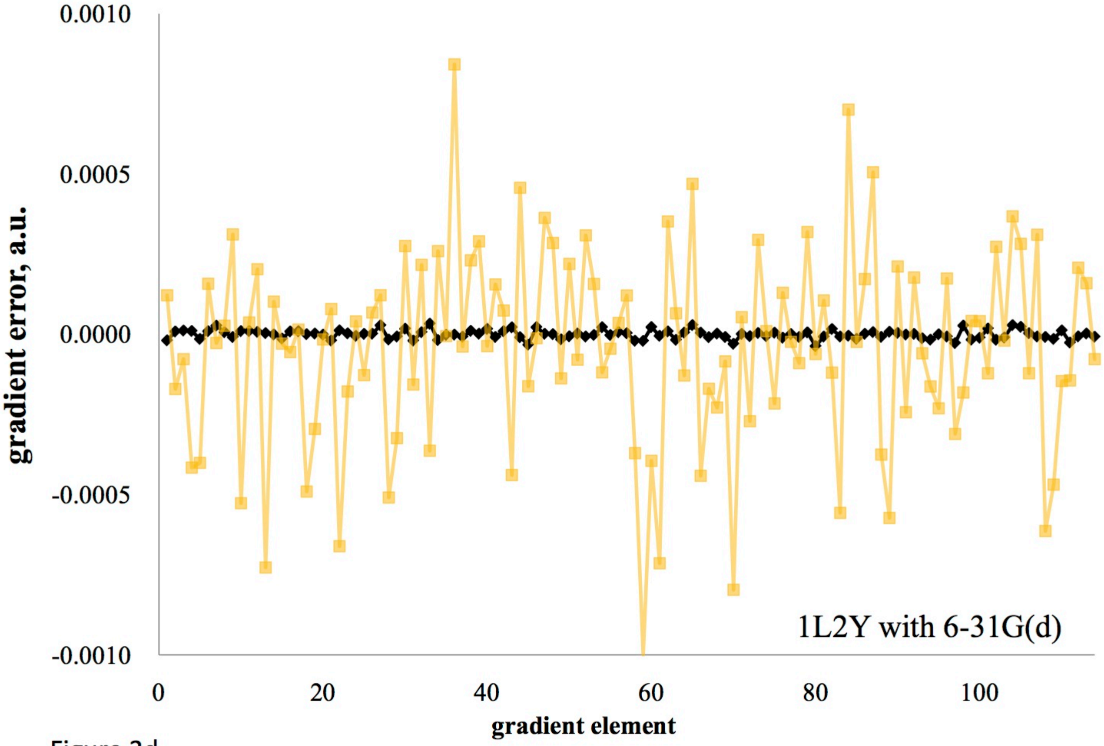

Figure 3d

Figure 3e. Errors of the analytic gradient elements relative to the numeric gradient elements for $(H_2O)_{64}$ at the RHF/6-311G(d). Black diamond: fully analytic energy gradients. Yellow square: the conventional gradients.

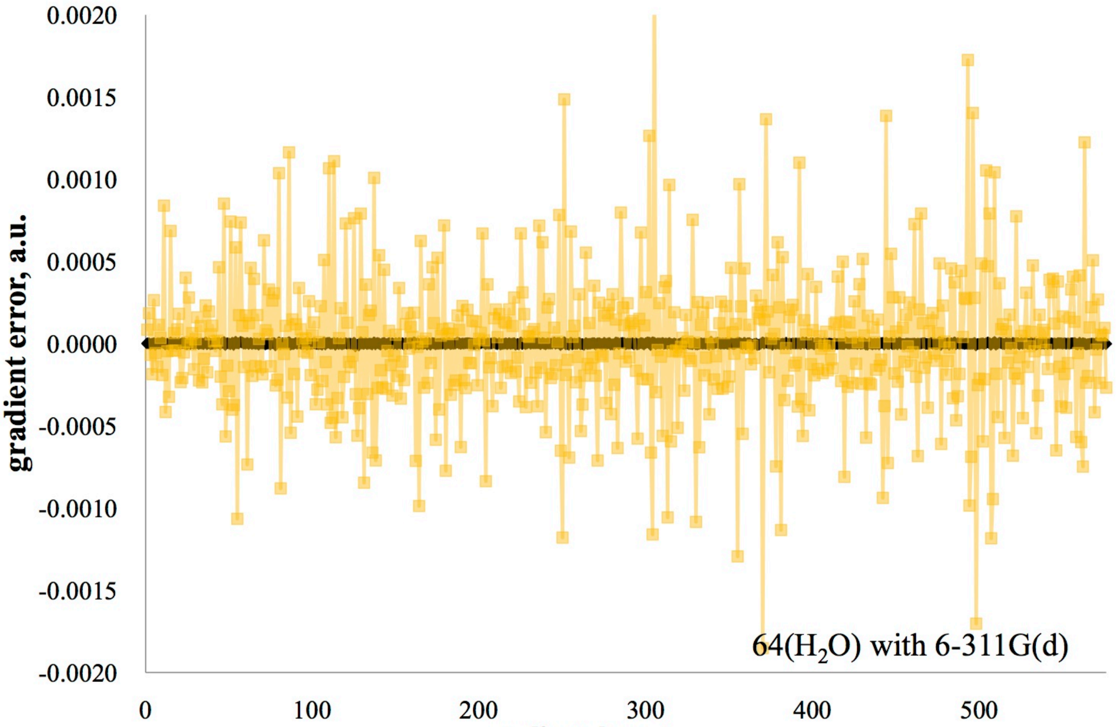

Figure 3e

Figure 4. The parallel efficiency using the PC cluster of 1, 2, 4, 8, 16 and 32 CPUs (Intel Pentium 4 3.2 GHz). Solid line: for the total gradient calculation. Dashed line: for the SCZV calculation.

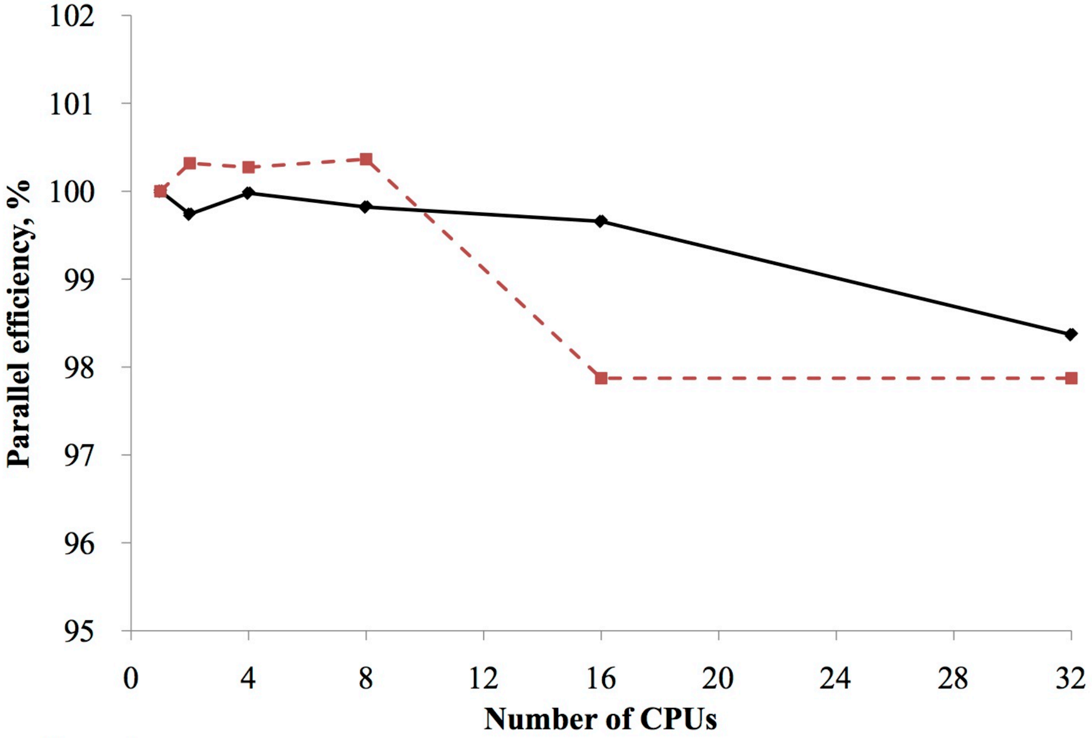

Figure 4

Table I. The number of GDDI groups used in dividing 31 nodes

	monomer step	dimer step
$(H_2O)_{64}$	16	16
$(ALA)_{10}$	5	15
hydrated chignolin	5	15
1L2Y	10	15

Table II. The root mean square (RMS) and the maximum absolute values (MAX grad.) of the gradient elements for FMO2-RHF. RMS of the errors of the analytic gradients relative to the numeric gradients (RMS error) and the error in the maximum absolute gradient values (MAX error). All values are in a.u.

gradient	RMS	MAX grad.	RMS error	MAX error
$(H_2O)_{64}$ without approximations, 6-31G(d)				
numeric	0.005997	0.014090	-	-
analytic	0.005997	0.014094	0.000011	0.000035
conventional	0.006132	0.014347	0.000231	0.000961
$(H_2O)_{64}$ with $L_{\text{ES-DIM}}$=2.0, 6-31G(d)				
numeric	0.005997	0.014090	-	-
analytic	0.005997	0.014094	0.000011	0.000034
conventional	0.006132	0.014347	0.000232	0.000975
$(H_2O)_{64}$ with $L_{\text{ES-DIM}}$=2.0, 6-311G(d)				
numeric	0.007467	0.018020	-	-
analytic	0.007469	0.018029	0.000003	0.000010
conventional	0.007745	0.018507	0.000433	0.002280
$(ALA)_{10}$ without approximations, 6-31G(d)				
numeric	0.011658	0.043197	-	-
analytic	0.011664	0.043222	0.000009	0.000039
conventional	0.011655	0.043169	0.000160	0.000580
Hydrated (EFP) chignolin without approximations, 6-31G(d)				
numeric	0.000284	0.002010	-	
fully analytic	0.000280	0.001995	0.000017	0.000092
conventional	0.000215	0.001542	0.000191	0.001501
1L2Y with $L_{\text{ES-DIM}}$=2.0, 6-31G(d)				
numeric	0.019779	0.047540	-	-
analytic	0.019780	0.047543	0.000015	0.000037
conventional	0.019822	0.047418	0.000335	0.001001

Table III. Wall-clock time in the SCC, SCZV and the total computation using a 31 single 3.2 GHz Pentium 4 cluster (all in seconds), FMO2-RHF/6-31G(d).

	SCC	SCZV	TOTAL
$(H_2O)_{64}$ without approximations			
analytic	24.3	29.5	467.2
conventional	23.0	-	431.4
$(H_2O)_{64}$ with $L_{\text{ES−DIM}}$=2.0			
analytic	29.4	28.1	261.0
conventional	24.3	-	227.8
$(ALA)_{10}$ without approximations			
analytic	359.7	230.4	1240.3
conventional	358.4	-	1016.3
hydrated chignolin without approximations			
analytic	1383.6	883.2	7299.8
conventional	1382.4	-	6419.2
1L2Y with $L_{\text{ES−DIM}}$=2.0			
analytic	3429.1	2320.7	12942.1
conventional	3380.4	-	10597.1

Chapter 3. Analytic gradient for fragment molecular orbital density functional theory

A paper to be submitted to *The Journal of Chemical Theory and Computation*

Kurt R. Brorsen, Federico Zahariev, Hiroya Nakata, Mark S. Gordon

Abstract

The equations for the response terms for the fragment molecular orbital (FMO) method interfaced with the denisty functional theory (DFT) gradient are derived and implemented. Compared to the previous FMO-DFT gradient that lacks response terms, the FMO-DFT analytic gradient has improved accuracy for a variety of functionals when compared to numerical gradients. The FMO-DFT gradient agrees with the fully *ab initio* DFT gradient in which no fragmentation is performed, while reducing the non-linear scaling associated with standard DFT. Solving for the response terms requires the solution of the coupled perturbed Kohn-Sham equations (CPKS) where the CPKS equations are solved through a decoupled Z-vector procedure called the self-consistent Z-vector method. FMO-DFT is a non-variational method and the FMO-DFT gradient is unique compared to standard DFT gradients in that the FMO-DFT gradient requires terms from both DFT and time-dependent DFT theories.

1. Introduction

The fragment molecular orbital (FMO) method[1] is one of many techniques[2-7] that seek to reduce the non-linear scaling of standard quantum chemical methods by fragmentation. FMO has been applied to many biological[8-10] and inorganic systems[11,12].

As electron correlation plays an important role in many systems of chemical interest, the FMO method was interfaced with density functional theory (DFT), including an energy gradient, in 2003.[13] In the FMO prescription, the individual fragments (monomers) are iterated to self-consistency.[14] However, if pairs of fragments (dimers) are included explicitly (as in the FMO2 level of theory), the dimers are not iterated to self-consistency. Because the dimer calculations are not iterated to self-consistency, it is necessary, even for first order derivatives, to include response terms that arise from the derivatives of the molecular orbital coefficients with respect to the nuclear coordinates.[15,16] Similar to other FMO gradient implementations at the time,[15-18] response terms for the FMO-DFT gradient were not included due to the complexity of solving for the response terms. The authors assumed that the contribution of the response terms to the gradient would be small and therefore could be ignored in most circumstances. However, the inclusion of response terms improves the efficiency of geometry optimizations, while for FMO molecular dynamics simulatons,[19-21] the neglect of the response terms in the energy gradient results in poor energy conservation in the microcanonical ensemble.[19] Additionally, the error in the analytic gradient prevents the implementation of semi-analytic hessians (i.e., finite differences of analytic gradients). The lack of semi-analytic hessians means that the FMO method must use fully numerical hessians. Fully numerical Hessians can be computationally intense and are prone to error, thereby limiting the applicability of FMO for finding transition states and the verification of potential energy minima.

Because of the shortcomings in the original FMO gradient, the analytic FMO restricted Hartree-Fock (RHF) gradient, including response terms, was derived and implemented.[16] The response terms were included through the self-consisted Z-Vector (SCZV) method. The Z-Vector[22-24] is calculated in the Z-vector "field" of the other fragments. Since the derivation of the FMO-RHF response terms, further improvements to the FMO gradient have followed, including extensions to unrestricted Hartree-Fock (UHF),[25] 2nd order Moller-Plesset perturbation theory (MP2), [26] and the electrostatic point charge (ESP-PC) approximation.[27,28] The analytic energy gradient has also been interfaced with the polarizable continuum model (PCM),[29] and the effective fragment potential (EFP).[30] Additionally, FMO analytic hessians have been implemented for both RHF and unrestricted HF (UHF).[31]

It has been demonstrated that the improved FMO-RHF gradient eliminates the lack of energy conservation for FMO-MD simulations.[21] In the present work, the derivation of the fully analytic FMO-DFT method is presented and the implementation of the method is discussed.

As the Kohn-Sham and coupled perturbed Kohn-Sham (CPKS) equations[32] are similar to the Hartree-Fock and coupled perturbed Hartree-Fock equations, the derivation and implementation presented in the present study closely follows that of the FMO-RHF analytic gradient.[16]

While the FMO-DFT derivation presented below is similar to that of FMO-RHF, the derivation is unique when compared to other DFT gradients. Because the FMO2-DFT method is not variational, first order derivatives require higher order functional derivatives than do standard DFT gradients. The higher order functional derivatives normally arise in time-dependent DFT (TDDFT) calculations and therefore the FMO-DFT gradient employs both DFT and TDDFT theory.

2. Analytic gradient for FMO-DFT

The FMO2-DFT energy expansion is

$$E=\sum_{I}^{N} E'_I + \sum_{I>J}^{N} (E'_{IJ} - E'_I - E'_J) + \sum_{I>J}^{N} Tr(\Delta\mathbf{D}^{IJ}\mathbf{V}^{IJ}), \tag{1}$$

E'_X is the internal fragment energy of monomer or dimer X, $\mathbf{V}^{IJ}$ is the matrix of the electrostatic potential for dimer IJ, and $\Delta\mathbf{D}^{IJ}$ is the dimer density difference matrix,

$$\Delta\mathbf{D}^{IJ} = \mathbf{D}^{IJ} - (\mathbf{D}^{I} \oplus \mathbf{D}^{J}). \tag{2}$$

In Eq. (2), $\mathbf{D}^{\mathbf{X}}$ is the density of fragment X. The internal fragment energy is defined as

$$E'_X = \sum_{\mu\nu\in X} D^X_{\mu\nu} h^X_{\mu\nu} + \frac{1}{2} \sum_{\mu\nu\lambda\sigma\in X} \left[D^X_{\mu\nu} D^X_{\lambda\sigma} - \frac{c_x}{2} D^X_{\mu\lambda} D^X_{\nu\sigma} \right] (\mu\nu\,|\,\lambda\sigma) + \mathrm{E}^X_{XC} + \mathrm{E}^X_{NR}, \tag{3}$$

$h^X_{\mu\nu}$ is the one-electron Hamiltonian of monomer or dimer X, c_x is the scaling factor for hybrid functionals, and $(\mu\nu\,|\,\lambda\sigma)$ is a two electron integral in the atomic orbital basis. The nuclear repulsion energy E^X_{NR} is defined as

$$\mathrm{E}^X_{NR} = \sum_{\mathrm{B}\in X} \sum_{\mathrm{A}(\in X)>\mathrm{B}} \frac{\mathrm{Z_A Z_B}}{R_{\mathrm{AB}}}, \tag{4}$$

$\mathrm{Z_A}$ is the nuclear charge of atom A, and R_{AB} is the distance between atoms A and B. E^X_{XC} is the exchange-correlation energy. The exchange-correlation energy $\mathrm{E}^X_{xc}\left[\rho^X\right]$ is a functional of the density of fragment X,

$$\rho^X(\vec{r}) = \sum_{\mu,\nu\in X} D^X_{\mu\nu} \phi^X_\mu(\vec{r}) \phi^X_\nu(\vec{r}), \tag{5}$$

where $\phi^X_\mu(\vec{r})$ are atomic orbitals in fragment X.

If fragmentation occurs across a covalent bond, the hybrid orbital projection (HOP) contribution[33]

$$\sum_{i\in X}^{occ} 2\langle i|\hat{P}^X|i\rangle = \sum_{\mu\nu\in X} D^X_{\mu\nu}P^X_{\mu\nu}, \tag{6}$$

must be added to E'_X; $\hat{P}^X$ is the hybrid projection operator

$$\hat{P}^X = \sum_{k\in X} \mathrm{B}_\kappa |\theta_K\rangle\langle\theta_K|, \tag{7}$$

$|\theta_K\rangle$ is the hybrid orbital and B_κ is a constant.

The matrix in Eq. (1) is formed from one and two-electron contributions:

$$V^{IJ}_{\mu\nu} = \sum_{K\neq IJ} \left(u^K_{\mu\nu} + v^K_{\mu\nu}\right). \tag{8}$$

The one-electron and two-electron parts are defined in Eqs. (9) and (10), respectively.

$$u^K_{\mu\nu} = \sum_{\mathrm{A}\in\mathrm{K}} \langle\mu|\frac{-\mathrm{Z}_\mathrm{A}}{|r-R_\mathrm{A}|}|\nu\rangle, \tag{9}$$

$$v^K_{\mu\nu} = \sum_{\lambda\sigma\notin\mathrm{K}} D^\mathrm{K}_{\lambda\sigma}(\mu\nu|\lambda\sigma). \tag{10}$$

Calculation of the two-electron terms is expensive, so in most FMO calculations, a cutoff value is specified such that for monomers separated by a distance greater than the cutoff value, the two-electron term in the electrostatic potential (ESP) is approximated using point charges (PC) as

$$v^K_{\mu\nu} = \tilde{v}^K_{\mu\nu} = \sum_{\mathrm{A}\in\mathrm{K}} \langle\mu|\frac{-Q_\mathrm{A}}{|r-R_\mathrm{A}|}|\nu\rangle. \tag{11}$$

The approximation is called the ESP-PC approximation[34] and is used in most FMO calculations.

The differentiation of the total FMO-DFT energy contains two components. One component contains terms from the internal fragment energies, E'_X ; the second component contains terms from the ESP. The derivative of the internal fragment energy, E'_X , with respect to nuclear coordinate a is

$$\frac{\partial E'_X}{\partial a} = \sum_{\mu\nu\in X} D^X_{\mu\nu}\frac{\partial h^X_{\mu\nu}}{\partial a} + \frac{1}{2}\sum_{\mu\nu\lambda\sigma\in X}\left[D^X_{\mu\nu}D^X_{\sigma\lambda} - \frac{c_x}{2}D^X_{\mu\lambda}D^X_{\nu\sigma}\right]\frac{\partial(\mu\nu|\lambda\sigma)}{\partial a} + D^X_{\mu\nu}\int v^X_{xc}\left[\rho^X\right](\vec{r})\frac{\partial\left(\phi^X_\mu(\vec{r})\phi^X_\nu(\vec{r})\right)}{\partial a}d\vec{r} +$$

$$\sum_{\mu\nu\in X} D^X_{\mu\nu}\frac{\partial P^X_{\mu\nu}}{\partial a} - 2\sum_{i,j\in X}^{occ} S^{a,X}_{ji}F'^X_{ji} - 4\sum_{i\in X}^{occ}\sum_{r\in X}^{vir} U^{a,X}_{ri}V^X_{ri} + \frac{\partial \mathrm{E}^X_{NR}}{\partial a} + W^X_{XC}. \tag{12}$$

The superscript a on S and U refer to a derivative with respect to coordinate a. The derivative of $\mathrm{E}^X_{xc}\left[\rho^X\right]$ with respect to the nuclear coordinate a is found by using Eq. (5) and the functional form of the chain rule.

$v^X_{xc}\left[\rho^X\right](\vec{r})$ is the exchange-correlation potential, $\dfrac{\delta E^X_{xc}\left[\rho^X\right]}{\delta\rho^X(\vec{r})}$, which is a functional of the density. Most exchange-correlation functionals are computed on a grid. In Eq.(12), W^X_{XC} arises from the derivative of the grid weights of $\mathrm{E}^X_{xc}\left[\rho^X\right]$.[35] The reader is referred to Ref. 35 for more details about the derivative of grid weights. The internal fragment Fock matrix element is

$$F'^X_{ij} = h^X_{ij} + \sum_{k\in X}^{occ}\left[2(ij|kk) - c_x(ik|jk)\right] + \left(i\middle|v^X_{xc}\middle|j\right) + P^X_{ij}, \tag{13}$$

$\left(i\middle|v^X_{xc}\middle|j\right)$ is a matrix element of the exchange-correlation potential:

$$\left(i\middle|v_{xc}^{X}\middle|j\right) = \sum_{\mu,\nu\in X} C_{\mu i}^{X*}C_{\nu j}^{X}\int\phi_{\mu}^{X*}(\vec{r})v_{xc}^{X}(\vec{r})\phi_{\nu}^{X}(\vec{r})d\vec{r}, \tag{14}$$

P_{ij}^{X} is a matrix element of the HOP matrix

$$P_{ij}^{X} = \sum_{\mu\nu} C_{\mu i}^{X}P_{\mu\nu}^{X}C_{\nu j}^{X}, \tag{15}$$

and the overlap derivative matrix $S_{ij}^{a,X}$ is

$$S_{ij}^{a,X} = \sum_{\mu\nu\in X} C_{\mu i}^{X*}\frac{\partial S_{\mu\nu}^{X}}{\partial\alpha}C_{\nu j}^{X}. \tag{16}$$

The term $S_{ji}^{a,X}F_{ji}'^{X}$ in Eq. (12) arises from the derivatives of the density in Eq. (3) with respect to a nuclear coordinate. The orthonormality condition[22]

$$S_{ij}^{a,X} + U_{ji}^{a,X} + U_{ij}^{a,X} = 0 \tag{17}$$

was used to produce the $S_{ji}^{a,X}F_{ji}'^{X}$ term.

The following definition will be used for the response term $U_{ri}^{a,X}$

$$\overline{U}^{a,X,Y} = 4\sum_{i\in X}^{occ}\sum_{r\in X}^{vir} U_{ri}^{a,X}V_{ri}^{Y}, \tag{18}$$

The response term arises from the derivative of the molecular orbital coefficient

$$\frac{\partial C_{\mu i}^{X}}{\partial a} = \sum_{m\in X}^{occ+vir} U_{ri}^{a,X}C_{\mu m}^{X}. \tag{19}$$

$U_{ri}^{a,X}$ is found by solving the CPKS equations.

The differentiation of the ESP term with respect to nuclear coordinate *a* is

$$\frac{\partial}{\partial a}Tr(\Delta\mathbf{D}^{IJ}\mathbf{V}^{IJ}) = \sum_{\mu\nu\in IJ}\Delta D_{\mu\nu}^{IJ}\sum_{K\neq IJ}^{all}\left[\frac{\partial u_{\mu\nu}^{K}}{\partial a} + \sum_{\mu\nu\in K} D_{\lambda\sigma}^{K}\frac{\partial(\mu\nu|\lambda\sigma)}{\partial a}\right]$$

$$-2\sum_{\mu\nu\in IJ} W_{\mu\nu}^{IJ} \frac{\partial S_{\mu\nu}^{IJ}}{\partial a} + 2\sum_{\mu\nu\in I} W_{\mu\nu}^{I} \frac{\partial S_{\mu\nu}^{I}}{\partial a} + 2\sum_{\mu\nu\in J} W_{\mu\nu}^{J} \frac{\partial S_{\mu\nu}^{J}}{\partial a} + \overline{U}^{a,IJ,IJ} - \overline{U}^{a,I,IJ} - \overline{U}^{a,J,IJ}$$

$$-2\sum_{K\in IJ}^{all} \sum_{\mu\nu\in \mathrm{K}} \Delta X_{\mu\nu}^{\mathrm{K(IJ)}} S_{\mu\nu}^{a,\mathrm{K}} + 4\sum_{\mathrm{K}\neq \mathrm{IJ}}^{all} \sum_{\mu\nu\in IJ} \sum_{r\in K}^{vir} \sum_{i\in K}^{occ} \Delta D_{\mu\nu}^{\mathrm{IJ}} U_{ri}^{a,\mathrm{K}} (\mu\nu \,|\, ri), \tag{20}$$

where

$$W_{\mu\nu}^{X} = \frac{1}{4} \sum_{\mu\nu\in X} D_{\mu\lambda}^{X} V_{\lambda\sigma}^{\mathrm{IJ}} D_{\sigma\nu}^{X}, \tag{21}$$

and

$$\Delta X_{\mu\nu}^{K(IJ)} = \frac{1}{4} \sum_{\lambda\sigma\in \mathrm{K}} D_{\mu\lambda}^{\mathrm{K}} \left[\sum_{\zeta\eta\in IJ} \Delta D_{\zeta\eta}^{IJ} (\zeta\eta \,|\, \lambda\sigma) \right] D_{\sigma\nu}^{\mathrm{K}}. \tag{22}$$

Collecting all of the terms $\overline{U}^{a,X,Y}$ from Eqs. (12) and (20) forms the equation

$$\overline{U}^{a} = -\sum_{I}^{N} \overline{U}^{a,I,I} - \sum_{I>J}^{N} \left(\overline{U}^{a,IJ,IJ} - \overline{U}^{a,I,I} - \overline{U}^{a,J,J} \right) + \sum_{I>J}^{N} \left(\overline{U}^{a,IJ,IJ} - \overline{U}^{a,I,IJ} - \overline{U}^{a,J,IJ} \right). \tag{23}$$

$\overline{U}^{a}$ is equal to zero when either no approximations are applied to the calculation of the ESP or approximations to the calculation of the ESP are applied uniformly. For most FMO calculations, the calculation of the ESP is approximated, but not uniformly and therefore the contribution from $\overline{U}^{a}$ must be included in the gradient. The contribution from $\overline{U}^{a}$ has previously been included for the FMO-RHF method.[27] As $\overline{U}^{a}$ only contains terms involving $U_{ri}^{a,X}$ and V_{ri}^{Y}, the contributions to the gradient from $\overline{U}^{a}$ are identical for the FMO-RHF and FMO-DFT methods and the interested reader is referred to the previous study.[16,27] For the purposes of the derivation in the present study, $\overline{U}^{a}$ will be treated as equal to zero; therefore, the only contributions to the gradient from $U_{ri}^{a,K}$ arise from the last term of Eq. (20). To find the last term of Eq. (20), it is necessary to solve the CPKS equations.

3. Coupled Perturbed Kohn-Sham equations for FMO-DFT

The FMO-DFT analytic gradient only contains response term contributions from monomers. The response term contributions can be found by exploiting the diagonal nature of the Fock matrix to solve the CPKS equations[32] for the FMO-DFT method. For monomer *I*, the MO Fock matrix can be written as

$$F_{ij}^{I}=F_{ij}'^{I}+V_{ij}^{I}$$

$$=\tilde{h}_{ij}^{I}+\sum_{k\in \mathrm{I}}^{occ}\left[2(ij\,|\,kk)-c_x(ik\,|\,jk)\right]+\left(i\middle|v_{xc}^{X}\middle|j\right)+P_{ij}^{\mathrm{I}}, \tag{24}$$

The FMO one-electron Hamiltonian is

$$\tilde{h}_{ij}^{I}=h_{ij}^{I}+V_{ij}^{I}. \tag{25}$$

The derivative of the monomer Fock matrix with respect to a nuclear coordinate is

$$\frac{\partial F_{ij}^{I}}{\partial a}=\frac{\partial}{\partial a}\left(\tilde{h}_{ij}^{I}+\sum_{k\in \mathrm{I}}^{occ}\left[2(ij\,|\,kk)-c_x(ik\,|\,jk)\right]+\left(i\middle|v_{xc}^{X}\middle|j\right)+P_{ij}^{\mathrm{I}}\right). \tag{26}$$

Taking the derivative of the right side and rearranging terms, the derivative of the monomer Fock matrix with respect to nuclear coordinate can be written as

$$\frac{\partial F_{ij}^{I}}{\partial a}=F_{ij}^{a,I}+\sum_{k\in \mathrm{I}}^{occ+vir}\left(U_{ki}^{a,\mathrm{I}}F_{kj}^{\mathrm{I}}+U_{kj}^{a,\mathrm{I}}F_{ik}^{\mathrm{I}}\right)+\sum_{k\in \mathrm{I}}^{occ+vir}\sum_{l\in \mathrm{I}}^{occ}U_{kl}^{a,\mathrm{I}}\mathrm{A}'_{ij,kl}+\sum_{K\neq I}\sum_{k\in \mathrm{K}}^{occ+vir}\sum_{l\in \mathrm{K}}^{occ}U_{kl}^{a,\mathrm{K}}4(ij\,|\,kl),$$

(27)

The orbital Hessian matrix A’ is defined as

$$A'_{ij,kl}=4(ij\,|\,kl)-c_x\left[(ik\,|\,jl)+(il\,|\,jk)\right]+4\left(ij\middle|f_{xc}^{X}\middle|kl\right), \tag{28}$$

$\left(ij\middle|f_{xc}^{X}\middle|kl\right)$ is the matrix element of the exchange-correlation kernel:

$$f_{xc}^{X}\left[\rho^{X}\right](\vec{r},\vec{r}')=\frac{\delta^{2}E_{xc}^{X}\left[\rho^{X}\right]}{\delta\rho^{X}(\vec{r})\,\delta\rho^{X}(\vec{r}')} \tag{29}$$

$$\left(ij\middle|f_{xc}^{X}\middle|kl\right)=\sum_{\mu,\nu,\rho,\sigma\in X}C_{\mu i}^{X*}C_{\nu j}^{X}C_{\rho k}^{X*}C_{\sigma l}^{X}\iint\phi_{\mu}^{X*}(\vec{r})\,\phi_{\nu}^{X}(\vec{r})\,f_{xc}^{X}(\vec{r},\vec{r}')\,\phi_{\rho}^{X*}(\vec{r}')\,\phi_{\sigma}^{X}(\vec{r}')\,d\vec{r}\,d\vec{r}' \tag{30}$$

The derivative of the Fock matrix element is

$$F_{ij}^{a,I}=h_{ij}^{a,I}+V_{ij}^{a,I}+\sum_{k\in\mathrm{I}}^{occ}\left[2(ij\,|\,kk)^{\alpha}-c_{x}(ik\,|\,jk)^{\alpha}\right]+\left(i\middle|v_{xc}^{X}\middle|j\right)^{a}+P_{ij}^{\alpha,\mathrm{I}}. \tag{31}$$

$h_{ij}^{a,I}$ is the derivative of the one-electron Hamiltonian

$$h_{ij}^{a,I}=\sum_{\mu\nu\in I}C_{\mu i}^{\mathrm{I}*}C_{\nu j}^{\mathrm{I}}\frac{\partial h_{\mu\nu}^{\mathrm{I}}}{\partial a}, \tag{32}$$

The derivative of the two-electron integral $(ij\,|\,kl)^{a}$ is

$$(ij\,|\,kl)^{a}=\sum_{\mu\nu\rho\sigma}C_{\mu i}^{\mathrm{I}*}C_{\nu j}^{\mathrm{I}}C_{\rho k}^{\mathrm{I}*}C_{\sigma l}^{\mathrm{I}}\frac{\partial(\mu\nu\,|\,\rho\sigma)}{\partial a}, \tag{33}$$

and the derivative of the exchange-correlation potential matrix elements $\left(i\middle|v_{xc}^{X}\middle|j\right)^{a}$ is

$$\begin{aligned}\left(i\middle|v_{xc}^{X}\middle|j\right)^{a}&=\sum_{\mu,\nu\in X}C_{\mu i}^{X*}C_{\nu j}^{X}\int v_{xc}^{X}(\vec{r})\frac{\partial\left(\phi_{\mu}^{X*}(\vec{r})\,\phi_{\nu}^{X}(\vec{r})\right)}{\partial a}d\vec{r}\\&+2\sum_{\mu,\nu,\rho,\sigma\in X}C_{\mu i}^{X*}C_{\nu j}^{X}C_{\rho k}^{X*}C_{\sigma l}^{X}\iint\phi_{\mu}^{X*}(\vec{r})\,\phi_{\nu}^{X}(\vec{r})\,f_{xc}^{X}(\vec{r},\vec{r}')\frac{\partial\left(\phi_{\rho}^{X*}(\vec{r}')\,\phi_{\sigma}^{X}(\vec{r}')\right)}{\partial a}d\vec{r}\,d\vec{r}'\end{aligned} \tag{34}$$

The functional form of the chain-rule and the relationship

$$\frac{\delta v_{xc}^{X}\left[\rho^{X}\right](\vec{r})}{\delta\rho^{X}(\vec{r}')}=\frac{\delta^{2}E_{xc}^{X}\left[\rho^{X}\right]}{\delta\rho^{X}(\vec{r})\,\delta\rho^{X}(\vec{r}')}=f_{xc}^{X}\left[\rho^{X}\right](\vec{r},\vec{r}') \tag{35}$$

is used to derive $\left(i\middle|v_{xc}^{X}\middle|j\right)^{a}$.

The ESP derivative $V_{ij}^{a,I}$ is defined as

$$V_{ij}^{a,I} = \sum_{K \notin I} \left(u_{ij}^{a,K} + \sum_{k \in \mathrm{K}}^{occ} 2(ij \mid kk)^{\alpha} \right). \tag{36}$$

The one electron derivative contribution, $u_{ij}^{a,K}$, in Eq. (36) and the HOP derivative $P_{ij}^{a,1}$ in Eq. (31) are defined in an analogous manner to the derivative of the one-electron Hamiltonian $h_{ij}^{a,I}$ in Eq. (32).

Further rearrangement of Eq. (26) leads to

$$\begin{aligned}\frac{\partial F_{ij}^{I}}{\partial a} &= F_{ij}^{a,I} - \left(\varepsilon_j^I - \varepsilon_i^I\right) U_{ij}^{a,I} - S_{ij}^{a,I} \varepsilon_j^I - \sum_{k,l \in \mathrm{I}}^{occ} S_{kl}^{a,\mathrm{I}} \left[2(ij \mid kl) - c_x (ik \mid jk) \right] + \sum_{k \in \mathrm{I}}^{vir} \sum_{l \in \mathrm{I}}^{occ} U^{a,I} A'_{ij,kl} \\ &- \sum_{K \neq I} \sum_{k,l \in \mathrm{K}}^{occ} 2 S_{kl}^{a,\mathrm{K}} (ij \mid kl) + \sum_{\mathrm{K} \neq \mathrm{I}} \sum_{k \in \mathrm{K}}^{vir} \sum_{l \in \mathrm{K}}^{occ} U_{kl}^{\alpha,\mathrm{K}} 4(ij \mid kl),\end{aligned} \tag{37}$$

where ε_i^I is the energy of MO *i* of fragment *I*. The orthonormality condition[16] of Eq. (13) was used to produce Eq. (37).

For each fragment *I*, Eq. (37) contains $U_{kl}^{a,X}$ contributions from all fragments in the system. Therefore, the $\partial F_{ij}^{X} / \partial a$ for each fragment must be collected and solved together. The $\partial F_{ij}^{X} / \partial a$ for all fragments can be written in matrix form as

$$\mathbf{A}\mathbf{U}^{a} = \mathbf{B}_0^{a}, \tag{38}$$

The fragment block diagonal part of matrix **A** is

$$A_{ij,kl}^{I,I} = \delta_{ik} \delta_{jl} \left(\varepsilon_j^I - \varepsilon_i^I \right) - \left\{ 4(ij \mid kl) - c_x \left[(ik \mid jl) + (il \mid jk) \right] + 4\left(ij \middle| f_{xc}^{X} \middle| kl \right) \right\}, \tag{39}$$

the fragment off-diagonal part is

$$A_{ij,kl}^{I,K} = -4(ij \mid kl), \tag{40}$$

and the *ij* th element of the vector B_0^a for fragment I is

$$B_{0,ij}^{a,I} = F_{ij}^{a,I} - S_{ij}^{a,I}\varepsilon_j^I - \sum_{kl\in \mathrm{I}}^{occ} S_{kl}^{a,\mathrm{I}}\left[2(ij\,|\,kl)-(ik\,|\,jl)\right] - \sum_{\mathrm{K}\neq \mathrm{I}}\sum_{kl\in \mathrm{K}}^{occ} 2S_{kl}^{a,\mathrm{K}}(ij\,|\,kl). \tag{41}$$

The response terms for the FMO-DFT gradient can be included by applying the SCZV procedure to Eq. (38) in a manner identical to the FMO-RHF gradient. Of course, the definitions of the matrix **A** and vector $\mathbf{B}_0^a$ are different for FMO-DFT. The reader interested in the SCZV procedure for the FMO-DFT method is therefore directed to the previous study of the analytic gradient for the FMO-RHF method.[16]

4. Computational Details

To demonstrate that the inclusion of the response terms makes the FMO-DFT gradient fully analytic, gradient calculations with and without the response terms included were compared to numerical gradients. For comparison purposes, the error in the numerical gradient is set to zero. To test the accuracy of the gradient for systems with and without fragmentation across a covalent bond, two test systems were chosen: a $(H_2O)_{32}$ cluster (Figure 1a) and an alanine $(ALA)_7$ polypeptide chain in an alpha helix configuration (Figure 1b). For both test systems, calculations were performed with multiple density functionals. A distance cutoff of 2.0 was used for the ESP-PTC approximation (RESPPC) and the electrostatic dimer approximation (RESDIM) for all calculations. For the RESPPC and RESDIM cutoffs, the distance between two atoms A and B is defined relative to the van der Waals radii of atoms A and B, $R_{AB}/(R_A+R_B)$, where R_{AB} is the Euclidean distance between atoms A and B and R_A is the van der Waals radius of atom A. The numerical energy gradient was calculated using double differencing with a step size of 0.0001 Å and 0.0005 Å for the $(H_2O)_{32}$ cluster and the $(ALA)_7$ polypeptide chain respectively.

For the 32-water cluster, an additional calculation was performed without the ESP-PTC approximation or the electrostatic dimer approximation (a cutoff of 0.0) to quantify how much error is introduced into the gradient calculation through the use of the two approximations. For the water cluster, each water molecule was treated as a fragment, while for the alanine polypeptide chain, each alanine unit was treated as a fragment.

Additional DFT calculations in which no fragmentation was used were performed on the water cluster systems to check the accuracy of the FMO-DFT gradient relative to fully *ab initio* methods. For the additional calculations, the B3LYP, PBE0 and SVWN functionals were used. All the DFT calculations were performed using the 6-31G(d) basis.

All FMO-DFT and DFT calculations in this study used a grid to evaluate the exchange-correlation functional. The grid contained 96 radial points for the Euler-MacLaurin quadrature and 302 angular points for the Lebedev grid.

5. Results and Discussion

Results from the gradient calculations for the water test system are presented in Table 1. For all functionals, inclusion of the response terms results in a more accurate gradient. For the water system, the error in each gradient element with and without response terms is presented in Figure 2 for calculations using the B3LYP functional and Figure 3 for calculations using all non-B3LYP functionals, and Hartree-Fock. For the four water cluster systems for which calculations were performed with the 6-31G(d) basis and the ESP-PTC and electrostatic dimer approximations, the root mean square (RMS) error improves with the inclusion of response terms by a minimum factor of 13 to a maximum factor of 26.

There is a negligible increase in the gradient error when the ESP-PTC and electrostatic dimer approximations are used for the B3LYP water cluster. Specifically, the RMS error increases from 0.000017 Hartree/Bohr to 0.000023 Hartree/Bohr when the approximations are included in the calculation. Although the negligible increase in error indicates that the ESP-PTC and electrostatic dimer approximations can reliably be applied in FMO-DFT gradient calculations, care must be taken when using the ESP-PTC approximation. A previous study[27] using the FMO-RHF method has determined that the vdw radius cutoff for the ESP-PTC approximation should be set above 1.5 for accurate calculations. To assess the effect of the basis set, a test calculation was performed with the 6-311G(2d,2p) basis for the water cluster system with the B3LYP functional. Inclusion of the response terms reduces the RMS error for the system by more than a factor of 18. The factor is similar in magnitude to that obtained from calculations that use the 6-31G(d) basis set, indicating that the inclusion of the response terms gives an accurate gradient for any basis set.

An additional calculation was performed on the water cluster using the FMO-RHF method (Figure 3d) to compare the accuracy of the FMO-DFT gradient to the FMO-RHF gradient. For the FMO-RHF gradient, the inclusion of the response terms reduces the RMS error by a factor of 23. The reduction in the RMS error for the FMO-RHF gradient is similar in magnitude to the reduction in the RMS error for the FMO-DFT gradient when response terms are included, and indicates that the analytic gradient for FMO-DFT is as accurate as that for the FMO-RHF method.

Results from the gradient calculation on the alanine peptide system are presented in Table 2. Like the water system, inclusion of the response terms results in a more accurate gradient for all test systems. For the alanine peptide system, the errors in each gradient element with and without the response terms included are presented in Figure 4. The RMS error improves by a factor of 34 for the B3LYP functional and 36 for PBE0 functional. A previous study[5] found that the FMO-RHF gradient is accurate for a system of bonded fragments. Therefore, a calculation at the FMO-RHF/6-31G(d) level of theory was performed on the alanine peptide system. Inclusion of the response terms for the alanine peptide system at the FMO-RHF/6-31G(d) level of theory improves the RMS error by a factor of 29. Since the decrease in the RMS error for the FMO-RHF gradient is of the same order of magnitude as that for the FMO-DFT gradient, the FMO-DFT gradient is as accurate as the FMO-RHF gradient for systems with either bonded or non-bonded fragments.

Comparison of the FMO-DFT gradient with the DFT gradient with no fragmentation of the system is presented in Table 3. For all three functionals, the FMO-DFT gradient reproduces the DFT gradient. Of the three test functionals, the maximum RMS deviation of the FMO-DFT gradient from the DFT gradient is .0016 Hartree/Bohr with the SVWN functional. For the three test functionals, the largest difference in any single gradient element is 0.00554 Hartree/Bohr and occurs when the B3LYP functional is used.

6. Conclusions

For *ab initio* methods, accurate gradients are a necessity for the calculation of properties, verification of potential energy minimum and molecular dynamics simulations. In the present study, the analytic gradient has been derived and the implementation has been discussed for the FMO2-DFT method using the SCZV procedure previously derived for the FMO-RHF gradient. Inclusion of the response terms results in a more accurate gradient when compared to numerical gradients for all test systems. Given the increased accuracy, the response terms should be included for all FMO-DFT MD calculations. The FMO-DFT gradient reproduces the DFT gradient in which no fragmentation has been performed and is a potential linearly scaling DFT method that can be combined with molecular dynamics. Response terms are now included in the FMO gradient for RHF, UHF, MP2, and DFT, and a future promising research direction will be to extend the analytic gradient to other FMO methods, such as multilayer FMO,[36] three body FMO,[37] FMO with an auxiliary basis set,[38] and the effective fragment molecular orbital method.[39]

7. Acknowledgements

KRB was supported by a Department of Energy Computational Science Graduate Fellowship. FZ and MSG were supported by funds provided by the Department of Energy, Basic Energy Sciences, to the Ames Laboratory, Administered by Iowa State University. The computations reported here were performed on Cyence at Iowa State University.

References

1. K. Kitaura, E. Ikeo, T. Asada, T. Nakano, M. Uebayasi, Chem. Phys. Lett. 313 (3,4) (1999) 701.

2. M. S. Gordon, D. G. Fedorov, S. R. Pruitt, L. V. Slipchenko, Chem. Rev. 112 (2012) 632.

3. P. Otto, J. Ladik, Chem. Phys. 8 (1975) 192–200.

4. W. Yang, Phys. Rev. Lett. 66 (1991) 1438–1441.

5. J. L. Gao, J. Phys. Chem. B 101 (1997) 657–663.

6. M. Kobayashi, H. Nakai, Phys. Chem. Chem. Phys. 14 (2012) 7629-7639

7. Y. Aoki, F. L. Gu, Phys. Chem. Chem. Phys. 14 (2012) 7640-7668.

8. T. Sawada, D. G. Fedorov, K. Kitaura, J. Am. Chem. Soc. 132 (2010) 16862–16872.

9. Y. Alexeev, M. P. Mazanetz, O. Ichihara, D. G. Fedorov, Curr. Top. Med. Chem. 12 (2012) 2013–2033.

10. T. Watanabe, Y. Inadomi, K. Fukuzawa, T. Nakano, S. Tanaka, L. Nils- son, U. Nagashima, J. Phys. Chem. B 111 (2007) 9621–9627.

11. P. J. Carlson, S. Bose, D. W. Armstrong, T. Hawkins, M. S. Gordon, J. W. Petrich, J. Phys. Chem. B 116 (2012) 503–512.

12. P. V. Avramov, D. G. Fedorov, P. B. Sorokin, S. Sakai, S. Entani, M. Ohtomo, H. N. Y. Matsumoto, J. Phys. Chem. Lett. 3 (2012) 2003–2008.

13. S. Sugiki, , N. Kurita, Y. Sengoku, H. Sekino. Chem. Phys. Lett. 382 (2003) 611.

14. D. G. Fedorov, K. Kitaura, The Fragment Molecular Orbital Method: Practical Applications to Large Molecular Systems, CRC press, Boca Raton, FL, 2009.

15. K. Kitaura, S. I. Sugiki, T. Nakano, Y. Komeiji, M. Uebayasi, Chem. Phys. Lett. 336 (2001) 163.

16. T. Nagata, K. Brorsen, D. G. Fedorov, K. Kitaura, M. S. Gordon, J. Chem. Phys. 134 (2011) 124115.

17. T. Nagata, D. G. Fedorov, K. Kitaura, Chem. Phys. Lett. 475 (2009) 124.

18. T. Nagata, D. G. Fedorov, K. Kitaura, Chem. Phys. Lett. 492 (2010) 302.

19. Y. Komeiji et al., Chem. Phys. Lett. 372 (2003) 342.

20. Y. Komeiji, Y. Inadomi, T. Nakano, Comput. Biol. Chem. 28 (2004) 155.

21. K. R. Brorsen, N. Minezawa, F. Xu, T. L. Windus, and M. S. Gordon. J. Chem. Theo. Comp. 8 (2012) 5008.

22. Y. Yamaguchi, H. F. Schaefer III, Y. Osamura, and J. Goddard, A New Dimension to Quantum Chemistry: Analytical Derivative Methods in Ab Initio Molecular Electronic Structure Theory. Oxford University Press, New York, (1994).

23. N. C. Handy, H. F. Schaefer III J. Chem. Phys. 81 (1984) 5031.

24. C. Ochsenfeld, M. S. Gordon, Chem. Phts. Lett. 270 (1997) 399.

25. H. Nakata, D. G. Fedorov, T. Nagata, S. Yokojima, K. Ogata, K. Kitaura, S. Nakamura. J. Chem. Phys. 137 (2012) 044110.

26. T. Nagata, D. G. Fedorov, K. Ishimura, and K. Kitaura, J. Chem. Phys. 135 (2011) 044110.

27. T. Nagata, D. G. Fedorov, K. Kitaura, Chem. Phys. Lett. 544 (2012), 87.

28. H. Nakata, D. G. Fedorov, S. Yokojima, K. Kitaura, S. Nakamura. Theor. Chem. Acc 133 (2014) 1477.

29. T. Nagata, D. G. Fedorov, H. Li, K. Kitaura, J. Chem. Phys. 136 (2012) 204112.

30. T. Nagata, D. G. Fedorov, K. Kitaura, Theor. Chem. Acc 131 (2012) 1136.

31. H. Nakata, T. Nagata, D. G. Fedorov, S. Yokojima, K. Kitaura, and S. Nakamura. J. Chem. Phys. 138 (2013) 164103.

32. F. Furche, R. Ahlrichs, J. Chem. Phys. 117 (2002) 7433.

33. T. Nagata, D. G. Fedorov, K. Kitaura, 492 (2010) 302-308.

34. T. Nakano, T. Kaminuma, T. Sato, K. Fukuzawa, Y. Akiyama, M. Uebayasi, K. Kitaura. Chem. Phys. Lett. 351 (2002) 475.

35. B.G. Johnson, P. M. W. Gill, and J. A. Pople, J. Chem. Phys. 98 (1993) 5612.

36. D. G. Fedorov, T. Ishida, K. Kitaura. J. Phys. Chem. *A* 109, 11 (2005) 2638.

37. D. G. Fedorov, K. Kitaura, J. Chem. Phys. 15 (2004) 6832.

38. D. G. Fedorov, K. Kitaura, Chem. Phys. Lett. 597 (2014) 99.

39. S. R. Pruitt, C. Steinmann, J. H. Jensen, M. S. Gordon. J. Chem. Theo. Comp. 9, (2013): 2235.

Figure 1a. Geometric structure of $(H_2O)_{32}$ [colored by chemical elements as black (C), red (O), blue (N), and gray (H)].

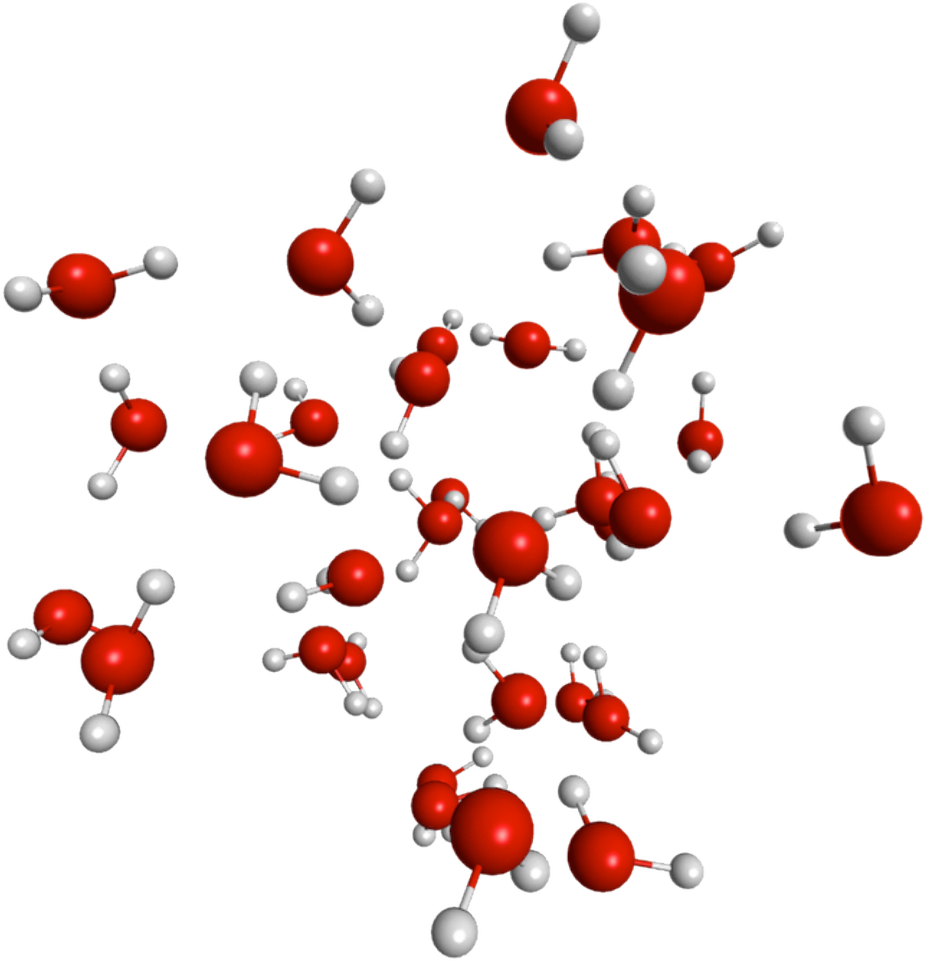

Figure 1b. Geometric structures of $(Ala)_7$ [colored by chemical elements as black (C), red (O), blue (N), and gray (H)].

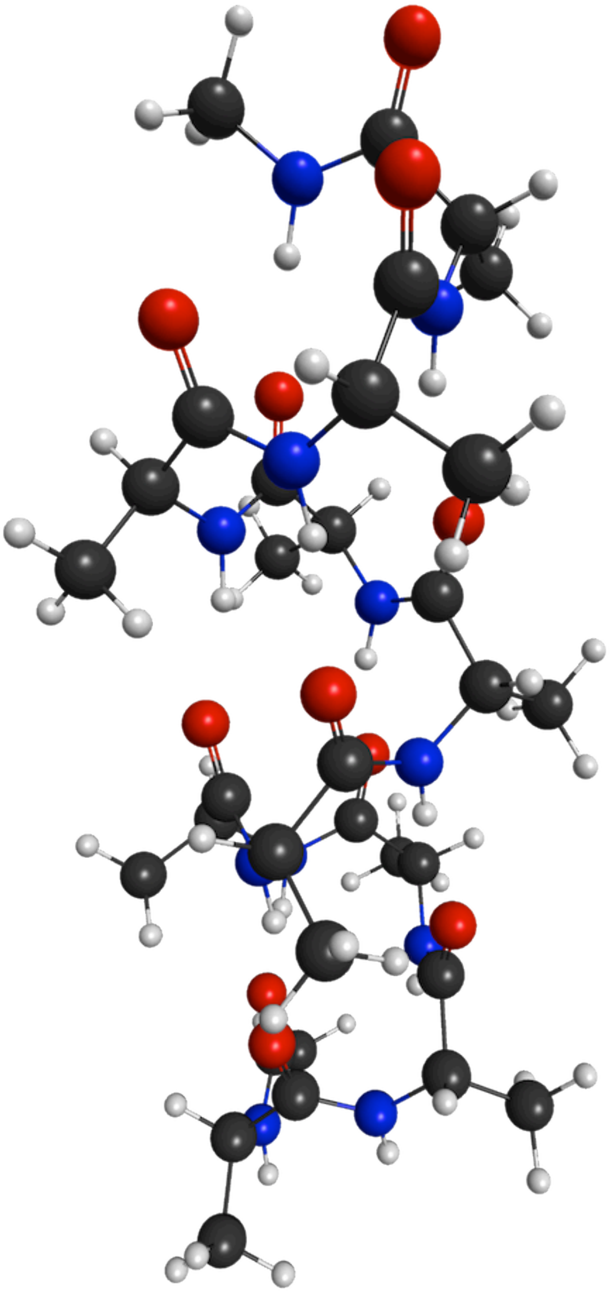

Figure 2a. Error of each gradient element relative to the numeric gradient for the $(H_2O)_{32}$ test system for (a) B3LYP/6-31G(d), RESDIM= 2.0, RESPPC= 2.0. Red squares are the gradient with response terms included in the gradient. Blue squares are the gradient without response terms included in the gradient.

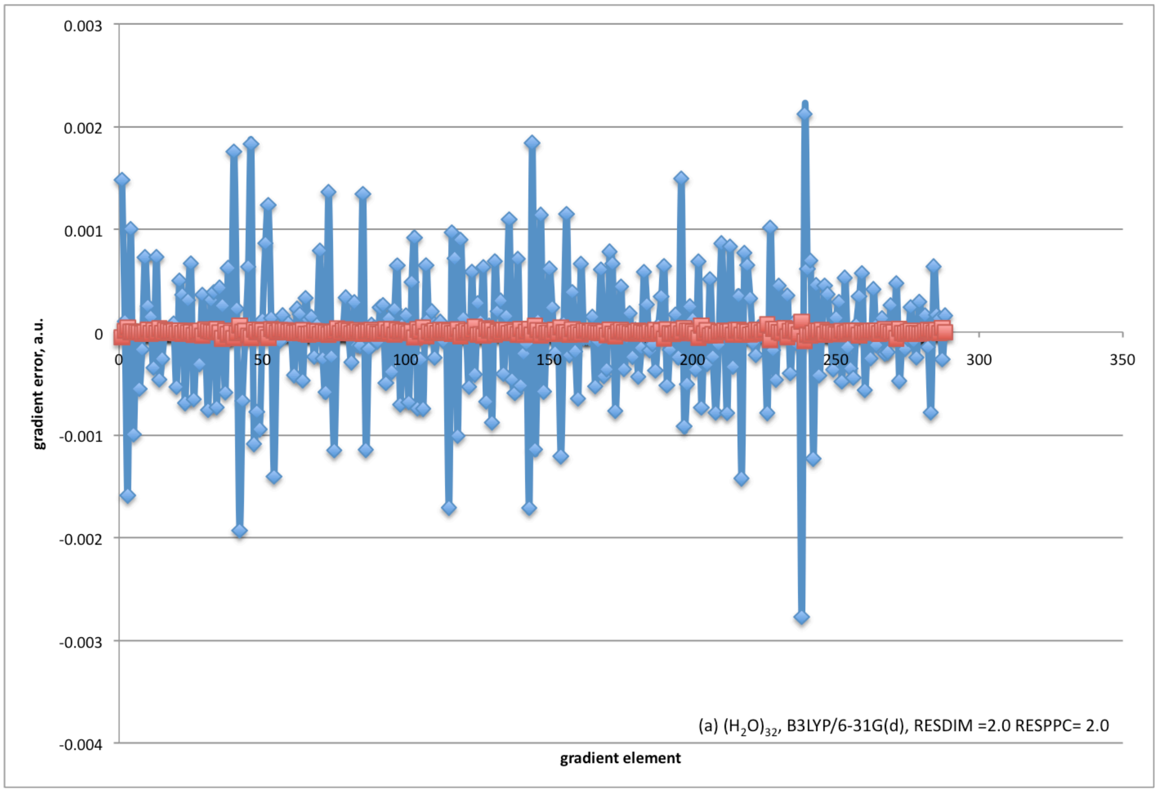

Figure 2b. Error of each gradient element relative to the numeric gradient for the $(H_2O)_{32}$ test system for B3LYP/6-311G(2d,2p), RESDIM= 2.0, RESPPC= 2.0. Red squares are the gradient with response terms included in the gradient. Blue squares are the gradient without response terms included in the gradient.

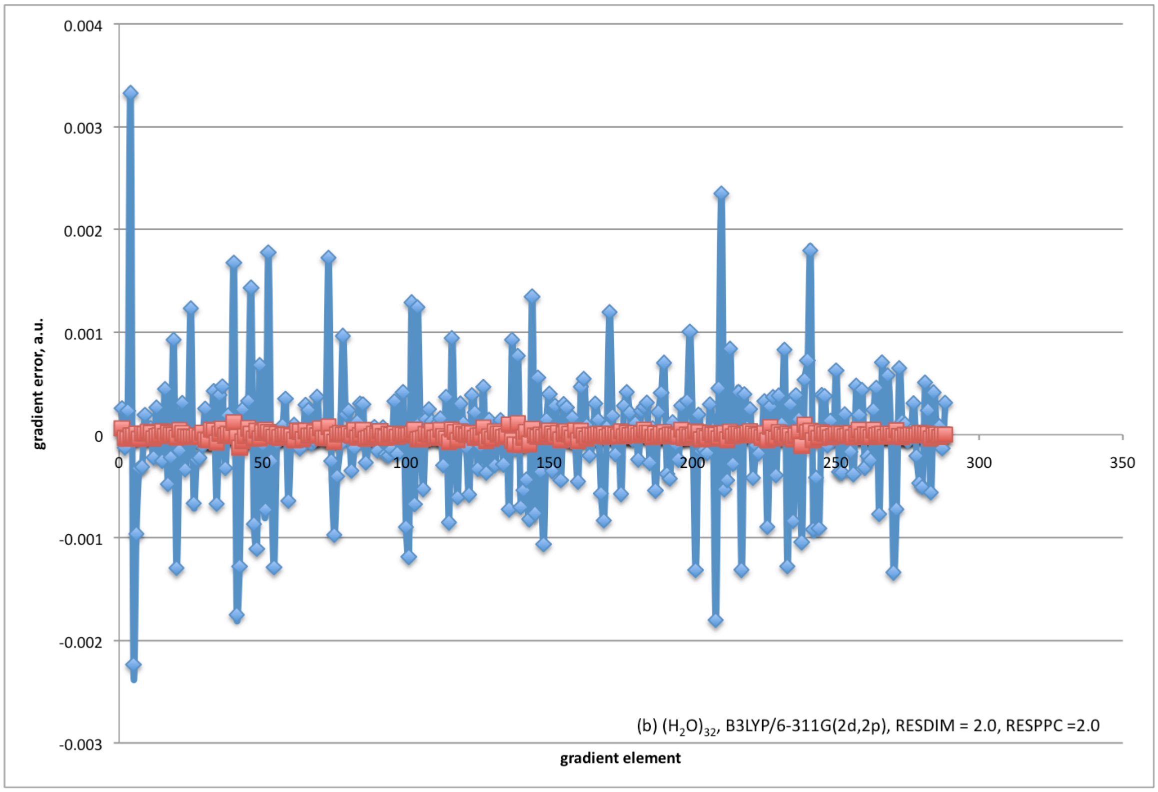

Figure 2c. Error of each gradient element relative to the numeric gradient for the $(H_2O)_{32}$ test system for B3LYP/6-31G(d), RESDIM=0.0, RESPPC=0.0. Red squares are the gradient with response terms included in the gradient. Blue squares are the gradient without response terms included in the gradient.

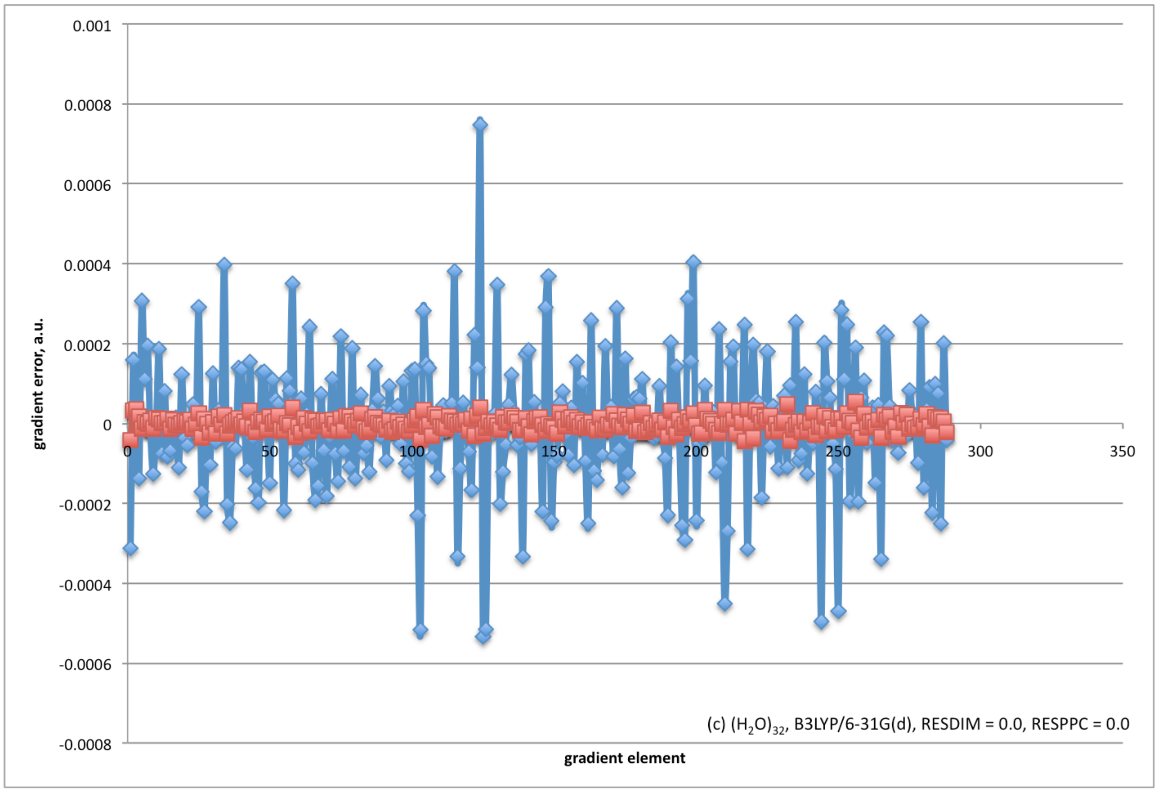

Figure 3a. Error of each gradient element relative to the numeric gradient for the $(H_2O)_{32}$ test system for BLYP/6-31G(d). Red squares are the gradient with response terms included in the gradient. Blue squares are the gradient without response terms included in the gradient. RESDIM and RESPPC were set to 2.0 for all calculations.

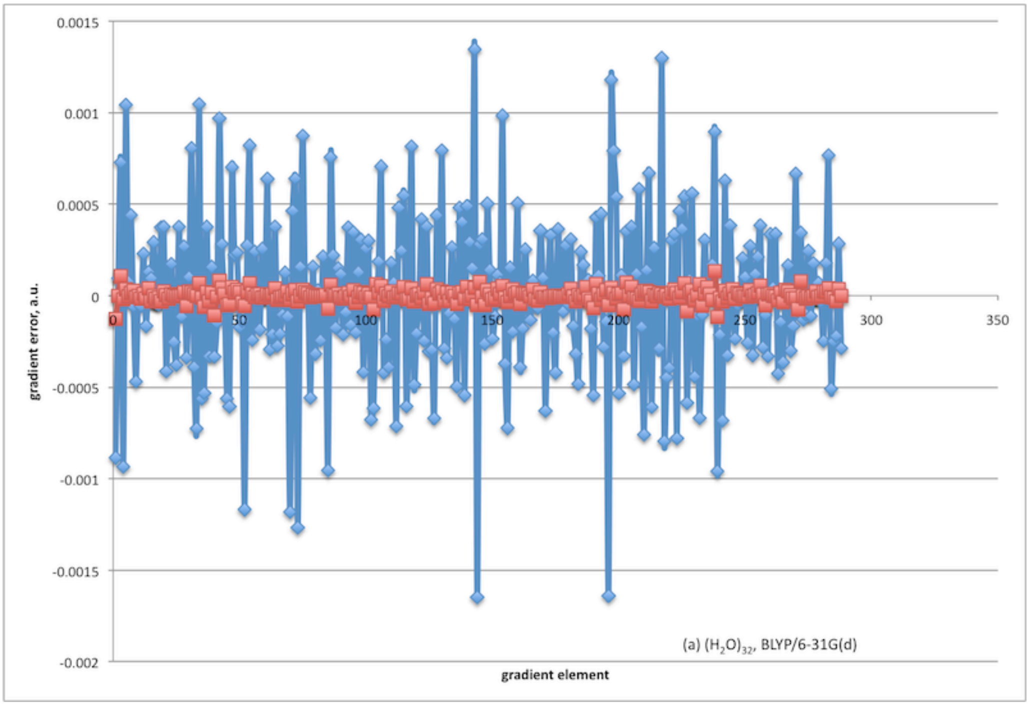

Figure 3b. Error of each gradient element relative to the numeric gradient for the $(H_2O)_{32}$ test system for PBE0/6-31G(d). Red squares are the gradient with response terms included in the gradient. Blue squares are the gradient without response terms included in the gradient. RESDIM and RESPPC were set to 2.0 for all calculations.

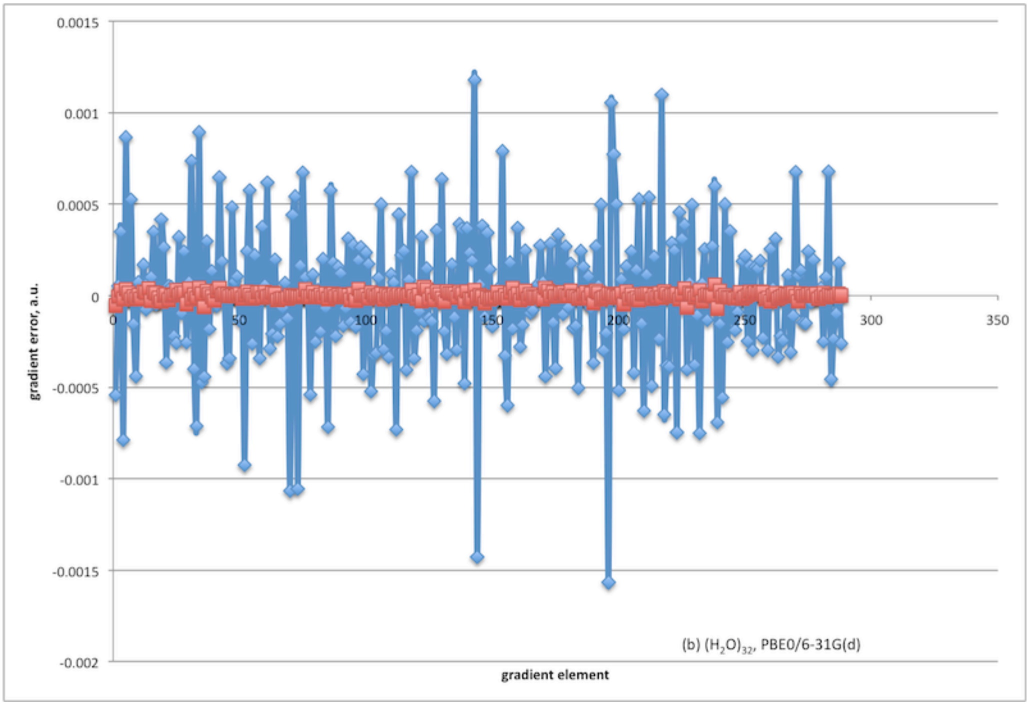

Figure 3c. Error of each gradient element relative to the numeric gradient for the $(H_2O)_{32}$ test system for SVWN/6-31G(d). Red squares are the gradient with response terms included in the gradient. Blue squares are the gradient without response terms included in the gradient. RESDIM and RESPPC were set to 2.0 for all calculations.

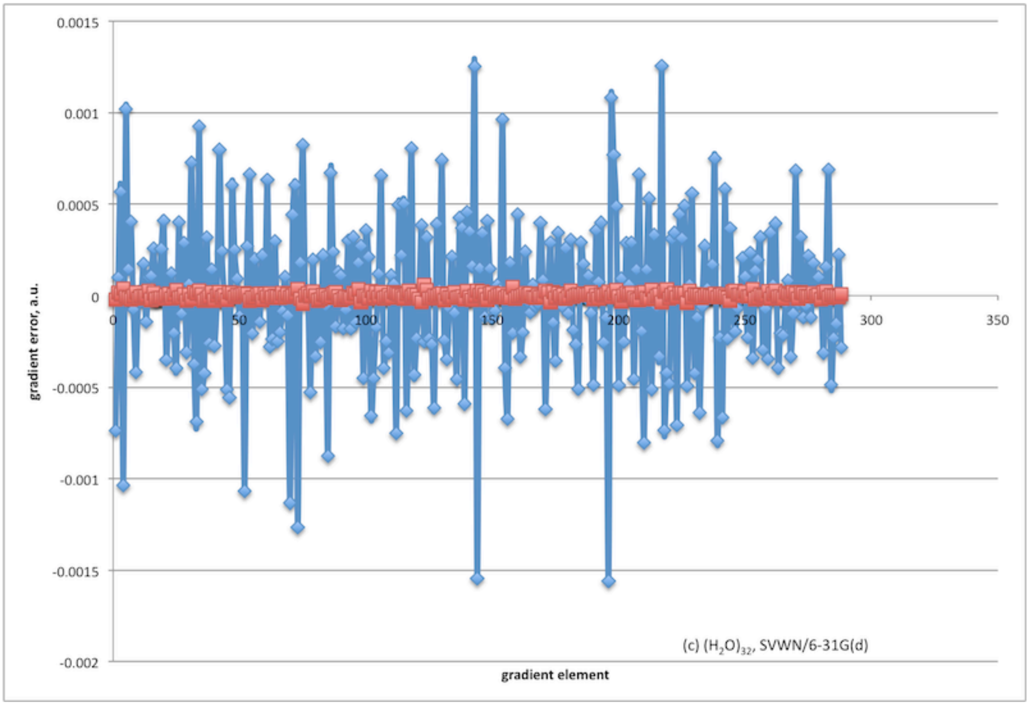

Figure 3d. Error of each gradient element relative to the numeric gradient for the $(H_2O)_{32}$ test system for HF/6-31G(d). Red squares are the gradient with response terms included in the gradient. Blue squares are the gradient without response terms included in the gradient. RESDIM and RESPPC were set to 2.0 for all calculations.

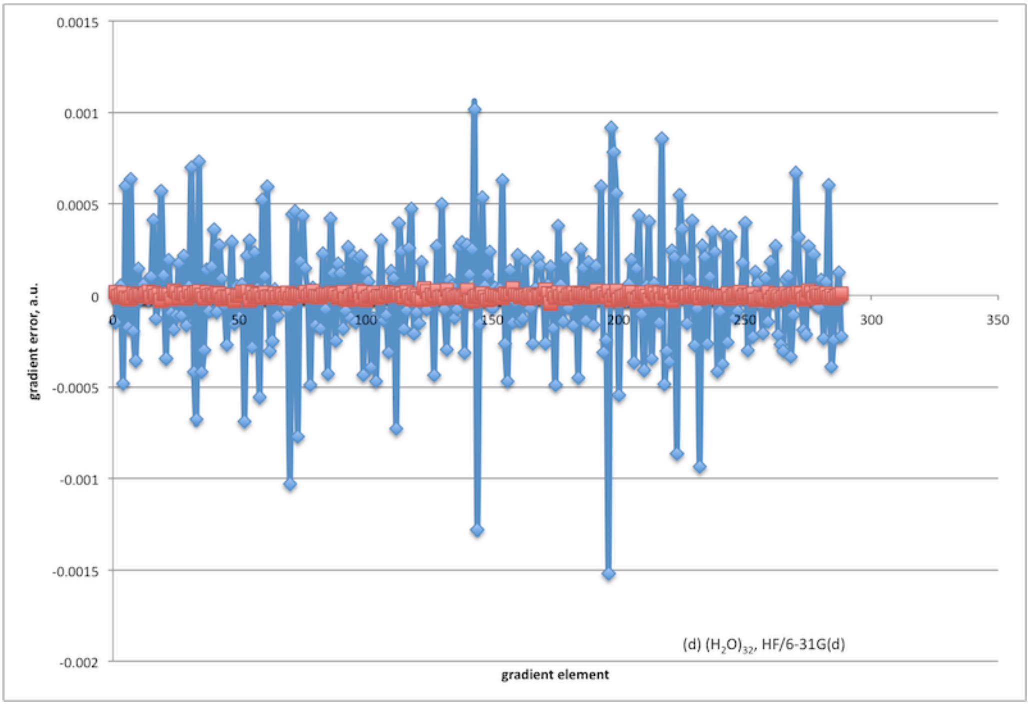

Figure 4a. Error of each gradient element relative to the numeric gradient for the $(Ala)_7$ test system for B3LYP/6-31G(d). Red squares are the gradient with response terms included in the gradient. Blue squares are the gradient without response terms included in the gradient. RESDIM and RESPPC were set to 2.0 for all calculations.

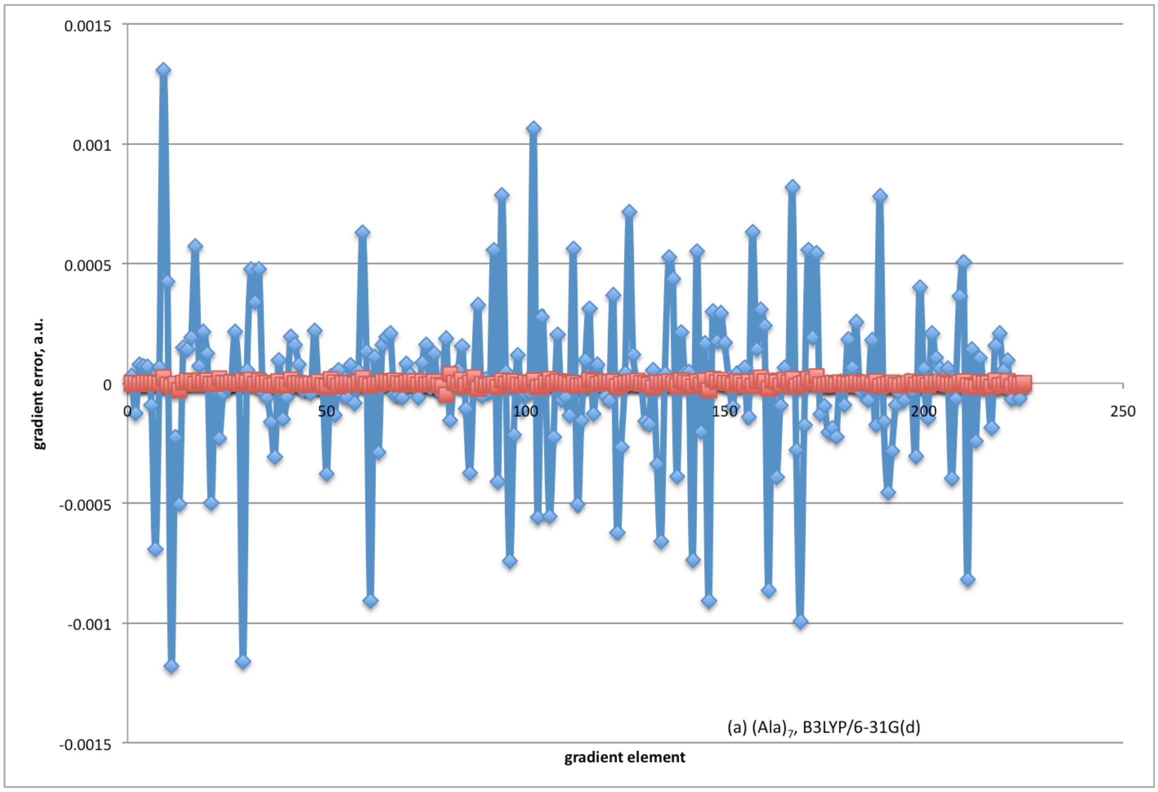

Figure 4b. Error of each gradient element relative to the numeric gradient for the $(Ala)_7$ test system for PBE0/6-31(d). Red squares are the gradient with response terms included in the gradient. Blue squares are the gradient without response terms included in the gradient. RESDIM and RESPPC were set to 2.0 for all calculations.

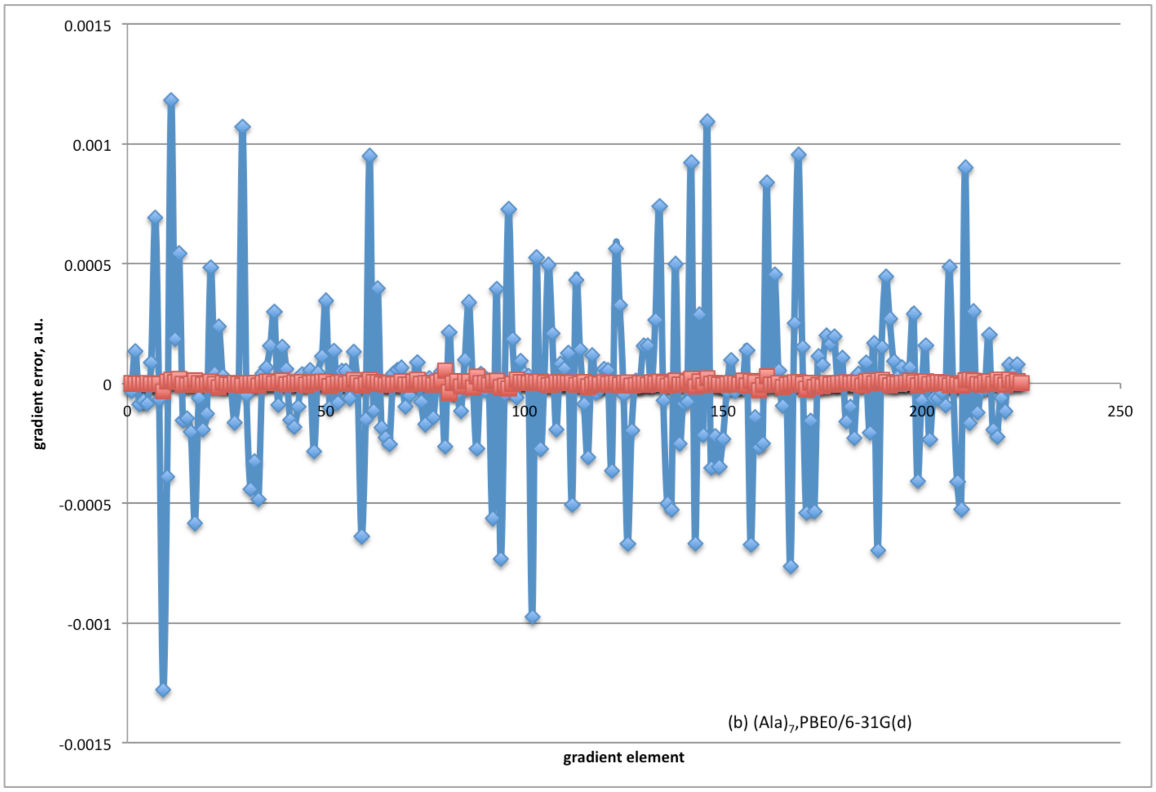

Figure 4c. Error of each gradient element relative to the numeric gradient for the $(\mathrm{Ala})_7$ test system for HF/6-31G(d). Red squares are the gradient with response terms included in the gradient. Blue squares are the gradient without response terms included in the gradient. RESDIM and RESPPC were set to 2.0 for all calculations.

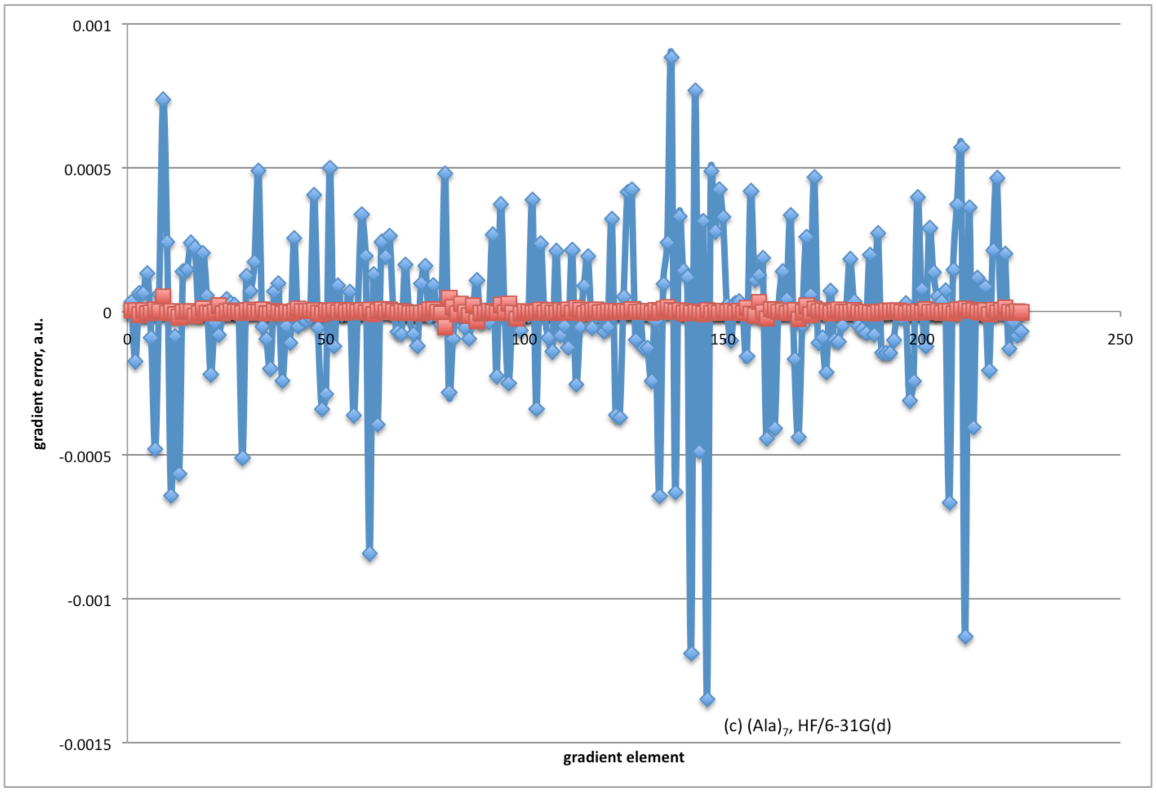

Table 1. The maximum absolute gradient value (MAX), the root mean square of the errors (RMS error), and the maximum absolute error in any gradient element (MAX error) for the FMO gradient with and without response terms included for the $(H_2O)_{32}$ cluster. The error in the numerical gradients is set to 0. Units are Hartree.

Gradient	MAX	RMS error	MAX error
$(H_2O)_{32}$, B3LYP/6-31G(d), RESPPC=2.0, RESDIM=2.0			
With response terms	0.031425	0.000023	0.000100
Without response terms	0.029790	0.000613	0.002122
$(H_2O)_{32}$, PBE0/6-31G(d), RESPPC=2.0, RESDIM=2.0			
With response terms	0.029265	0.000019	0.000071
Without response terms	0.029586	0.000377	0.001567
$(H_2O)_{32}$, BLYP/6-31G(d), RESPPC=2.0, RESDIM=2.0			
With response terms	0.040782	0.000032	0.000132
Without response terms	0.040278	0.000451	0.001649
$(H_2O)_{32}$, SVWN/6-31G(d), RESPPC=2.0, RESDIM=2.0			
With response terms	0.048558	0.000016	0.000057
Without response terms	0.049120	0.000421	0.001561
$(H_2O)_{32}$, B3LYP/6-31G(d), RESPPC=0.0, RESDIM=0.0			
With response terms	0.031230	0.000017	0.000053
Without response terms	0.031218	0.000164	0.000747
$(H_2O)_{32}$, B3LYP/6-311G(2d,2p), RESPPC=2.0, RESDIM=2.0			
With response terms	0.024845	0.000033	0.000125
Without response terms	0.024612	0.000612	.0003325
$(H_2O)_{32}$, HF/6-31G(d), RESPPC=2.0, RESDIM=2.0			
With response terms	0.029817	0.000014	0.000043
Without response terms	0.029600	0.000327	0.001520

Table 2. The maximum absolute gradient value (MAX), the root mean square of the errors (RMS error), and the maximum absolute error in any gradient element (MAX error) for the FMO gradient with and without response terms included for the (ALA)$_7$ polypeptide. RESDIM and RESPPC were set to 2.0 for all calculations. The error in the numerical gradients is set to 0. All units are in Hartree.

Gradient	MAX	RMS error	MAX error
(ALA)$_7$, B3LYP/6-31G(d)			
With response terms	0.631294	0.000010	.000038
Without response terms	0.631309	0.000332	.001308
(ALA)$_7$, PBE0/6-31G(d)			
With response terms	0.635749	0.0000091	0.000018
Without response terms	0.635756	0.000336	0.001279
(ALA)$_7$ HF/6-31G(d)			
With response terms	0.635648	.0000098	0.000054
Without response terms	0.635691	.000285	0.001349

Table 3. Comparison of the FMO-DFT and DFT gradients for the $(H_2O)_{32}$ cluster with response terms included. MAX = the maximum absolute value in the FMO-DFT gradient; RMSD = the root mean square difference between FMO-DFT gradient elements and DFT gradient elements; MAX diff = the maximum absolute difference between a FMO-DFT gradient element a DFT gradient element. RESDIM and RESPPC were set to 2.0 for all FMO calculations. Units are in a.u.

MAX	RMSD	MAX diff
	$(H_2O)_{32}$, B3LYP/6-31G(d)	
0.031425	0.001349	0.00544
	$(H_2O)_{32}$, PBE0/6-31G(d)	
0.029265	0.001176	0.00426
	$(H_2O)_{32}$, SVWN/6-31G(d)	
0.048558	0.001558	0.00533

Chapter 4. Fragment molecular orbital molecular dynamics with the fully analytic energy gradient

A paper published in *The Journal of Chemical Theory and Computation*

Kurt R. Brorsen, Noriyuki Minezawa, Feng Xu, Theresa L. Windus and Mark S. Gordon

Abstract

Fragment molecular orbital molecular dynamics (FMO-MD) with periodic boundary conditions is performed on liquid water using the analytic energy gradient, the electrostatic potential point charge approximation, and the electrostatic dimer approximation. Compared to previous FMO-MD simulations of water that used an approximate energy gradient, inclusion of the response terms to provide a fully analytic energy gradient results in better energy conservation in the NVE ensemble for liquid water. An FMO-MD simulation that includes the fully analytic energy gradient and two body corrections (FMO2) gives improved energy conservation compared with a previously calculated FMO-MD simulation with an approximate energy gradient and including up to three body corrections (FMO3).

1. Introduction

1.1 Fragment Molecular Orbital Method

Much progress has been made recently in improving algorithms *for ab initio* calculations on large systems[1,2]. One strategy is to use a fragmentation approach, in which a large system of interest is divided into smaller subsystems, and *ab initio* calculations are performed on these smaller subsystems[2]. One of the most successful and extensively developed fragmentation methods is the fragment molecular orbital (FMO) method[3] proposed by Kitaura et al. in 1999. The FMO method has been implemented for most *ab initio* and density functional theory (DFT) methods.[4-8] Numerous approximations to the original FMO method have been implemented to improve the efficiency of the calculation. The two most important of these approximations are the electrostatic point charge (ESP-PC) approximation and the electrostatic dimer (ES-DIM) approximation[9]. The ESP-PC approximation calculates the FMO embedded electrostatic potential using point charges rather than two electron integrals, while the ES-DIM approximation calculates the dimer energy of two fragments using point charges rather than using *ab initio* methods.

FMO gradients were developed soon after the introduction of the FMO method[10]. Improvements to the gradient followed that allowed the use of gradients with the ESP-PC approximation[11] and the ES-DIM approximation[12]. Because the dimer (or trimer) density is not iterated to self-consistency, the FMO2 (or FMO3) method is not variational. Consequently, response terms arising from the derivative of the molecular orbital coefficients with respect to nuclear coordinates must be included in the calculation of the first derivative. Because the inclusion of these response terms in the gradient requires the solution of the coupled perturbed Hartree-Fock equations, the original formulation of the FMO gradient neglected the response terms, based on the supposition that such terms make only small contributions to the gradient. Nagata et al.[13] solved these analytic gradient response equations for the FMO method at the restricted Hartree-Fock (RHF) level of theory (without the use of the ESP-PC approximation) by introducing the self-consistent Z-vector (SCZV) procedure. More recently, the response equations have been solved for and implemented for FMO-MP2[14] and for the general FMO method in which the ESP-PC approximation is included[15]. The corresponding analytic gradients for FMO-DFT will be forthcoming shortly.

1.2 FMO Molecular Dynamics

Komeiji et al. first implemented FMO2-molecular dynamics (FMO-MD) in 2003,[16,17] and many applications of FMO-MD have since been published[18-22]. The authors of the first implementation of FMO-MD[16] noted that the neglect of the response terms in the FMO gradient led to less than perfect energy conservation for a NVE ensemble, but this lack of energy conservation was deemed acceptable; since the fully analytic gradient had yet to be derived, there was no alternative.

Further improvements to the FMO-MD algorithm have been implemented, both to the FMO-MD method itself and to improve the energy conservation of FMO-MD[23]. The FMO3 method, in which explicit three body interactions are included in the FMO calculation, improves both the total energy and electron density of a FMO calculation.[24-26] This prompted the development of a FMO3-MD method to study water and protonated water systems[27] since three-body effects are important in water.[28] Although fully analytic FMO3 gradients have not yet been derived and implemented, it appears that using the FMO3 level of theory improves energy conservation in FMO-MD simulations.[23] Of course, while the FMO3 method is more accurate than FMO2 due to the explicit inclusion of three-body terms, it is likewise much more computationally demanding. It was recently demonstrated that FMO3-MD simulations (without periodic boundary conditions) are more than a factor of four more computationally expensive than a corresponding FMO2-MD simulation for water.[23] The inclusion of periodic boundary conditions will greatly increase this FMO3/FMO2 ratio, as many more calculations would have to be performed on triads of fragments when periodic boundary conditions are used. Therefore, from the perspective of computational expense, FMO2-MD is preferable if the accuracy of its energetics and forces is adequate. This is especially the case if one can guarantee good FMO2-MD energy conservation.

Another addition to FMO-MD in an attempt to improve energy conservation is dynamic fragmentation. [23,29,30] Dynamic fragmentation continually fragments a system over the course of a MD simulation, using a distance-based cutoff, and allows FMO-MD to describe processes such as proton transfer or chemical reactions. Dynamic fragmentation apparently improves energy conservation in FMO-MD simulations for systems such as a protonated water clusters.[23] While dynamic fragmentation seems to be beneficial for improving energy conservation for reactive systems, it is desirable to be able to run FMO-MD simulations without the need for dynamic fragmentation in order to reduce the complexity of FMO-MD runs.

All of the FMO-MD improvements described above have been implemented using a gradient that neglects the response terms. As noted above, the response terms for the FMO2-RHF method were recently derived and implemented using the SCZV procedure. [13] As analytic gradients are essential for accurate MD simulations, these response terms should be included in all FMO-MD calculations. In the original derivation of the SCZV procedure, the root mean square deviation error of the analytic gradient with response terms was shown[13] to improve the accuracy (measured by comparison to numerical gradients) for a single geometry by more than an order of magnitude, relative to the gradient in which the response terms are omitted. The new fully analytic gradient has also been combined with the effective fragment potential[31] to perform the first FMO-MD simulation with response terms included in the gradient. [32] These simulations showed good energy conservation.

The original implementation of the SCZV procedure assumed that the ESP-PC approximation was not used. This assumption severely restricts the use of the SCZV procedure for FMO-MD applications, since the ESP-PC approximation is normally applied in FMO calculations. Recently, Nagata, Fedorov and Kitaura[15] have solved for and implemented the response terms for the FMO gradient within the ESP-PC approximation. This improvement to the gradient allows accurate FMO-MD simulations to be performed, with all common FMO approximations implemented and available. With this recent improvement, it is shown here that accurate FMO-MD simulations, including periodic boundary conditions, are possible without the need to use the FMO3-MD level of theory.

2. Equations of Fragment Molecular Orbital Mehtod

In the following, a brief overview of the FMO2 restricted Hartree-Fock (RHF) energy is presented. Details and equations for the FMO gradient[10-13,15] and the FMO-MD method[16,17,23] can be found elsewhere.

The FMO2 energy for RHF is

$$E = \sum_{I}^{N} E_I^{'} + \sum_{I>J}^{N} (E_{IJ}^{'} - E_I^{'} - E_J^{'}) + \sum_{I>J}^{N} \mathrm{Tr}(\Delta \mathbf{D}^{IJ} \mathbf{V}^{IJ}), \qquad (1)$$

where N is the number of fragments, I or J are monomer fragments, IJ is a dimer consisting of fragments I and J, $E_X^{'}$ is the internal fragment energy, $\mathbf{V}^{IJ}$ is the matrix of the electrostatic potential, and $\Delta\mathbf{D}^{IJ}$ is the dimer density difference matrix.

The internal fragment energy, E'_X , is

$$E'_X = \sum_{\mu\nu\in X} D^X_{\mu\nu} h^X_{\mu\nu} + \frac{1}{2}\sum_{\mu\nu\lambda\sigma\in X}\left[D^X_{\mu\nu}D^X_{\lambda\sigma} - \frac{1}{2}D^X_{\mu\lambda}D^X_{\nu\sigma}\right](\mu\nu\,|\,\lambda\sigma) + E^{\mathrm{NR}}_X, \tag{2}$$

where $h^X_{\mu\nu}$ is the one-electron Hamiltonian of fragment X, E^{NR}_X is the nuclear repulsion potential energy of fragment X,

$$E^{\mathrm{NR}}_X = \sum_{B\in X}\sum_{A(\in X)>B}\frac{Z_A Z_B}{R_{AB}}, \tag{3}$$

$D^K_{\lambda\sigma}$ is the density matrix element of fragment K, and $(\mu\nu\,|\,\lambda\sigma)$ is a two-electron integral in the AO basis. The elements of $\mathbf{V}^{IJ}$ are expressed as

$$V^{IJ}_{\mu\nu} = \sum_{K\neq IJ}\left(u^K_{\mu\nu} + v^K_{\mu\nu}\right) \tag{4}$$

The one-electron and two electron terms In Eq. (4) are, respectively,

$$u^K_{\mu\nu} = \sum_{A\in K}\langle\mu|\frac{-Z_A}{|\mathbf{r}-\mathbf{R}_A|}|\nu\rangle, \tag{5}$$

$$v^K_{\mu\nu} = \sum_{\lambda\sigma\in K} D^K_{\lambda\sigma}(\mu\nu\,|\,\lambda\sigma).$$

The dimer density difference matrix $\Delta\mathbf{D}^{IJ}$ is defined as

$$\Delta\mathbf{D}^{IJ} = \mathbf{D}^{IJ} - (\mathbf{D}^I \oplus \mathbf{D}^J). \tag{6}$$

For distances R_{XK} between a monomer or dimer X and a fragment K in the ESP, that are greater than a user defined value R_{ESP-PC} , the two electron terms in the electrostatic potential are approximated as point charges:

$$v^{K}_{\mu\nu} \simeq \tilde{v}^{K}_{\mu\nu} = \sum_{A\in K} \left\langle \mu \left| \frac{Q_A}{\left|\mathbf{r}-\mathbf{R}_A\right|} \right| \nu \right\rangle, \tag{7}$$

where A is atom A in fragment K, Q_A is the nuclear charge on atom A, $\mathbf{R}_A$ is coordinate of atom A, $\mathbf{r}$ is the coordinate of fragment K, and μ and ν are atomic basis functions. This approximation is called the ESP-PC approximation and is used in most FMO calculations.

For a dimer *IJ*, if the monomer pair *I* and *J* are farther apart than the (user defined) value of R_{ES-DIM} the dimer energy is approximated as

$$E^{'}_{IJ} \cong E^{'}_{I} + E^{'}_{J} + \mathrm{Tr}(\mathbf{D}^{I}\mathbf{u}^{J}) + \mathrm{Tr}(\mathbf{D}^{J}\mathbf{u}^{I}) + \sum_{\mu\nu\in I}\sum_{\lambda\sigma\in J} D^{I}_{\mu\nu} D^{J}_{\lambda\sigma} (\mu\nu \mid \lambda\sigma) + \Delta E^{\mathrm{NR}}_{IJ}. \tag{8}$$

This approximation is called the ES-DIM approximation and reduces the number of *ab initio* dimer calculations that must be performed. The ES-DIM approximation is employed for most FMO calculations.

3. Computational Methods

A system of 32 water molecules was used to examine the accuracy of FMO-MD simulations with the ESP-PC approximation and response terms included in the gradient. This system was prepared by generating a random initial configuration of 32 waters inside a box (box length=9.865Å) , so that the density of the system matched that of water at 300 K. To equilibrate this system, a 50 ps classical MD simulation using the NVT ensemble at 300 K with an 0.5 fs step size was then performed using the previous random initial configuration as the starting point, and with randomized initial velocities so that the system temperature was 300 K. The force field used for the classical MD simulation was the general effective fragment potential (EFP2) method[33,34].

The final geometry produced by the classical MD equilibration was used as the initial geometry for the FMO-MD equilibration. The FMO-MD equilibration was performed using the NVT ensemble for 500 fs with a 1.0 fs step size and with randomized initial velocities to ensure that the temperature was maintained at 300 K. The Nose-Hoover thermostat with chains[35] was used to control the temperature. The velocity was randomized to a temperature of 300 K every 100 fs. For this FMO-MD equilibration, the ESP-PC approximation was not used and the cutoff value for the ES-DIM approximation was set to 1.5: if monomers I and J are more than 1.5 reduced distances, ρ_{IJ}, apart, then the *ab initio* dimer calculation is not performed, and the interaction between fragments I and J is approximated using point charges. The reduced distance is

$$\rho_{IJ} = r_{IJ} / (R_I + R_J), \tag{9}$$

In Eq. (9) r_{IJ} is the Euclidean distance between fragments I and J, and R_X is the van der Waals radius of fragment X. The response terms were included in the energy gradient. All waters in the FMO-MD equilibration were treated at the RHF/6-31G(d,p) level of theory.

The final configuration and velocities of the FMO-MD equilibration was then used as the initial configuration and velocities for FMO-MD simulations using the NVE ensemble to examine the accuracy of the recent FMO gradient improvements. These FMO-MD simulations were performed at the RHF/6-31G(d,p) level of theory for 50 ps using time steps in a range from 0.25-1.5 fs. Cutoff values were set to 4.75 for the ESP-PC approximation and 1.5 for the ES-DIM approximation, so that these approximations were used if two fragments are more than 4.75 and 1.5 reduced distances away, respectively. Two different FMO-MD simulations were performed at each time step - one simulation that included the response terms in the gradient and one that neglected the response terms.

For all FMO-MD calculations in this study, periodic boundary conditions (PBC) using the minimum image convention were employed[36]. Previous studies[23] of energy conservation for FMO-MD lacked PBC and instead employed a harmonic potential U that constrained the system to remain within a sphere centered at the origin:

$$U = K\left[\max(\mathbf{r}-\mathbf{r}_c,0)\right]^2 \tag{10}$$

where K is a force constant (set to 0.75 kcal/mol/Å^2 in the study), r is the distance to the origin, and r_c is the radius of the sphere. It is assumed in the present study that the use of PBC vs. the harmonic potential has no noticeable relative effect on energy conservation for the FMO-MD simulations. Previous studies[23] have shown that no dynamic fragmentation occurs for systems of pure water, so no dynamic fragmentation was employed. All FMO-MD simulations in this study were performed using the General Atomic and Molecular Electronic Structure System (GAMESS)[37,38].

The root mean square deviation of the total energy, *RMSD(E)*, was calculated for each of the FMO-MD NVE simulations as

$$RMSD(E) = \sqrt{\left\langle (E-\langle E\rangle\ )^2\right\rangle} \tag{11}$$

The velocity-Verlet method was used to integrate the equations of motion in this study. For the velocity-Verlet method, the *RMSD(E)* is proportional to the square of the time step, Δt [39]:

$$RMSD(E) \propto (\Delta t)^2 \tag{12}$$

Therefore, a log-log graph of *RMSD(E)* versus Δt should be linear with a slope of 2. This relationship was previously[16,23,32] used to evaluate the ability of FMO-MD simulations to produce an accurate NVE ensemble and will also be used for this study.

4. Results and Discussions

The log-log plot of *RMSD(E)* versus Δt is shown in Figure 1. Benchmarking fully molecular orbital molecular dynamics (MO-MD) simulations, in which MD is performed using *ab initio* methods with no fragmentation, were not performed in this study due to the computational cost of performing MO-MD with PBC. Previous FMO-MD studies of water[16,17,23] that have used MO-MD simulations as a benchmark have shown that MO-MD exhibits smaller *RMSD(E)* for a given time step than FMO-MD, for all variations of FMO-MD that were available at the time. It is therefore assumed in this study that with identical initial conditions, a smaller *RMSD(E)* for a given MD simulation is always closer to the MO-MD value and therefore more accurate. Previous studies[23] have also shown that the velocity-Verlet integrator begins to fail for MO-MD simulations with a large time step and have therefore focused on the time step range of 0.25-1.0 fs for which the MO-MD simulations have consistently shown perfect energy conservation based on a log-log plot of *RMSD(E)* versus Δt with a slope of 2.

The FMO2-MD plot in Figure 1 demonstrates a significant improvement in energy conservation when the response terms are included in the energy gradient (Figure 1). Both simulations with and without response terms included show a decrease in energy conservation over the time step range of 0.25-0.4 fs, but the FMO2-MD simulation with the response terms included is still more robust than is the FMO2-MD simulation without response terms. For larger step sizes Δt, the *RMSD(E)* values for the two sets of simulations begin to converge at ~1.5 fs. The energy conservation begins to fail for both sets of MD simulations in the range of 0.25-0.4 fs. On the other hand, for the time step range in which most FMO-MD simulations will likely be performed (0.4-1.0 fs), a least squares line of best fit to the data has a slope of 1.948 for the FMO2-MD simulations that include response terms versus a slope of 0.772 for the FMO2-MD simulations that lack response terms. As a MD simulation exhibiting perfect energy conservation would have a best fit line with a slope of 2.0, the slopes of the best fit lines of the FMO2-MD simulations illustrate the necessity of adding response terms to the FMO gradient in order to obtain robust FMO2-MD simulations.

Even with the response terms added, the *RMSD(E)* becomes constant at small time step values indicating that residual errors remain in the FMO gradient. These residual errors are likely due to the fragmentation employed by the FMO method and are inherent to any FMO-MD simulation. These residual errors could be further reduced by including higher body corrections to the FMO method (FMO3, FMO4, etc.) The residual errors would be completely eliminated at the limit of a full *ab initio* calculation on the entire system without fragmentation. Indeed, the reduction in residual errors with the addition of higher body corrections is seen in Figure 2 where the FMO3-MD results appear to trend to a smaller constant than FMO2-MD results.

The results presented in Figure 1 for the FMO2-MD simulation without response terms have a shape that is qualitatively similar to that of the previous FMO2-MD results[23] that are presented in Figure 2. As these two FMO2-MD simulations are performed on identical systems of 32 waters at the RHF/6-31G(d,p) level of theory, these curves should in theory have the same *RMSD(E)* values, but this is not the case. The FMO2-MD simulation (with no response terms) performed in the present work has a higher *RMSD(E)* for a given time step than the previous study. This difference in the *RMSD(E)* is due to differences in how the classical and FMO-MD equilibrations were performed and the use of different initial geometries and velocities for the FMO2-MD simulations. However, the *RMSD(E)* differences between the two curves is less important than how closely the slope of each curve aligns with a line of slope 2. Also important is the relative shape of each curve with regard to the degree of energy conservation. From this perspective, both of the FMO2-MD simulations without response terms show similar, if not identical, energy conservation. Therefore, the FMO2-MD simulations without response terms can be treated as similar to one another.

Now, recall that the FMO2-MD and FMO3-MD curves in Figure 2 were computed without the response terms. Comparing the curves in Figure 1 with those in Figure 2, the curve for the FMO2-MD simulation with the response terms included appears to show a greater improvement over the FMO2-MD curve without response terms than does the FMO3-MD curve in Figure 2. This can be seen by examining the ratio of *RMSD(E)* values for the FMO2-MD simulations with and without response terms in Figure 1 and the ratio of *RMSD(E)* values for the FMO3-MD and FMO2-MD simulations, both without response terms in Figure 2. These comparisons are presented in Table 1. It is assumed that the two FMO2-MD curves without response terms in Figure 1 and Figure 2 can be treated as essentially the same, differing only due to different initial conditions. Therefore, referring to time steps in the range 0.4-1.0 fs in Table 1, the ratio for the FMO2-MD simulations with vs. without response terms is slightly greater than the corresponding ratio for FMO3 vs. FMO2, both without response terms. This suggests that the energy conservation improves at least as much by including response terms in FMO2-MD simulations as it does by choosing FMO3 without response terms. When one considers the additional computational expense incurred by choosing FMO3, FMO3-MD is a logical choice only when the system demands it due to the superior description of energetics and electron density of FMO3. It is also important to emphasize that FMO3 MD without a fully analytic gradient is not guaranteed to provide acceptable energy conservation, and therefore acceptable predictions of bulk properties, in all cases.

5. Conclusions and Future Studies

Accurate gradients are essential for producing correct forces in MD simulations. This can be seen for MD simulations with incomplete or inaccurate gradients, in which case energy conservation is violated for the NVE ensemble. For the FMO method, accurate gradients require the addition of the response terms obtained from the SCZV procedure. Therefore, it is necessary to include the response terms for all FMO-MD simulations. This practice has not been consistently followed in previous FMO-MD applications,[19,21,22] in part because the fully analytic gradients have only recently been made available. Response terms for the FMO-MP2 gradient have been shown to improve the accuracy of the FMO-MP2 gradient even more than the corresponding response terms for the FMO-RHF method.[14] Therefore, for FMO-MD simulations that include electron correlation, the addition of the response terms will be even more important than it is for FMO-RHF MD simulations. To date, response terms have not been implemented for other correlated *ab initio* methods. The response terms for FMO-DFT will be presented in a future paper. The lack of response terms for FMO interfaced with other *ab initio* methods limits the potential applications of FMO-MD for these methods, so solving for these response terms is a promising future research direction. Additionally, response terms have yet to be derived for FMO3. Since FMO3 is necessary for an accurate description of some systems and for FMO-MD with smaller time steps, the derivation and implementation of these response terms would be beneficial for future FMO-MD studies.

6. Acknowledgements

This work was supported in part by a National Science Foundation Petascale Applications grant and in part by a Department of Energy Chemistry End Station grant, both to MSG and TLW. KRB is supported by a US Department of Energy Computational Science Graduate Fellowship. The authors are grateful for the inspirational work in the field of analytic gradients and potential energy surfaces. The authors also thank Yuto Komeiji for graciously providing FMO-MD data from reference 23.

References

1. *Linear-Scaling Techniques in Computational Chemistry and Physics*, Zalesny R.; Papadopoulos, M. G. ; Mezey, P. G.; J. Leszczynski Eds.; Springer: Berlin, 2011.

2. Gordon, M. S. ; Fedorov, D. G.; Pruitt, S. R.; Slipchenko, L. V. *Chem. Rev.* **2012**, *112*, 632.

(3. Kitaura, K.; Ikeo, E.; Asada, T.; Nakano, T.; Uebayasi, M. *Chem. Phys. Lett.* **1999**, *313*, 701.

4. Fedorov, D. G.; Kitaura, K. *J. Chem. Phys*. **2004**, *121*, 2483.

5. Mochizuki, Y.; Yamashita, K.; Fukuzawa, K.; Takematsu, K.; Watanabe, H.; Taguchi, N; Okiyama, Y.; Tsuboi, M.; Nakano, T.; Tanaka, S. *Chem. Phys. Lett.* **2010,** *493*, 346.

6. Fedorov, D. G.; Kitaura, K. *J. Chem. Phys.* **2010**, *123*, 134103.

7. Sugiki, S. I.; Kurita, N.; Sengoku, Y.; Sekino, H. *Chem. Phys. Lett.* **2003**, *382*, 611.

8. Fedorov, D. G.; Kitaura, K. *Chem. Phys. Lett.* **2004**, *389*, 129.

9. Nakano, T.; Kaminuma, T.; Sato, T.; Fukuzawa, K.; Akiyama, Y.; Uebayasi, M.; Kitaura, K. *Chem. Phys. Lett.* **2002**, *351*, 475.

10. Kitaura, K.; Sugiki, S. I.; Nakano, T.; Komeiji, Y.; Uebayasi, M. *Chem. Phys. Lett.* **2001**, *336*, 163.

11. Nagata, T.; Fedorov, D. G.; Kitaura, K. *Chem. Phys. Lett.* **2009**, *475*, 124.

12. Nagata, T.; Fedorov, D. G.; Kitaura, K. *Chem. Phys. Lett.* **2010**, *492*, 302.

13. Nagata, T.; Brorsen, K.; Fedorov, D. G.; Kitaura, K.; Gordon, M. S. *J. Chem. Phys.* **2011**, *134*, 124115.

14. Nagata, T.; Fedorov, D. G.; Li, H.; Kitaura, K. *J. Chem. Phys.* **2012**, *136*, 204112.

15. Nagata, T.; Fedorov, D. G.; Kitaura, K. *Chem. Phys. Lett.* **2012**, *544*, 87.

16. Komeiji, Y.; Nakano, T.; Fukuzawa, K.; Ueno, Y.; Inadomi, Y.; Nemoto, T.; Uebayasi, M.; Fedorov, D. G.; K, Kitaura, *Chem. Phys. Lett.* **2003**, *372*, 342.

17. Komeiji, Y.; Inadomi, Y.; Nakano, T. *Comput. Biol. Chem.* **2004**, *28*, 155.

18. Komeiji, Y.; Mochizuki, Y.; Nakano, T.; Fedorov, D.G. *Theochem* **2009**, *898*, 2.

19. Mochizuki, Y.; Komeiji, Y.; Ishikawa, T.; Nakano, T.; Yamataka, H. *Chem. Phys. Lett.* **2007**, *437*, 66.

20. Fedorov, D.G.; Ishida, T.; Kitaura, K. *J. Phys. Chem. A* **2005**, *109,* 2638.

21. Sato, M.; Yamataka, H.; Komeiji, Y; Mochizuki, Y.; Ishikawa, T; Nakano, T. *J. Am. Chem .Soc.* **2008**, *130,* 2396.

22. Komeiji, Y; Ishikawa, T; Mochizuki, Y; Yamataka, H; Nakano, T. *J. Comput. Chem.* **2009**, *30*, 40.

23. Komeiji, Y.; Mochizuki, Y.; Nakano, T *Chem. Phys. Lett.* **2010**, *484*, 380.

24. Fedorov, D. G.; Kitaura, K. *J. Chem. Phys.* **2004**, *120*, 6832.

25. Fedorov, D. G.; Kitaura, K. *Chem. Phys. Lett.* **2006**, *433*, 182.

26. Fujita, T.; Fukuzawa, K.; Mochizuki, Y.; Nakano, T.; Tanaka, S. *Chem. Phys. Lett.* **2009**, *478*, 295.

27. Fedorov, D. G.; Kitaura, K. *J. Chem. Phys.* **2004**, *120*, 6832.

28. Xantheas, S. S. *Chem. Phys.* **2000**, *258*, 225.

29. Mochizuki, Y.; Komeiji, Y.; Ishikawa, T.; Nakano, T.; Yamataka, H. *Chem. Phys. Lett.* **2007**, *437*, 66.

30. Komeiji, Y.; Ishikawa, T.; Mochizuki, Y.; Yamataka, H.; Nakano, T. *J. Comput. Chem.* **2009**, *30*, 40.

31. Gordon, M. S.; Slipchenko, L.; Li, H.; Jensen, J. H. *Ann. Rep. Comp.* Chem., **2007**, *3*, 177.

32. Nagata, T.; Fedorov, D. G.; Kitaura, K. *Theochem.* **2012**, *131*, 1136.

33. Day, N. P.; Jensen, H. J.; Gordon, M. S.; Webb, P. S. *J. Chem. Phys.* **1996**, *105*, 1968.

34. Gordon, M. S.; Freitag, M. A.; Bandyopadhyay, P.; Jensen, J. H.; Kairys, V.; Stevens, W. J. *J. Phys. Chem.* **2001**, *105*, 293.

35. Harvey, S. C.; Tan, R. K. Z.; Cheatham III, T.E. *J. Comput. Chem.* **1998**, *19*, 726.

36. Fujita, T.; Nakano, T.; Tanaka, S. *Chem. Phys. Lett.* **2011**, *506, 112.*

37. Schmidt, M. W.; Baldridge, K. K.; Boatz, J. A.; Elbert, S. T.; Gordon, M. S.; Jensen, J. H.; Koseki, S.; Matsunaga, N.; Nguyen, K. A.; Su, S.; Windus, T. L.; Dupuis, M.; Montgomery, J. A. *J. Comput. Chem.* **1993**, *14,* 1347 .

38. Gordon, M. S.; Schmidt, M. W. *Theory and Applications of Computational Chemistry, the first forty years*, Elsevier: Amsterdam, 2005.

39. Haile, J. M. *Molecular Dynamics Simulation – Elementary Methods*; Wiley: NY,1992.

Figure 1. Log-log plot of the RMSD(E) vs. Δt for FMO2-MD with and without response terms as performed in this study.

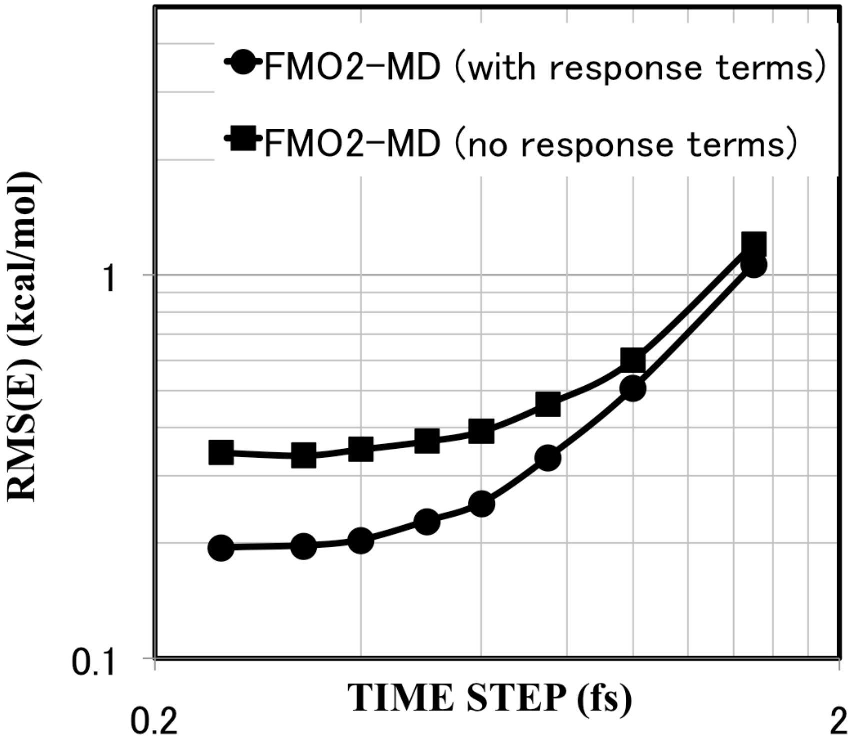

Figure 2. Log-log plot of the RMSD(E) vs. Δt for FMO2-MD and FMO3-MD without response terms and MO-MD from a previous study[23].

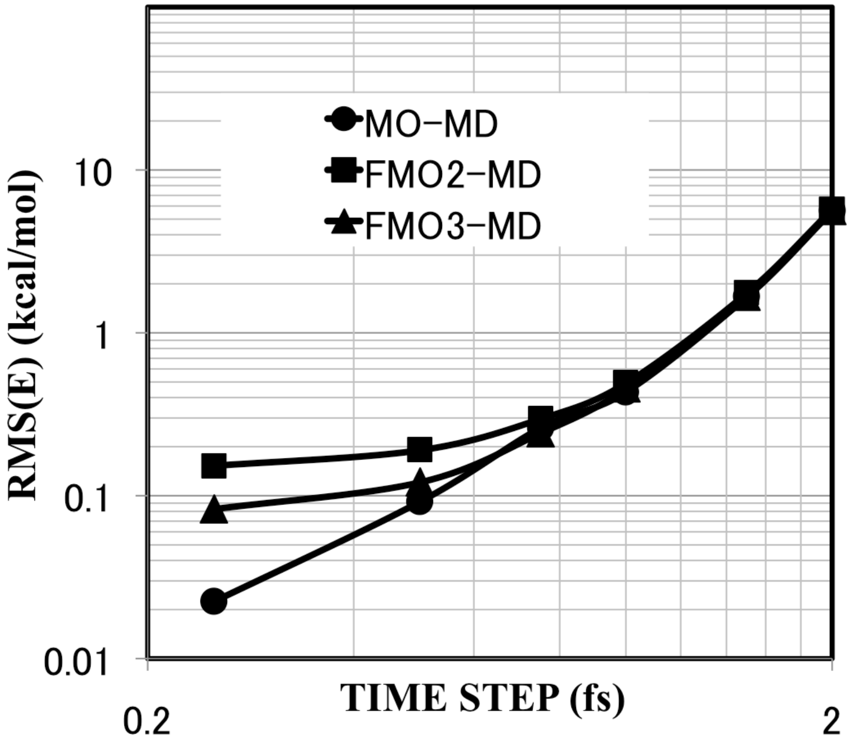

Table 1 Ratio of the *RMSD(E)* for various FMO2-MD time steps with and without response terms (performed in this study) and for FMO3-MD and FMO2-MD both without response terms performed in a previous study[23].

Time step (fs)	FMO2-MD without response terms/FMO2-MD with response terms	FMO2-MD/FMO3-MD
0.25	1.77	1.85
0.5	1.62	1.58
0.75	1.38	1.23
1.0	1.19	1.09
1.5	1.13	1.06

Chapter 5. Surface affinity of the hydronium ion: The effective fragment potential and umbrella sampling

A paper to be submitted to *The Journal of Physical Chemistry*

Kurt R. Brorsen, Spencer R. Pruitt, Mark S. Gordon

Abstract

The surface affinity of the hydronium ion in water is investigated with umbrella sampling and classical molecular dynamics simulations, in which the system is described with the effective fragment potential (EFP). The solvated hydronium ion is also explored using second order perturbation theory for the hydronium ion and the empirical TIP5P potential for the waters. Umbrella sampling is used to analyze the surface affinity of the hydronium ion, varying the number of solvent water molecules from 32 to 256. Umbrella sampling with the EFP method predicts the hydronium ion to most probably lie about halfway between the center and edge of the water cluster, independent of the cluster size. Umbrella sampling using MP2 for the hydronium ion and TIP5P for the solvating waters predicts that the solvated proton most probably lies about 0.5-2.0 Å from the edge of the water cluster independent of the cluster size.

1. Introduction

The solvated proton is of great importance in chemistry, occurring in a wide variety of natural settings, such as biological phenomena, surface science, and interstellar chemistry and has been widely studied experimentally and computationally.[1-16] Of particular interest is the surface affinity of the solvated proton, since if the proton demonstrates a surface affinity the proton could catalyze acid-base reactions at the interface. A general consensus has emerged that the solvated proton demonstrates a surface affinity, though there is conflicting evidence regarding the cause of the surface affinity.

Ideally, computational studies of the solvated proton should be performed with *ab initio* molecular dynamics (AIMD) simulations.[17] The solvated proton is shared and transported among many different water molecules over the course of molecular dynamics (MD) simulations through the Grotthuss shuttling mechanism,[18,19] and AIMD can account for the changing bonding topology of the solvated proton. However, AIMD simulations of the solvated proton are difficult due to their computational expense and are therefore limited to smaller system sizes and shorter simulations. While there has been some success with AIMD simulations on larger systems using Car-Parinello density functional theory,[8,9] most MD simulations of the solvated proton have used either a classical molecular mechanics (MM) force field or a QM/MM description of the system.

Classical or QM/MM MD simulations of the solvated proton can be broadly separated into two groups: simulations that account for the Grotthuss shuttling mechanism through the use of the multistate empirical valence bond method[20,21] (MS-EVB) or other similar methods and simulations that treat the solvated proton as existing in either the limiting form of the Eigen[22] (H_3O^+) or Zundel[23] ($H_5O_2^+$) cation. While methods that include the Grotthuss shuttling mechanism are more physically correct in the way they account for proton transport, classical or QM/MM simulations in which the Grotthuss shuttling mechanism is ignored have described the surface affinity of the solvated proton in water reasonably well.[1,3,6,13] The limiting form of the Eigen cation, the hydronium ion, is the focus of the present study. Both a model potential and a QM/MM approach are used.

The effective fragment potential[24,25] (EFP) is a one-electron model potential with fixed internal geometry. EFP calculations compute the interaction energy between fragments. In a typical EFP calculation, each molecule is treated as a fragment. The EFP interaction parameters are derived from an *ab initio* calculation. For neutral water clusters, the EFP method correctly reproduces the relative energies and geometries of second order Møller-Plesset (MP2) perturbation theory at orders of magnitude lower computational cost.[25-27] The EFP method has also successfully been used to model ion solvation.[28,29] For the protonated water cluster, one would expect that the EFP method will provide a level of accuracy similar to that of correlated electronic structure theory at a significantly smaller computational cost.[30] The present study employs the general EFP2 method for both the solute hydronium ion and the solvent water, in combination with umbrella sampling to calculate the probability distribution function of the hydronium ion as a function of the distance of the center of mass of the hydronium ion from the center of the cluster. A previous study used umbrella sampling to calculate the surface affinity of the hydronium ion using a polarizable force field.[11] Umbrella sampling has also been combined with the EFP2 method to accurately compute the hydration structures of salts[31] and absolute pK_a values.[32]

2. Computational Methods

The surface affinity of the hydronium ion was calculated using NVT MD simulations with umbrella sampling. To systematically investigate the H_3O^+ surface affinity as a function of cluster size, simulations were performed with one H_3O^+ and 32, 64, 128, or 256 solvating water molecules. All MD simulations were performed using the electronic structure program GAMESS.[33]

In addition to the EFP2 simulations, an analogous set of calculations were performed in which the H_3O^+ is represented with second order perturbation theory (MP2) and the aug-cc-pVDZ basis set, and the waters are described with the TIP5P potential[34] (MP2/TIP5P).

For each umbrella sampling calculation, a harmonic spherical boundary potential centered at the origin was used to prevent evaporation. The force constant for the spherical boundary potential was set to 3.0 kcal/mol/$Å^2$ and the edge of the spherical boundary potential was set such that the density of each cluster would be equal to the density of water at 300 K if all molecules were inside the spherical boundary potential. For 32, 64, 128, and 256 solvating waters, the edge of the spherical boundary was set to 6.2, 7.8, 9.7, and 12.2 Å from the origin, respectively. For the umbrella sampling, windows were selected every 0.5 Å, starting at the origin and ending at the edge of the spherical boundary potential. For 32, 64, 128, and 256 solvating waters there were 13, 16, 20, and 26 windows, respectively. The force constant for the umbrella sampling constraint was set to 2.0 kcal/mol/$Å^2$. The force constants for the spherical boundary potential and umbrella sampling constraint were chosen to ensure adequate sampling and overlap among the umbrella sampling simulations.

For each combination of cluster size, level of theory, and window, initial NVT equilibrations were performed for 20 ps at 300 K. The final configurations of the equilibration were then used for NVT production simulations for 100 ps at 300 K. The NVT simulations all used the velocity-Verlet integration and a step size of 1.0 fs.

To improve the convergence of the probability distribution function for the EFP2 simulations with 256 solvating water molecules, two additional MD simulations with umbrella sampling were performed with windows at 9.5 and 10.5 Å from the center of the cluster. The additional calculations used the same MD, spherical boundary potential, and umbrella sampling protocol as the other MD simulations with umbrella sampling.

The probability distribution function for each cluster size and level of theory was then obtained from the production simulations by the weighted histogram analysis method (WHAM).[35,36]

3. Results and Discussion

The probability distribution functions for each cluster size and combination of theory are presented in Figure 1. For all cluster sizes, EFP2 predicts the hydronium ion to lie closer to the center of the water cluster than does MP2/TIP5P.

For the hydronium ion solvated by 32 waters, EFP2 and MP2/TIP5P predict that the hydronium ion most probably lies about ½ and ¾ of the way between the center and the edge of the water cluster respectively, where the edge of the water cluster is defined as the start of the spherical boundary potential. The greatest probability for finding H_3O^+ corresponds to a distance from the edge of the water cluster of about 2.5-3.5 Å for EFP2 and about 0.5-2.0 Å for MP2/TIP5P. The EFP2 and MP2/TIP5P probability density functions maintain common features as the water cluster size is increased. MP2/TIP5P predicts that the hydronium ion most probably lies at a distance of about 0.5-2.0 Å from the surface of the water cluster independent of the water cluster size. EFP2 predicts that the hydronium ion most probably lies about ½ of the way from the center to the surface of the water cluster independent of water cluster size.

For all cluster sizes, the peaks in the MP2/TIP5P probability distribution functions are sharper and higher than the corresponding EFP2 probability distribution functions. The sharp MP2/TIP5P probability distribution function indicates that for MP2/TIP5P the hydronium ion is unlikely to be found outside the most probable region of space of 0.5-2.0 Å from the edge of the water cluster. The more diffuse EFP2 probability distribution function indicates that while the hydronium ion is most likely to be found at a distance of about ½ of the way from the center to the surface of the water cluster, the hydronium ion is much less constrained to one region of space than is the case with MP2/TIP5P.

Both the MP2/TIP5P and EFP2 probability distribution functions show smaller propensities for the hydronium ion to be near the center of the water cluster than in other regions of the water cluster. There is a stronger surface affinity for MP2/TIP5P than there is for EFP2, so MP2/TIP5P predicts a low probability for the hydronium ion to be at the center of the water cluster. It is important to stress that unlike the potential of mean force, the probability distribution function does not need to be corrected with the inclusion of a volume-entropy term.[37] The present study is focused on where the hydronium ion is most likely to be found in a water cluster.

The MP2/TIP5P results agree with much of the recent literature[11-16] by predicting that the hydronium ion demonstrates a modest surface affinity. The EFP2 method differs from much of the recent literature by predicting that the hydronium ion does not demonstrate a significant surface affinity. The EFP2 method predicts that it is most probable to find the hydronium ion halfway between the center and edge of the cluster independent of the water cluster size. However, as noted above, the EFP2 probability distribution is rather broad and indistinct.

There are two possible origins for the difference between the EFP2 and MP2/TIP5P results. The first possibility is that because EFP2 uses fragments with fixed internal geometries, the system is prevented from relaxing to a lower energy state in which the hydronium ion might lie closer to the surface of the cluster. Since the MP2/TIP5P results presented here use a solvent with frozen internal geometry, and since the MP2 hydronium ion does lie closer to the surface than does the EFP2 hydronium ion, it may be that only internal relaxation in the solute is needed. If this is indeed the case, and QM/MM MP2/EFP2 MD simulations should allow the system to relax sufficiently. *Ab initio*-EFP2 MD simulations are not currently possible, since the QM-EFP2 gradient is not yet fully implemented. Once this implementation is complete, QM-EFP2 MD simulations will be performed on solvated H_3O^+.

Since the EFP2 method generally predicts intermolecular interactions with an accuracy that is equivalent to that of MP2, a second possible reason that EFP2 MD simulations predict that H_3O^+ lies further from the surface than is predicted by most methods is that an MP2 MD simulation would predict such a result as well. That is, the EFP2 prediction could be the correct one. At present, performing MP2 AIMD simulations with no approximations is computationally infeasible for the system sizes and simulation times required. However, with fragmentation methods[38] such as the fragment molecular orbital (FMO) method,[39] or related methods[40,41,42] MP2 AIMD simulations will be possible.

4. Conclusions

The surface affinity of the hydronium ion was investigated using umbrella sampling based on MD simulations with both the EFP2 method and the combined MP2/TIP5P methods. The EFP2 and MP2/TIP5P probability density functions maintain common features independent of the number of solvating waters. According to the EFP2 method, the hydronium ion most probably lies ~halfway between the center and the edge of the cluster, while the MP2/TIP5P simulations predict that the H_3O^+ is most likely to be found ~0.5-2.0 Å from the edge of the cluster. Both of these predictions are independent of the cluster size. The origin of the different predictions by the two methods is as yet unresolved.

5. Acknowledgements

KRB was supported by a Department of Energy Computational Science Graduate Fellowship. MSG was supported by funds provided by the Department of Energy, Basic Energy Sciences, to the Ames Laboratory, administered by Iowa State University. SRP was supported by an SI2 grant from the National Science Foundation. The computations reported here were performed on the Iowa State University Cyence cluster, obtained via a National Science Foundation MRI grant, at Iowa State University.

References

1. Dang, L. X. (2003). Solvation of the hydronium ion at the water liquid/vapor interface. *The Journal of chemical physics*, *119*(12), 6351-6353.

2. Petersen, M. K., Iyengar, S. S., Day, T. J., & Voth, G. A. (2004). The hydrated proton at the water liquid/vapor interface. *The Journal of Physical Chemistry B*,*108*(39), 14804-14806.

3. Mucha, M., Frigato, T., Levering, L. M., Allen, H. C., Tobias, D. J., Dang, L. X., & Jungwirth, P. (2005). Unified molecular picture of the surfaces of aqueous acid, base, and salt solutions. *The Journal of Physical Chemistry B*, *109*(16), 7617-7623.

4. Petersen, P. B., & Saykally, R. J. (2005). Evidence for an enhanced hydronium concentration at the liquid water surface. *The Journal of Physical Chemistry B*,*109*(16), 7976-7980.

5. Tarbuck, T. L., Ota, S. T., & Richmond, G. L. (2006). Spectroscopic studies of solvated hydrogen and hydroxide ions at aqueous surfaces. *Journal of the American Chemical Society*, *128*(45), 14519-14527.

6. Buch, V., Milet, A., Vácha, R., Jungwirth, P., & Devlin, J. P. (2007). Water surface is acidic. *Proceedings of the National Academy of Sciences*, *104*(18), 7342-7347.

7. Levering, L. M., Sierra-Hernandez, M. R., & Allen, H. C. (2007). Observation of hydronium ions at the air-aqueous acid interface: vibrational spectroscopic studies of aqueous HCl, HBr, and HI. *The Journal of Physical Chemistry C*,*111*(25), 8814-8826.

8. Berkelbach, T. C., Lee, H. S., & Tuckerman, M. E. (2009). Concerted hydrogen-bond dynamics in the transport mechanism of the hydrated proton: A first-principles molecular dynamics study. *Physical review letters*, *103*(23), 238302.

9. Mundy, C. J., Kuo, I., Feng, W., Tuckerman, M. E., Lee, H. S., & Tobias, D. J. (2009). Hydroxide anion at the air–water interface. *Chemical Physics Letters*,*481*(1), 2-8.

10. Mizuse, K., Mikami, N., & Fujii, A. (2010). Infrared Spectra and Hydrogen-Bonded Network Structures of Large Protonated Water Clusters H+ (H2O) n (n= 20–200). *Angewandte Chemie International Edition*, *49*(52), 10119-10122.

11. Jagoda-Cwiklik, B., Cwiklik, L., & Jungwirth, P. (2011). Behavior of the Eigen form of hydronium at the air/water interface. *The Journal of Physical Chemistry A*, *115*(23), 5881-5886.

12. Knight, C., & Voth, G. A. (2011). The curious case of the hydrated proton.*Accounts of chemical research*, *45*(1), 101-109.

13. Takahashi, H., Maruyama, K., Karino, Y., Morita, A., Nakano, M., Jungwirth, P., & Matubayasi, N. (2011). Energetic origin of proton affinity to the air/water interface. *The Journal of Physical Chemistry B*, *115*(16), 4745-4751.

14. Yamaguchi, S., Kundu, A., Sen, P., & Tahara, T. (2012). Communication: Quantitative estimate of the water surface pH using heterodyne-detected electronic sum frequency generation. *The Journal of chemical physics*, *137*(15), 151101.

15. Wick, C. D. (2012). Hydronium Behavior at the Air–Water Interface with a Polarizable Multistate Empirical Valence Bond Model. *The Journal of Physical Chemistry C*, *116*(6), 4026-4038.

16. Kumar, R., Knight, C., & Voth, G. A. (2013). Exploring the behaviour of the hydrated excess proton at hydrophobic interfaces. *Faraday Discussions*, *167*, 263-278.

17. Car, R., & Parrinello, M. (1985). Unified approach for molecular dynamics and density-functional theory. *Physical review letters*, *55*(22), 2471.

18. Markovitch, O., Chen, H., Izvekov, S., Paesani, F., Voth, G. A., & Agmon, N. (2008). Special pair dance and partner selection: elementary steps in proton transport in liquid water. *The Journal of Physical Chemistry B*, *112*(31), 9456-9466.

19. Agmon, N. (1995). The grotthuss mechanism. *Chemical Physics Letters*,*244*(5), 456-462.

20. Schmitt, U. W., & Voth, G. A. (1998). Multistate empirical valence bond model for proton transport in water. *The Journal of Physical Chemistry B*, *102*(29), 5547-5551.

21. Wang, F., & Voth, G. A. (2005). A linear-scaling self-consistent generalization of the multistate empirical valence bond method for multiple excess protons in aqueous systems. *The Journal of chemical physics*, *122*(14), 144105.

22. Eigen, M. (1964). Proton Transfer, Acid-Base Catalysis, and Enzymatic Hydrolysis. Part I: ELEMENTARY PROCESSES. *Angewandte Chemie International Edition in English*, *3*(1), 1-19.

23. Zundel, G., & Metzger, H. (1968). Energiebänder der tunnelnden Überschuß-Protonen in flüssigen Säuren-eine IR-spektroskopische Untersuchung der Natur der Gruppierungen H5O2+. *Z. Phys. Chem*, *58*, 225-245.

24. Gordon, M. S., Freitag, M. A., Bandyopadhyay, P., Jensen, J. H., Kairys, V., & Stevens, W. J. (2001). The effective fragment potential method: A QM-based MM approach to modeling environmental effects in chemistry. *The Journal of Physical Chemistry A*, *105*(2), 293-307.

25. Gordon, M. S., Slipchenko, L., Li, H., & Jensen, J. H. (2007). The effective fragment potential: a general method for predicting intermolecular interactions.*Annual reports in computational chemistry*, *3*, 177-193.

26. Day, P. N., Pachter, R., Gordon, M. S., & Merrill, G. N. (2000). A study of water clusters using the effective fragment potential and Monte Carlo simulated annealing. *The Journal of Chemical Physics*, *112*(5), 2063-2073.

27. Merrill, G. N., & Gordon, M. S. (1998). Study of small water clusters using the effective fragment potential model. *The Journal of Physical Chemistry A*,*102*(16), 2650-2657.

28. Miller, Y., Thomas, J. L., Kemp, D. D., Finlayson-Pitts, B. J., Gordon, M. S., Tobias, D. J., & Gerber, R. B. (2009). Structure of Large Nitrate− Water Clusters at Ambient Temperatures: Simulations with Effective Fragment Potentials and Force Fields with Implications for Atmospheric Chemistry. *The Journal of Physical Chemistry A*, *113*(46), 12805-12814.

29. Kemp, D. D., & Gordon, M. S. (2005). Theoretical study of the solvation of fluorine and chlorine anions by water. *The Journal of Physical Chemistry A*,*109*(34), 7688-7699.

30. Flick, J. C., Kosenkov, D., Hohenstein, E. G., Sherrill, C. D., & Slipchenko, L. V. (2012). Accurate prediction of noncovalent interaction energies with the effective fragment potential method: Comparison of energy components to symmetry-adapted perturbation theory for the S22 test set. *Journal of Chemical Theory and Computation*, *8*(8), 2835-2843.

31. Choi, C. H., Re, S., Rashid, M. H., Li, H., Feig, M., & Sugita, Y. (2013). Solvent Electronic Polarization Effects on Na+–Na+ and Cl—Cl–Pair Associations in Aqueous Solution. *The Journal of Physical Chemistry B*,*117*(31), 9273-9279.

32. Uddin, N., Choi, T. H., & Choi, C. H. (2013). Direct Absolute p K a Predictions and Proton Transfer Mechanisms of Small Molecules in Aqueous Solution by QM/MM-MD. *The Journal of Physical Chemistry B*, *117*(20), 6269-6275.

33. Schmidt, M. W., Baldridge, K. K., Boatz, J. A., Elbert, S. T., Gordon, M. S., Jensen, J. H., ... & Montgomery, J. A. (1993). General atomic and molecular electronic structure system. *Journal of Computational Chemistry*, *14*(11), 1347-1363.

34 Mahoney, M. W., & Jorgensen, W. L. (2000). A five-site model for liquid water and the reproduction of the density anomaly by rigid, nonpolarizable potential functions. *The Journal of Chemical Physics*, *112*(20), 8910-8922.

35. Kumar, S., Rosenberg, J. M., Bouzida, D., Swendsen, R. H., & Kollman, P. A. (1992). The weighted histogram analysis method for free‐energy calculations on biomolecules. I. The method. *Journal of computational chemistry*, *13*(8), 1011-1021.

36. Grossfield, A., "WHAM: the weighted histogram analysis method", version 2.0.9, http://membrane.urmc.rochester.edu/content/wham

37. Li, J. L., Car, R., Tang, C., & Wingreen, N. S. (2007). Hydrophobic interaction and hydrogen-bond network for a methane pair in liquid water. *Proceedings of the National Academy of Sciences*, *104*(8), 2626-2630.

38. Gordon, M. S., Fedorov, D. G., Pruitt, S. R., & Slipchenko, L. V. (2012). Fragmentation methods: a route to accurate calculations on large systems.*Chem. Rev*, *112*(1), 632-672.

39. Komeiji, Y., Mochizuki, Y., Nakano, T., & Fedorov, D. G. (2009). Fragment molecular orbital-based molecular dynamics (FMO-MD), a quantum simulation tool for large molecular systems. *Journal of Molecular Structure: THEOCHEM*,*898*(1), 2-7.

40. Pruitt, S. R., Steinmann, C., Jensen, J. H., & Gordon, M. S. (2013). Fully Integrated Effective Fragment Molecular Orbital Method. *Journal of Chemical Theory and Computation*, *9*(5), 2235-2249.

41. Steinmann, C., Fedorov, D. G., & Jensen, J. H. (2010). Effective Fragment Molecular Orbital Method: A Merger of the Effective Fragment Potential and Fragment Molecular Orbital Methods†. *The Journal of Physical Chemistry A*,*114*(33), 8705-8712.

42. Lange, A. W., & Voth, G. A. (2013). Multi-state Approach to Chemical Reactivity in Fragment Based Quantum Chemistry Calculations. *Journal of Chemical Theory and Computation*, *9*(9), 4018-4025.

Figure 1a. Comparison of the EFP2 (blue) and MP2/TIP5P (red) hydronium ion probability distribution functions with the hydronium ion solvated by 32 waters

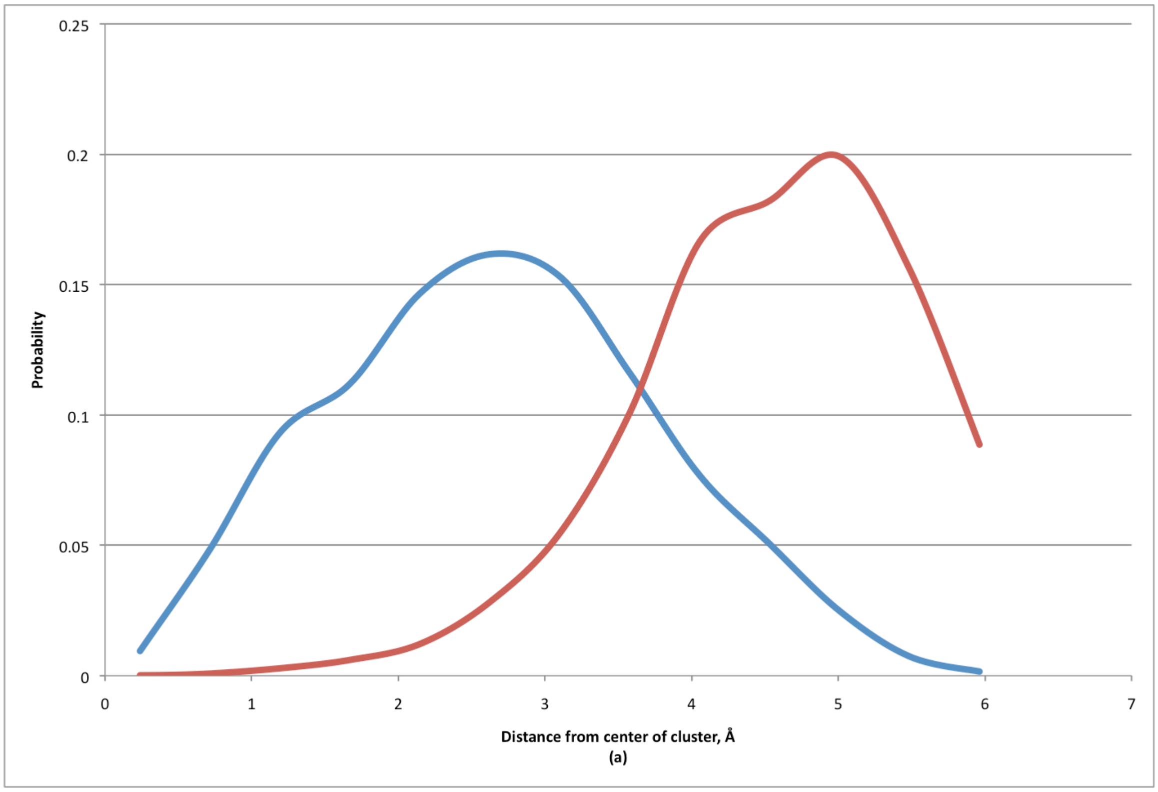

Figure 1b. Comparison of the EFP2 (blue) and MP2/TIP5P (red) hydronium ion probability distribution functions with the hydronium ion solvated by 64 waters

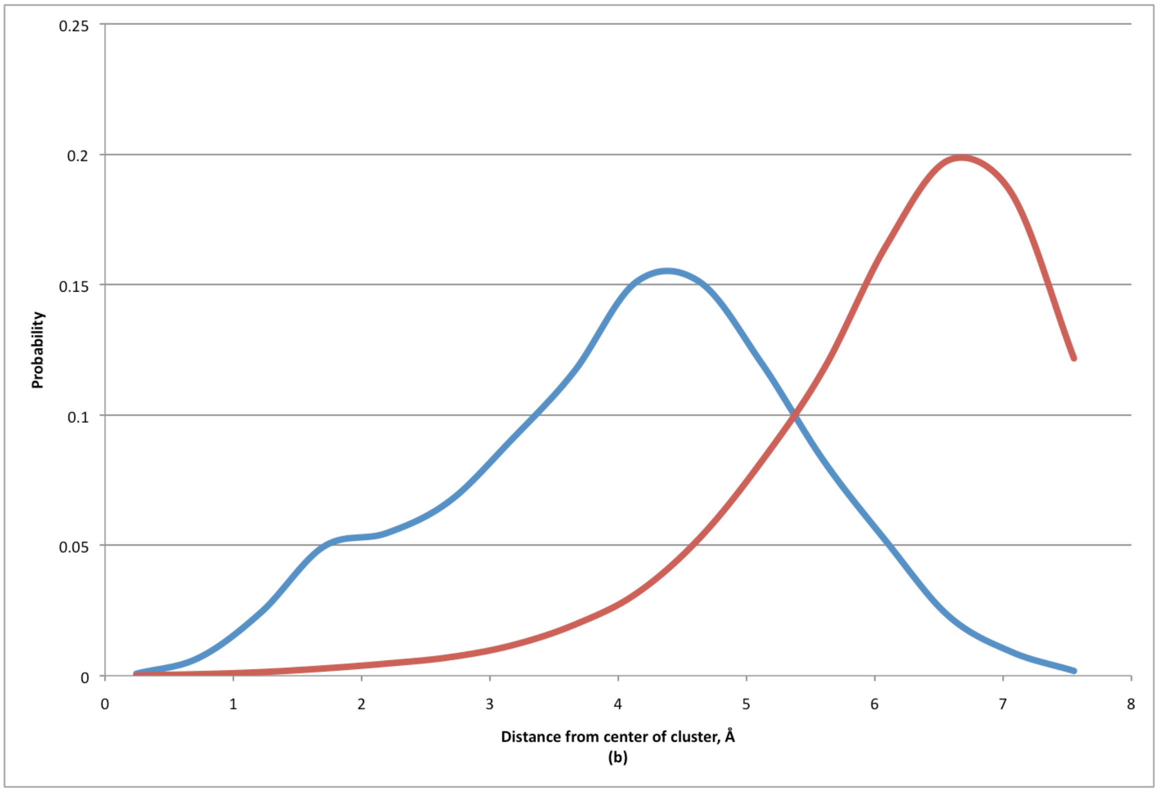

Figure 1c. Comparison of the EFP2 (blue) and MP2/TIP5P (red) hydronium ion probability distribution functions with the hydronium ion solvated by 128 waters

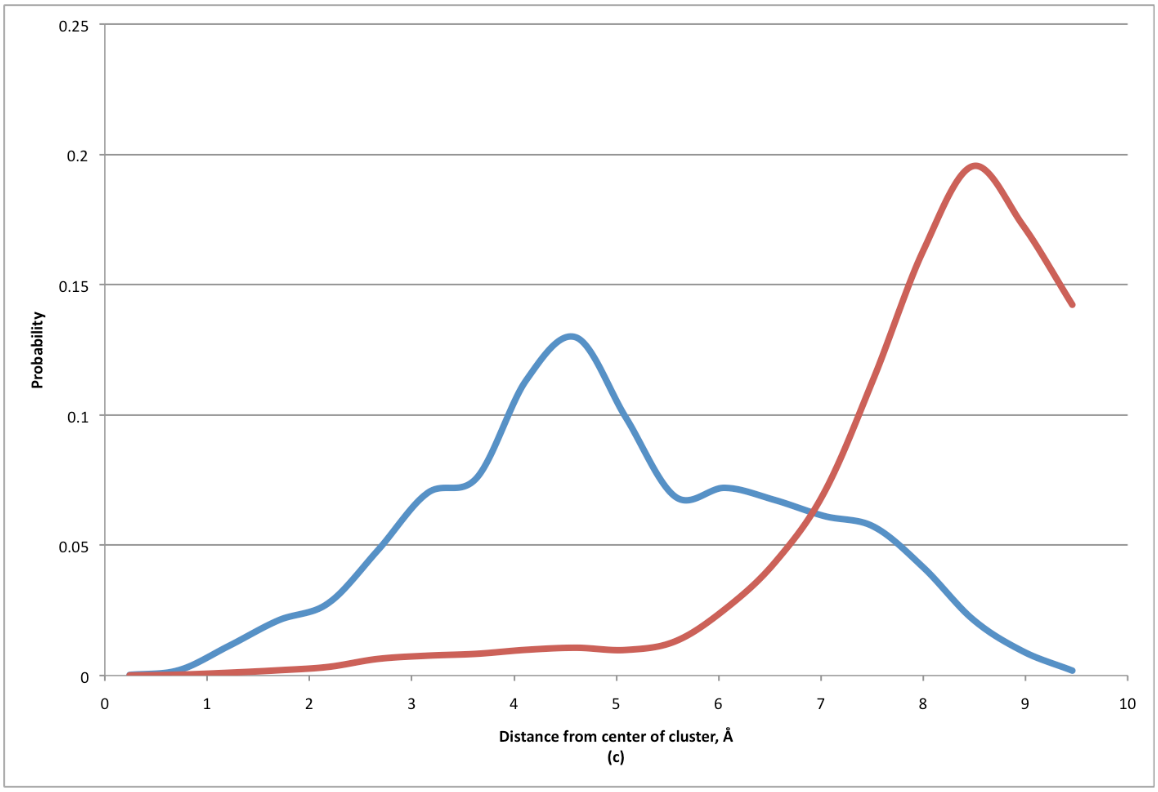

Figure 1d. Comparison of the EFP2 (blue) and MP2/TIP5P (red) hydronium ion probability distribution functions with the hydronium ion solvated by 256 waters

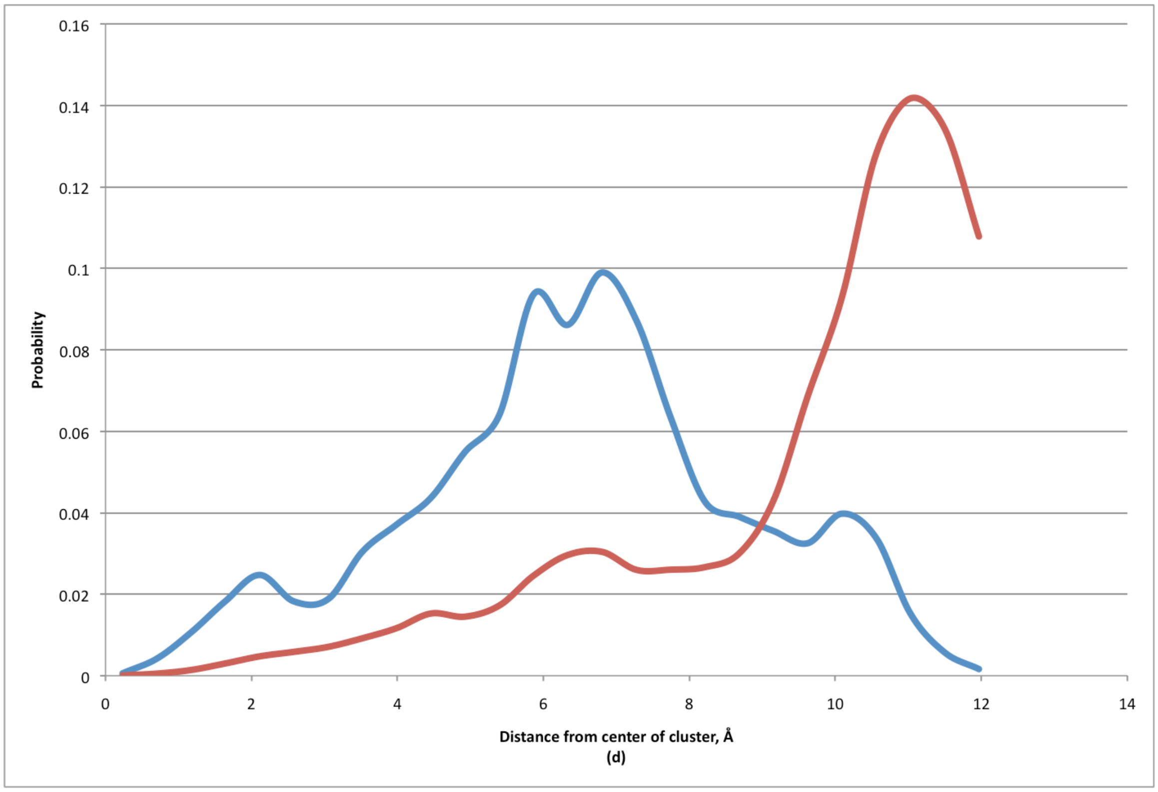

Chapter 6. Can the effective fragment potential method predict an accurate melting point for ice?

Kurt R. Brorsen, Mark S. Gordon

Abstract

The melting point of ice-I_h (T_m) is calculated by direct simulation of the solid-liquid interface with the waters described by the effective fragment potential. The NPH ensemble is used to calculate $T_{m,}$ with initial geometries and velocities from 300 K and 350 K NPT equilibrations. The NPH simulation with initial conditions from the 300 K NPT simulation converges to a T_m of 377.5 K ± 16.1 K. The NPH simulation with initial conditions from the 350 K NPT simulation converges to a T_m of 376.8 K ± 15.5 K.

1. Introduction

Chemistry at standard ambient temperature and pressure is ubiquitous. As the melting point of ice-I_h (T_m) is only 25 K lower than the standard ambient temperature, an accurate description of the phase diagram of water is an important characteristic of any water model. A small error in the description of the phase diagram of water can result in molecular dynamics (MD) calculations at the standard ambient temperature being performed in the wrong phase. Density functional theory (DFT) MD simulations have been employed to predict the melting point of ice. However, the DFT simulations result in errors in the predicted phase diagram of water. DFT with the PBE and BLYP functionals[1-3] predicts the melting point of ice-I_h to be 417 K and 411 K, respectively.[4] When dispersion corrections[5-7] are added to the BLYP functional, the predicted melting point improves to 360 K, still too high by nearly 90°.[8] Therefore, the DFT MD simulations on water at the standard ambient temperature can be interpreted as describing a supercooled state, rather than a true liquid state. The supercooled state results in an over-structured radial distribution function for water produced by DFT MD simulations at the standard ambient temperature.[9]

The melting point of ice-I_h has also been calculated using classical water models.[10-17] A simple point charge model, such as TIP3P, predicts a melting point of 146 K.[4] TIP4P/2005, improves on TIP3P, but still predicts a too low melting point of 251 K.[11] Due to the importance of predicting the phase diagram, the TIP4P model has also been reparameterized as TIP4P/ICE.[11] The TIP4P/ICE model has been designed to reproduce the melting point of ice-I_h by fitting the model potential parameters and predicts a melting point of 270 K.[11] The TIP5P method[118] predicts an accurate melting point of 272 K,[11] but predicts that ice-I_h is not thermodynamically stable at 1 bar.[19]

With recent improvements in force field method developments,[17,20-24] classical force fields can be generated from *ab initio* calculations as an alternative to fitting the parameters to empirical data. Examples of force fields generated by fitting parameters to *ab initio* calculations include iAMEOBA,[17] and TTM3-F.[20] The effective fragment potential (EFP) method is also obtained directly from *ab initio* quantum chemistry, but the EFP method contains no empirically fitted parameters.[21-24] The iAMEOBA and TTM3-F methods predict the melting point of ice-I_h to be 261 K and 248 K respectively.[17,8] The present study will focus on the EFP method.[21-24]

In the EFP method, a fragment with fixed internal geometry represents each water molecule. The EFP method contains five interaction energy terms that represent the fundamental types of intermolecular interactions:

$$E_{efp} = E_{Coul} + E_{pol} + E_{exrep} + E_{disp} + E_{CT} \qquad (1)$$

In Eq. (1), E_{Coul} is the EFP-EFP Coulombic interaction, expressed as a distributed multipole expansion. E_{pol} is the EFP-EFP polarization interacton, which is expressed in terms of localized orbital polarizability tensors and is iterated to self-consistency. The polarizability term accounts for many-body interactions via the iterative process. E_{exrep} represents the exchange repulsion interaction and is expressed in a power series in the intermolecular overlap. Because of the use of localized orbitals, the series is successfully truncated at the quadratic term. E_{disp} is the EFP-EFP dispersion interaction. E_{disp} is expressed in terms of localized orbital frequency-dependent polarizabilities, integrated over the imaginary frequency range. E_{CT} is the EFP-EFP charge transfer interaction, obtained in terms of the interaction between the occupied orbitals on one fragment and the virtual orbitals on the second fragment. Details regarding these terms can be obtained in the original references.

The EFP method accurately reproduces MP2 relative energies and geometries for water clusters, while requiring orders of magnitude less computational resources.[25]

The goal of the present study is to calculate the melting point of ice-I_h using the EFP method to determine if the EFP method can provide an accurate description of the melting point of ice-I_h at a reduced computational cost compared to previous DFT and model potential calculations.[4,8]

The melting point of ice-I_h can be calculated two ways: either by a Gibbs-Duhem integration of the free energy[26] or by direct simulation of the solid-liquid interface.[27-29] At the melting point, $G_{liq}(P,T)_{T=Tm} = G_{solid}(P,T)_{T=Tm}$, so finding the melting point of ice-I_h by

Gibbs-Duhem integration requires the non-trivial determination of the Gibbs free energy for the ice and liquid states. An alternative approach that will be used in the present study is to calculate the melting point by direct coexistence simulations of the ice-water interface. The direct coexistence simulations can be performed using different ensembles.[24] The present study uses the NPH ensemble, since the NPH ensemble allows the temperature of the system to adjust spontaneously to the melting point where $G_{liq}(P,T)_{T=Tm}= G_{solid}(P,T)_{T=Tm}$. Unlike the NVE ensemble, which also allows the temperature to spontaneously adjust, the NPH ensemble also allows standard pressure to be maintained during the simulation. For a simulation of ice-water in the NPH ensemble, if the initial temperature of the system is lower than the melting point, $T < T_m$, then the chemical potential of the liquid phase will be higher than the ice and waters from the liquid phase will release heat by freezing onto the ice surface. Likewise, if the initial temperature of the system is higher than the melting point, $T > T_m$, then the chemical potential of the ice will be higher than the liquid phase and waters from the ice will absorb heat and melt from the ice surface. Additional information about the relative benefits and drawbacks of Gibbs-Duhem integration and direct coexistence simulation in different ensembles can be found in a recent review.[30]

2. Computational Methods

The EFP method was used to describe the waters in all MD simulations, using the electronic structure program GAMESS.[31] To calculate T_m, an ice-liquid system of 192 waters was prepared in a simulation cell of 27.32x15.61x14.72 Å. A representative geometry of the ice-liquid system is presented in Figure 1. For the initial configuration of the ice-liquid system, 96 of the waters were assumed to be ice-I_h-like (top half of Figure 1) and were prepared with the Bernal-Fowler rules such that the simulation cell has a net zero dipole moment.[32] The remaining 96 waters (bottom half of Figure 1) were assumed to be liquid-like and were prepared from a NVT equilibration at 300 K for 100 ps with a step size of 0.25 fs using the velocity-Verlet algorithm in a simulation cell of 13.52x15.61x14.72 Å. The ice-liquid system in the present study is the same size and prepared in a similar manner as that used in previous DFT calculations of T_m.[4,8] The ice-liquid system in the present study was chosen to allow direct comparison of T_m between the EFP method and the previous DFT calculations.

The predicted T_m is apparently not converged with respect to system size for a simulation cell of 192 waters. Studies with the TIP4P potential have shown that the calculated T_m increases with system size, rising from ~200 K with a simulation cell of 192 waters to 229 ±1 K with a simulation cell of 12,288 waters.[33] A previous DFT study,[1,2] upon which the present work is based, calculated[4,8] T_m with a simulation cell of 192 waters. The authors assumed that for TIP4P and DFT, the change of T_m as a function of simulation cell size is qualitatively similar and therefore that their calculated T_m is most likely a lower bound of the true T_m for their level of theory. The assumption that the calculated T_m is most likely a lower bound of the true T_m is made in the present work as well.

500 fs equilibrations with a 0.25 fs step size were performed in the NPT ensemble at 1.0 atm with the velocity-Verlet algorithm at 300 K and 350 K on the merged ice-liquid systems to allow the ice-liquid system to relax. The final conditions of each of the NPT simulations were used as the initial conditions for the NPH simulations in which T_m

was calculated. The NPH simulations used a 0.25 fs step size, a pressure of 1.0 atm, and the velocity-Verlet algorithm. For the NPH simulations, the temperature was assumed to converge to T_m after 15 ps and the next 19.4 ps were used to determine the value of T_m.

3. Results and Discussion

The temperature versus the MD simulation time for the two NPH simulations is presented in Figure 2. The NPH simulation with initial conditions from the 300 K NPT simulation converges to a T_m of 377.5 K ± 16.1 K. The NPH simulation with initial conditions from the 350 K NPT simulation converges to a T_m of 376.8 K ± 15.5 K. Pooling and averaging the two NPH simulations together, T_m for the EFP method is calculated to be 377.2 K.

The T_m predicted by EFP compared to other methods is presented in Table 1. Unlike many of the classical force field methods presented in Table 1, the EFP method calculates too large a value for T_m. One possible source of error in the calculation of T_m is that the EFP fragments are internally rigid. Flexible force fields such as TTM3-F[20] or iAMOEBA[17] calculate a more accurate value for T_m than the EFP2 method. The error from the fixed internal geometries can be eliminated with the effective fragment molecular orbital (EFMO) method,[34,35] in which the fragments are flexible. The derivation and implementation of the EFMO analytic energy gradient is in progress. Once this is accomplished, EFMO MD simulations will be possible, and the importance of internal fragment flexibility can be assessed.

The T_m predicted by the EFP method is similar to that predicted by various DFT methods.[4,8] The agreement between the EFP and DFT methods is not entirely surprising, since the EFP method is derived from first principles. It is possible that the EFP method is correctly mimicking what the MP2 melting point of water would be if one performed MP2 MD simulations with internally frozen geometries. Calculating the melting point with MP2 by direct simulation of the solid-liquid interface is not currently computationally feasible, but through the use of fragmentation methods[36] such as the fragment molecular orbital method,[37,38] the T_m of ice-I_h described with MP2 will be calculated in the future.

4. Acknowledgements

KRB was supported by a Department of Energy Computational Science Graduate Fellowship. MSG was supported by funds provided by the Department of Energy, Basic Energy Sciences, to the Ames Laboratory, administered by Iowa State University.

References

1. Becke, A. D. (1988). Density-functional exchange-energy approximation with correct asymptotic behavior. *Physical Review A*, *38*(6), 3098.

2. Lee, C., Yang, W., & Parr, R. G. (1988). Development of the Colle-Salvetti correlation-energy formula into a functional of the electron density. *Physical Review B*, *37*(2), 785.

3. Perdew, J. P., Burke, K., & Ernzerhof, M. (1996). Generalized gradient approximation made simple. *Physical review letters*, *77*(18), 3865.

4. Yoo, S., Zeng, X. C., & Xantheas, S. S. (2009). On the phase diagram of water with density functional theory potentials: The melting temperature of ice ih with the Perdew–Burke–Ernzerhof and Becke–Lee–Yang–Parr functionals. *The Journal of chemical physics*, *130*(22), 221102.

5. Grimme, S. (2004). Accurate description of van der Waals complexes by density functional theory including empirical corrections. *Journal of computational chemistry*, *25*(12), 1463-1473.

6. Grimme, S. (2006). Semiempirical GGA-type density functional constructed with a long-range dispersion correction. *Journal of computational chemistry*,*27*(15), 1787-1799.

7. Grimme, S., Antony, J., Ehrlich, S., & Krieg, H. (2010). A consistent and accurate ab initio parametrization of density functional dispersion correction (DFT-D) for the 94 elements H-Pu. *The Journal of chemical physics*, *132*(15), 154104.

8. Yoo, S., & Xantheas, S. S. (2011). Communication: The effect of dispersion corrections on the melting temperature of liquid water. *The Journal of chemical physics*, *134*(12), 121105.

9. Grossman, J. C., Schwegler, E., Draeger, E. W., Gygi, F., & Galli, G. (2003). Towards an assessment of the accuracy of density functional theory for first principles simulations of water. *The Journal of chemical physics*, *120*(1), 300-311.

10. Vega, C., Sanz, E., & Abascal, J. L. F. (2005). The melting temperature of the most common models of water. *The Journal of chemical physics*, *122*(11), 114507.

11. Fernández, R. G., Abascal, J. L., & Vega, C. (2006). The melting point of ice Ih for common water models calculated from direct coexistence of the solid-liquid interface. *The Journal of chemical physics*, *124*(14), 144506.

12. Vega, C., Abascal, J. L., Conde, M. M., & Aragones, J. L. (2009). What ice can teach us about water interactions: a critical comparison of the performance of different water models. *Faraday discussions*, *141*, 251-276.

13. Paesani, F., Xantheas, S. S., & Voth, G. A. (2009). Infrared spectroscopy and hydrogen-bond dynamics of liquid water from centroid molecular dynamics with an Ab initio-based force field. *The Journal of Physical Chemistry B*, *113*(39), 13118-13130.

14. Vega, C., Abascal, J. L., Conde, M. M., & Aragones, J. L. (2009). What ice can teach us about water interactions: a critical comparison of the performance of different water models. *Faraday discussions*, *141*, 251-276.

15. Nilsson, A., & Pettersson, L. G. (2011). Perspective on the structure of liquid water. *Chemical Physics*, *389*(1), 1-34.

16. Vega, C., & Abascal, J. L. (2011). Simulating water with rigid non-polarizable models: a general perspective. *Physical Chemistry Chemical Physics*, *13*(44), 19663-19688.

17. Wang, L. P., Head-Gordon, T., Ponder, J. W., Ren, P., Chodera, J. D., Eastman, P. K., ... & Pande, V. S. (2013). Systematic improvement of a classical molecular model of water. *The Journal of Physical Chemistry B*,*117*(34), 9956-9972.

18. Mahoney, M. W., & Jorgensen, W. L. (2000). A five-site model for liquid water and the reproduction of the density anomaly by rigid, nonpolarizable potential functions. *The Journal of Chemical Physics*, *112*(20), 8910-8922.

19. Sanz, E., Vega, C., Abascal, J. L. F., & MacDowell, L. G. (2004). Tracing the phase diagram of the four-site water potential (TIP4P). *The Journal of chemical physics*, *121*(2), 1165-1166.

20. Fanourgakis, G. S., & Xantheas, S. S. (2008). Development of transferable interaction potentials for water. V. Extension of the flexible, polarizable, Thole-type model potential (TTM3-F, v. 3.0) to describe the vibrational spectra of water clusters and liquid water. *The Journal of chemical physics*, *128*(7), 074506.

21. Gordon, M. S., Freitag, M. A., Bandyopadhyay, P., Jensen, J. H., Kairys, V., & Stevens, W. J. (2001). The effective fragment potential method: A QM-based MM approach to modeling environmental effects in chemistry. *The Journal of Physical Chemistry A*, *105*(2), 293-307.

22. Gordon, M. S., Slipchenko, L., Li, H., & Jensen, J. H. (2007). The effective fragment potential: a general method for predicting intermolecular interactions.*Annual reports in computational chemistry*, *3*, 177-193.

23. M.S. Gordon, J.M. Mullin, S.R. Pruitt, L.B. Roskop, L.V. Slipchenko and J.A. Boatz, "Accurate Methods for Large Molecular Systems", J. Phys. Chem. B (Invited Centennial Feature Article), 113, 9646 (2009);

24. M.S. Gordon, D.G. Fedorov, S.R Pruitt, and L.V. Slipchenko, "Fragmentation Methods: A Route to Accurate Calculations on Large Systems", Chem. Rev, 112, 632 (2012)

25. Flick, J. C., Kosenkov, D., Hohenstein, E. G., Sherrill, C. D., & Slipchenko, L. V. (2012). Accurate prediction of noncovalent interaction energies with the effective fragment potential method: Comparison of energy components to symmetry-adapted perturbation theory for the S22 test set. *Journal of Chemical Theory and Computation*, *8*(8), 2835-2843.

26. Kofke, D. A. (1993). Gibbs-Duhem integration: a new method for direct evaluation of phase coexistence by molecular simulation. *Molecular Physics*,*78*(6), 1331-1336.

27. Ladd, A. J. C., & Woodcock, L. V. (1977). Triple-point coexistence properties of the Lennard-Jones system. *Chemical Physics Letters*, *51*(1), 155-159.

28. Ladd, A. J. C., & Woodcock, L. V. (1978). Interfacial and co-existence properties of the Lennard-Jones system at the triple point. *Molecular Physics*,*36*(2), 611-619.

29. Yoo, S., Zeng, X. C., & Morris, J. R. (2004). The melting lines of model silicon calculated from coexisting solid–liquid phases. *The Journal of chemical physics*, *120*(3), 1654-1656.

30. Vega, C., Sanz, E., Abascal, J. L. F., & Noya, E. G. (2008). Determination of phase diagrams via computer simulation: methodology and applications to water, electrolytes and proteins. *Journal of Physics: Condensed Matter*, *20*(15), 153101.

31. Schmidt, M. W., Baldridge, K. K., Boatz, J. A., Elbert, S. T., Gordon, M. S., Jensen, J. H., ... & Montgomery, J. A. (1993). General atomic and molecular electronic structure system. *Journal of Computational Chemistry*, *14*(11), 1347-1363.

32. Hayward, J. A., & Reimers, J. R. (1997). Unit cells for the simulation of hexagonal ice. *The Journal of chemical physics*, *106*(4), 1518-1529.

33. Wang, J., Yoo, S., Bai, J., Morris, J. R., & Zeng, X. C. (2005). Melting temperature of ice Ih calculated from coexisting solid-liquid phases. *Journal of Chemical Physics*, *123*(3), 36101-39900.

34. Pruitt, S. R., Steinmann, C., Jensen, J. H., & Gordon, M. S. (2013). Fully Integrated Effective Fragment Molecular Orbital Method. *Journal of Chemical Theory and Computation*, *9*(5), 2235-2249.

35. Steinmann, C., Fedorov, D. G., & Jensen, J. H. (2010). Effective Fragment Molecular Orbital Method: A Merger of the Effective Fragment Potential and Fragment Molecular Orbital Methods†. *The Journal of Physical Chemistry A*,*114*(33), 8705-8712.

36. Gordon, M. S., Fedorov, D. G., Pruitt, S. R., & Slipchenko, L. V. (2012). Fragmentation methods: a route to accurate calculations on large systems.*Chem. Rev*, *112*(1), 632-672.

37. Kitaura, K., Ikeo, E., Asada, T., Nakano, T., & Uebayasi, M. (1999). Fragment molecular orbital method: an approximate computational method for large molecules. *Chemical Physics Letters*, *313*(3), 701-706.

38. Komeiji, Y., Mochizuki, Y., Nakano, T., & Fedorov, D. G. (2009). Fragment molecular orbital-based molecular dynamics (FMO-MD), a quantum simulation tool for large molecular systems. *Journal of Molecular Structure: THEOCHEM*,*898*(1), 2-7.

Figure 1

Representative geometry of the ice-water system with 96 ice-I_h-like waters and 96 liquid-like waters.

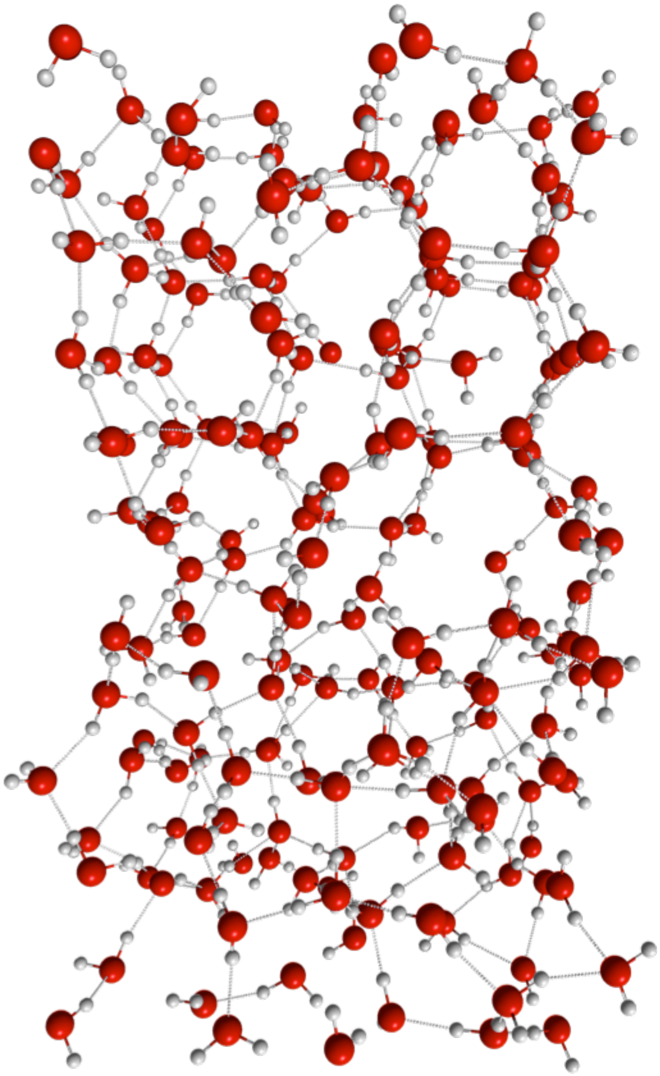

Figure 2

The temperature of the liquid-ice NPH simulations with initial conditions from the 300 K NPT simulation (blue) and 350 K NPT simulation (red).

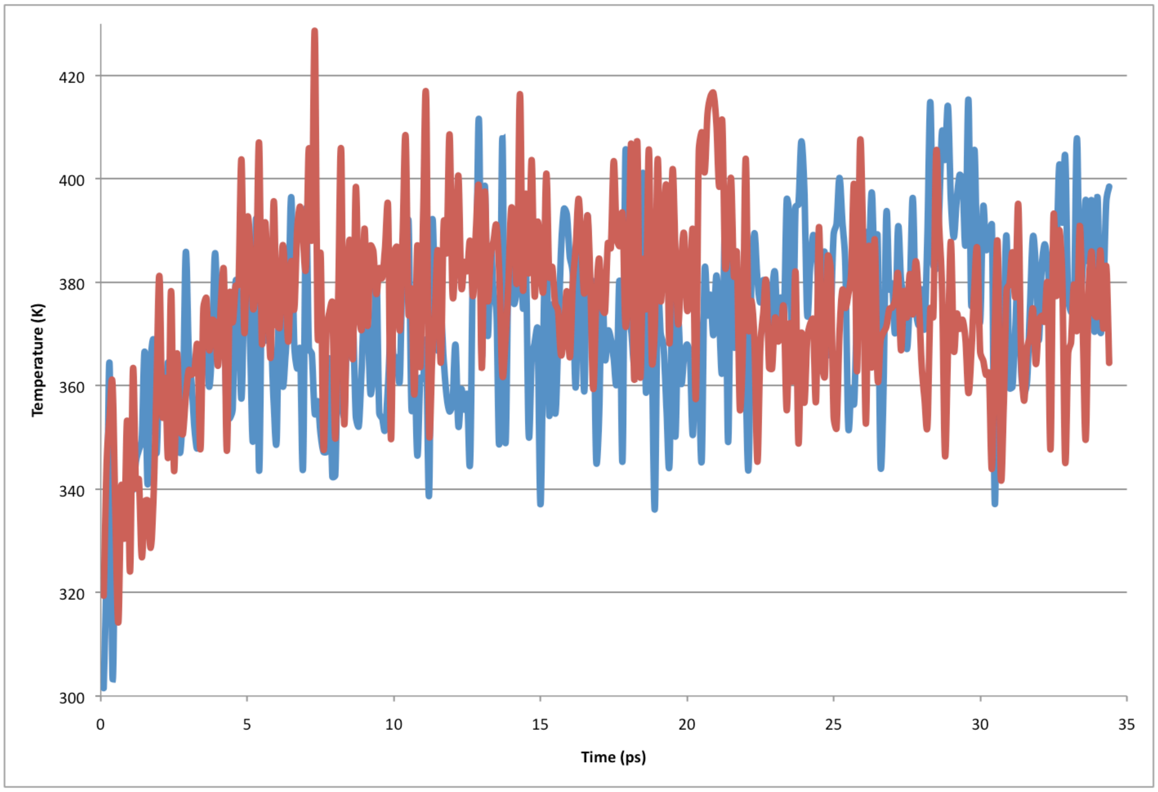

Table 1

Calculated melting point of ice-I_h

Method	Melting Point (K)
EFP2	377.2
BLYP[4]	417
PBE[4]	411
BLYP-D[8]	360
TIP3P[10]	146
TIP5P[11]	272
TTM3-F[8]	248
iAMOEBA[17]	261
TIP4P/ICE[11]	270
TIP4P/2005[11]	251

Chapter 7. Conclusions

In Chapter 2, the analytic gradient for the fragment molecular orbital (FMO) method expanded to second order (FMO2) and interfaced with restricted Hartree-Fock (RHF) was derived and the implemented was discussed. The FMO2-RHF analytic gradient requires the addition of response terms that arise from the derivative of the molecular orbital coefficient with respect to nuclear coordinate. The response terms are solved through the self-consistent Z-vector (SCZV) method. The SCZV procedure calculates the Z-vector of each fragment in the field of the Z-vectors of the other fragments. The derivation in chapter 2 is valid with the electrostatic dimer approximation, but requires that the FMO electrostatic potential either not be approximated at all, or be approximated uniformly.

The accuracy of the FMO2-RHF analytic gradient was tested by comparing the FMO-RHF analytic gradient and an earlier (incomplete) version of the FMO-RHF gradient with fully numerical gradients. For the four systems tested, the root mean square deviation (RMSD) of the FMO2-RHF analytic gradient was an order of magnitude less than the previous FMO2-RHF version of the gradient. The SCZV procedure parallelizes well, with a parallel efficiency of 98% on 32 nodes. The SCZV procedure increases the computational expense of an FMO2 calculation by 15-20%, a non-negligible but computationally tractable amount when considering the increase in the accuracy of the gradient.

In Chapter 3, the analytic gradient for the FMO2 method interfaced with density functional theory (DFT) was derived and the implementation discussed. Like the FMO2-

RHF analytic gradient, the FMO2-DFT gradient requires the addition of response terms arising from the derivative of the molecular orbital coefficient with respect to the nuclear coordinates; the FMO2-DFT analytic gradient includes the response terms through the SCZV method. The FMO2-DFT analytic gradient differs from the FMO2-RHF analytic gradient in that derivatives of the exchange-correlation functional must be included when calculating the response terms. Derivatives of the exchange-correlation functional are included in standard DFT gradient implementations, but FMO2-DFT requires higher order derivatives than is typical. The higher order derivatives arise during time-dependent DFT (TDDFT) calculations and so the FMO2-DFT analytic gradient contains components of DFT and TDDFT theory.

Similar to the FMO2-RHF gradient, the FMO2-DFT gradient was tested by comparing the FMO2-DFT gradient with and without the response terms included to numerical gradients. For all test systems, the FMO2-DFT gradient with response terms is more accurate than the FMO2-DFT gradient without response terms. The increase in the accuracy of the gradient through inclusion of response terms for FMO2-DFT is of similar magnitude as that of FMO2-RHF. The FMO2-DFT analytic gradient reproduces DFT gradient calculations in which no fragmentation was performed.

In Chapter 4, FMO2-RHF molecular dynamics (MD) simulations are performed with and without the analytic energy gradient to demonstrate that the analytic energy gradient is required for energy conservation in the NVE ensemble. The MD simulations are performed with different step sizes and the relative root mean square deviation of the energy from each MD simulations is used to check for energy conservation. The analytic gradient in MD simulations provides substantially better energy conservation than for

MD simulations without the analytic gradient, and for FMO2-MD simulations, an analytic gradient with response terms should always be used.

All analytic gradients for FMO are currently implemented only for FMO2. For FMO expanded to third order (FMO3), the present gradient is not fully analytic as the gradient neglects the response terms. FMO3 is typically perfromed when three-body effects are important in a system. In addition to better energies, for the NVE ensemble, FMO3-MD with a gradient that neglects response terms provides better energy conservation than FMO2-MD with a gradient that neglects response terms. While FMO3-MD provides better energy conservation than FMO2-MD, FMO3-MD is much more computationally expensive and FMO3-MD is best used only when three-body effects are important for the chemical system. FMO2-MD with the analytic gradient was therefore compared to FMO3-MD with a gradient neglecting response terms to see which provided better energy conservations. Owing to capabilities of different programs, a direct comparison could not be made, but by using an indirect comparison FMO2-MD with the analytic gradient was determined to provide better energy conservation in the NVE ensemble than FMO3-MD with a gradient neglecting response terms. Because of the better energy conservation of FMO2-MD with the analytic gradient, FMO3 is useful for FMO-MD solely when three-body effects are important.

In Chapter 5, the surface affinity of the hydronium ion was calculated using umbrella sampling where the system was described with the effective fragment potential (EFP). For comparison, QM/MM umbrella sampling calculations were performed in which the solute hydronium ion was treated with MP2 with the aug-cc-pVDZ basis and the solvent waters with both EFP and the TIP5P potential (MP2/TIP5P). To investigate the effect of cluster size on the surface affinity of the hydronium ion, umbrella sampling calculations were performed with 32, 64, 128, and 256 solvating waters.

For all cluster sizes, EFP predicts the hydronium ion to lie more interior than MP2/TIP5P. The cluster size was found to have negligible effect on the surface affinity of the hydronium ion, with EFP predicting that the solvated proton most probably lies halfway between the center and edge of the water cluster and MP2/TIP5P predicting the hydronium ion most probably lies 0.5-2.0 Å from the edge of the cluster independent of cluster size. The EFP results predict the hydronium ion to lie closer to the center of the water cluster than most of the recent experimental and computational literature. The discrepancy is hypothesized to arise from one of two possibilities. The first possibility is that the fixed internal geometries of the fragments in the EFP method are constraining the hydronium ion to lie in a higher energy region of space. From the results of other QM/MM studies of the hydronium ion, only the solute hydronium ion likely needs to be allowed to relax. In the future, QM/MM umbrella sampling calculations using MP2 to describe the hydronium ion and the EFP method to describe the solvent waters will be used to investigate the importance of solute relaxation. The other possibility is that since EFP method reproduces relative energies and geometries of water clusters at an MP2 level of theory, the EFP results are correctly mimicking MP2 MD. MP2 MD is computationally infeasible for the system sizes and time scales needed for the study, so a direct comparison is impossible, but by employing fragmentation and using FMO-MP2-MD or the effective fragment molecular orbital method (EFMO), an approximate comparison will be made.

In Chapter 6, the melting point of Ice-I_h was calculated using the EFP2 method by direct simulation of the water-ice interface. The melting point of Ice-I_h was calculated using the NPH ensemble with initial conditions from 300 and 350 K NPT equilibrations. The NPH simulation with initial conditions from the 300 K NPT simulation converges to a T_m of 377.5 K +/- 16.1 K. The NPH simulation with initial conditions from the 350 K NPT simulation converges to a T_m of 376.8 K +/- 15.5 K. The simulation cell contained 192 waters, so the melting point is not converged with respect to system size and therefore the calculated melting point is assumed to be a lower bound on the true melting point. The EFP2 method predicts a too high melting point similar to DFT methods. Since the EFP2 method agrees well with MP2 for the relative energies and geometries of water clusters, a hypothesis is presented that *ab initio* methods systematically overestimate the melting point of Ice-I_h. Similar to the investigation of the surface affinity of the hydronium ion, directly studying the hypothesis through MP2 MD is computationally intractable, but through the use of FMO-MD or EFMO an approximate comparison will once again be made.